Titre: Title:	Printable and Stretchable Polymers and Liquid Metal Composites for Wearable Electronics
Auteur: Author:	Chihyeong Kim
Date:	2026
Type:	Mémoire ou thèse / Dissertation or Thesis
Référence: Citation:	Kim, C. (2026). Printable and Stretchable Polymers and Liquid Metal Composites for Wearable Electronics [Thèse de doctorat, Polytechnique Montréal]. PolyPublie. https://publications.polymtl.ca/76283/

POLYTECHNIQUE MONTRÉAL

affiliée à l'Université de Montréal

Printable and Stretchable Polymers and Liquid Metal Composites for Wearable Electronics

CHIHYEONG KIM

Département de génie chimique

Thèse présentée en vue de l'obtention du diplôme de *Philosophiæ Doctor*

Génie chimique

Mars 2026

POLYTECHNIQUE MONTRÉAL

affiliée à l'Université de Montréal

Cette thèse intitulée :

Printable and Stretchable Polymers and Liquid Metal Composites for Wearable Electronics

présentée par **Chihyeong KIM**

en vue de l'obtention du diplôme de *Philosophiæ Doctor*

a été dûment acceptée par le jury d'examen constitué de :

Geraldine MERLE, présidente
Fabio CICOIRA, membre et directeur de recherche
Raphael TROUILLON, membre
Michele AMATO, membre externe

ACKNOWLEDGEMENTS

I would like to express my sincere gratitude to my supervisor, Professor Fabio Cicoira, for his invaluable guidance, mentorship, and support throughout this research project. His extensive knowledge and expertise in the field have strongly shaped the direction and development of this work. I am truly grateful for the opportunity to conduct my doctoral research under his supervision and for the trust and independence he granted me throughout this journey.

I would also like to thank the faculty members, as well as the technical and administrative staff of the Department of Chemical Engineering at Polytechnique Montréal, for providing an excellent research environment and continuous support during my studies.

I extend my heartfelt appreciation to my colleagues and collaborators, who have been a constant source of encouragement, inspiration, and friendship throughout my academic journey. This thesis represents not only my individual efforts but also the collective support and motivation I received from those around me.

Finally, I would like to express my deepest gratitude to my family for their unwavering support and encouragement. Their love, patience, and understanding have been the foundation that made this achievement possible.

RÉSUMÉ

L'impression a suscité un intérêt considérable en tant que technique de fabrication clé en raison de sa simplicité de mise en œuvre, de son faible coût et de sa grande capacité de personnalisation. Dans ce contexte, les matériaux pouvant être mis en solution, tels que les polymères, constituent des candidats idéaux pour l'électronique imprimable, car ils forment facilement des solutions ou des suspensions avec des solvants. Cette thèse de doctorat porte sur la fabrication de dispositifs portables utilisant des matériaux conducteurs souples rendus possibles grâce aux techniques d'impression.

Dans un premier temps, des transistors électrochimiques organiques entièrement imprimables ont été fabriqués en utilisant un hydrogel de poly(alcool vinylique) (PVA) comme électrolyte et le polymère conducteur poly(3,4-éthylènedioxythiophène):polystyrène sulfonate (PEDOT:PSS) comme matériau de canal. Des électrodes d'argent extensibles ont été utilisées pour les contacts drain/source, la grille et les interconnexions afin d'apporter une grande souplesse mécanique. La transconductance maximale et le rapport ON/OFF ont atteint respectivement 1,04 ± 0,13 mS et 830. En raison de la structure du réseau hydrogel et des différences de composition en solvants, les dispositifs présentant différentes formulations de gel ont montré des réponses transitoires et des stabilités opérationnelles à long terme distinctes. Le dispositif est resté stable pendant 50 jours et a supporté une déformation en traction allant jusqu'à 110 %, ce qui le rend adapté aux contraintes mécaniques attendues dans l'électronique portable. De plus, comme tous les composants imprimés étaient mécaniquement déformables, les transistors obtenus étaient entièrement extensibles, démontrant leur pertinence pour les applications électroniques portables.

Dans la deuxième étude, un composite multifonctionnel imprimable à base de métal liquide a été développé en tant qu'électrode ou interconnexion extensible pour dispositifs portables. La matrice polymère du composite a été rationnellement conçue et synthétisée afin d'assurer une bonne imprimabilité, une recyclabilité élevée et une compatibilité avec des environnements secs et immergés. Le composite a montré une extensibilité élevée, jusqu'à 500 % de déformation, ainsi qu'une conductivité électrique élevée (environ 10^5 S m^{-1}), tout en étant recyclable avec un rendement de récupération élevé (environ 95 %) grâce à l'utilisation de solvants verts. De plus, ce composite conducteur a démontré une excellente durabilité à l'état sec et humide, en maintenant une résistance stable sous des cycles de déformation allant de 0 à 50 % pendant plus de 16 h, à la

fois en environnement ambiant et aqueux, tout en fonctionnant efficacement comme capteur portable.

La dernière étude porte sur l'anisotropie électrique des films minces de PEDOT:PSS. L'anisotropie électrique constitue une stratégie prometteuse pour améliorer l'efficacité énergétique, un paramètre essentiel pour l'électronique portable. Des films de PEDOT:PSS présentant une anisotropie électrique dans le plan ont été obtenus en combinant un procédé classique de dépôt par spin-coating avec un post-traitement d'étirement humide à l'éthylène glycol. L'analyse des tendances de résistivité apparente a révélé un minimum distinct à environ 25 % de déformation, suggérant une réorganisation structurale induite par la contrainte. Les films de PEDOT:PSS traités dans ces conditions ont montré une anisotropie électrique dans le plan clairement définie, avec une résistance de feuille plus faible dans la direction d'étirement que dans la direction perpendiculaire. Cette approche offre une voie évolutive pour introduire une anisotropie électrique contrôlée dans les films minces de PEDOT:PSS, ouvrant des perspectives pour un large éventail d'applications électroniques et énergétiques.

Ce projet de doctorat a permis d'étudier de manière approfondie plusieurs composants de matériaux souples pour les dispositifs électroniques portables. En raison de la souplesse mécanique intrinsèque des polymères, tous les matériaux principaux étudiés dans cette thèse sont basés sur des polymères. Dans le premier projet, le fonctionnement des transistors électrochimiques organiques (OECT) a été étudié de manière systématique en fonction de la composition chimique des électrolytes hydrogels à base de PVA imprimés. Dans le deuxième projet, des composites multifonctionnels à base de métal liquide ont été développés grâce à la conception rationnelle et à la synthèse de matrices polymères adaptées à la formation de composites. Dans le dernier projet, un traitement d'étirement humide a été utilisé pour induire une anisotropie électrique dans des films minces de PEDOT:PSS par réorientation des chaînes polymères. Comme ce procédé d'étirement humide peut être appliqué aux films imprimés, les travaux futurs porteront sur l'extension de cette approche aux films imprimés de PEDOT:PSS et sur l'étude de leurs propriétés électromécaniques sous étirement.

ABSTRACT

Printing has attracted significant attention as a key manufacturing technique due to its facile processing, low cost, and high customizability. In this context, solution-processable materials such as polymers are ideal candidates for printable electronics, as they readily form solutions or suspensions with solvents. This PhD thesis focuses on the fabrication of wearable devices using soft conducting materials enabled by printing techniques.

First, fully printable organic electrochemical transistors were fabricated using a poly(vinyl alcohol) (PVA) hydrogel as the electrolyte and the conducting polymer poly(3,4-ethylenedioxythiophene):polystyrene sulfonate (PEDOT:PSS) as the channel material. Stretchable silver electrodes provided a soft feature to drain/source, gate and interconnect. The maximum transconductance and on/off ratio were 1.04 ± 0.13 mS and 830, respectively. Owing to hydrogel network structure and differences in solvent composition, devices with different gel formulations exhibited distinct transient responses and long-term operational stability. The device was stable for 50 days and stretched up to 110% tensile strain, which makes it suitable for withstanding the mechanical deformation expected in wearable electronics. Moreover, since all printed components were mechanically deformable, the resulting transistors were fully stretchable, demonstrating their suitability for wearable electronic applications.

In the second study, a printable multifunctional liquid-metal composite was developed as a stretchable electrode or interconnect for wearable devices. The polymer matrix of the composite was rationally designed and synthesized to ensure good printability, recyclability, and compatibility with both dry and underwater environments. The composite exhibited high stretchability up to 500% strain and high electrical conductivity (around 10^5 S m^{-1}), while also being recyclable with a high recovery yield (around 95%) using green solvents. In addition, the conducting composite showed excellent durability in both dry and wet states, maintaining its stable resistance with cyclic strain ranging from 0 to 50% for over 16 h, in both ambient and aqueous environments and functioned effectively as a wearable sensor.

The final study investigates the electrical anisotropy of PEDOT:PSS thin films. Electrical anisotropy is a promising strategy for improving device performance and energy efficiency, which is a critical consideration in wearable electronics. In-plane anisotropic PEDOT:PSS films were achieved by combining conventional spin coating with an ethylene glycol wet-stretch post-

treatment. Analysis of apparent resistivity trends revealed a distinct minimum at approximately 25% strain, suggesting a condition of strain-induced structural reorganization. PEDOT:PSS films treated under these conditions displayed clear in-plane electrical anisotropy, with lower sheet resistance along the strain direction compared to the perpendicular direction. This approach provides a scalable route to introduce controlled electrical anisotropy into PEDOT:PSS thin films, offering potential benefits for a wide range of electronic and energy applications.

This PhD work comprehensively investigated several soft material components for wearable electronic devices. Owing to the intrinsic mechanical softness of polymers, all major materials studied in this thesis were polymer-based. In the first work, the operational behavior of organic electrochemical transistors (OECTs) was systematically studied as a function of the chemical composition of printed poly(vinyl alcohol) (PVA)-based hydrogel electrolytes. In the second work, multifunctional liquid metal (LM) composites were developed through the rational design and synthesis of polymer matrices tailored for composite formation. In the final work, a wet-strain treatment was employed to induce electrical anisotropy in PEDOT:PSS thin films through polymer chain reorientation. Because this wet-strain process can be readily applied to printed films, future work will focus on extending this approach to printed PEDOT:PSS films and investigating their electromechanical characteristics under stretching.

TABLE OF CONTENTS

LIST OF TABLES

LIST OF FIGURES

LIST OF SYMBOLS AND ABBREVIATIONS

AIBN	Azobisisobutyronitrile
AR	Augmented reality
CAGR	Compound annual growth rate
DBSA	Dodecyl benzene sulfonic acid
DDMAT	2-(dodecylthiocarbonothioylthiododecylthiocarbonothioylthio)-2-methylpropionic acid
DIW	Direct ink writing
DMF	*N*,*N*-dimethylformamide
DMSO	Dimethyl sulfoxide
DSC	Differential scanning calorimetry
EDOT	3,4-ethylenedioxythiophene
EDX	Dispersive X-ray spectroscopy
EG	Ethylene glycol
EGain	Eutectic gallium–indium
EIS	Electrochemical impedance spectroscopy
EMI	Electromagnetic interference
FDM	Fused deposition modeling
Galinstan	Ga–In–Sn alloys
GOPS	(3-glycidyloxypropyl)trimethoxysilane
GPC	Gel permeation chromatography
IPA	Isopropanol
LMs	Gallium-based liquid metals
MR	Mixed reality

OECTs	Organic electrochemical transistors
PAA	Poly(acrylic acid)
PASTA	Poly(acrylic acid)-*b*-poly(styrene-*ran*-butyl acrylate)
PCB	Printed circuit board
PDI	Polydispersity index
PDMS	Polydimethylsiloxane
PEDOT	Polymerized 3,4-ethylenedioxythiophene
PEDOT:PSS	Poly(3,4-ethylenedioxythiophene) polystyrene sulfonate
PET	Polyethylene terephthalate
PSS	Polystyrene sulfonate
PVA	Polyvinyl alcohol
RAFT	Reversible addition–fragmentation chain transfer
RFID	Radio-frequency identification
SEM	Scanning electron microscope
SMU	Source-measure unit
THF	Tetrahydrofuran
TPU	Thermoplastic polyurethane
VR	Virtual reality
XR	Extended reality

LIST OF APPENDICES

CHAPTER 1 INTRODUCTION

1.1 Wearable devices

Wearable devices have gained significant attention in recent years, and consequently, their market size has increased steadily. The global wearable technology market size was estimated at USD 92.90 billion in 2025, with North America accounting for more than 33.0% of the total market revenue. The market size is projected to reach USD 229.97 billion by 2033, corresponding to a compound annual growth rate (CAGR) of 12.1% from 2026 to 2033. [1]

1.1.1 History of wearable devices

Wearable devices are generally defined as small electronic and mobile devices with wireless communication capability that are designed to be worn on the human body and integrated into gadgets, accessories, or clothing. Although wearable devices are currently associated with advanced electronic functionalities, early wearable devices were originally developed to enhance user experience rather than to provide electronic functions. From this perspective, wearable devices have existed since before the 20th century. One of the earliest wearable devices was the invention of glasses by Roger Bacon.[2] These glasses were designed to be easily carried and worn while improving vision. With the advancement of miniaturization technologies, pocket watches were further developed into wristwatches during the 19th century.[3] In addition, the Abacus Ring, invented in the 17th century, was designed as a compact accessory to assist traders with calculations and can be considered a predecessor of modern smart rings.

The development of wearable devices was strongly driven by military demands during World War I and World War II. Starting from the early 20th century, wearable devices began to incorporate electronic functionalities. Wristwatches became essential tools for planning and coordinating military operations, which contributed to the large-scale adoption of wearable devices in military applications.[4] This adoption later facilitated the widespread commercialization of wristwatches in the consumer market. During a similar period, the first wired hands-free communication devices integrated into flight helmets were developed for naval and aviation personnel.[5]

Following World War II, major technological innovations in wearable devices were achieved. In 1960, Morton Heilig patented the “Stereophonic Television Head-Mounted Display,” which contributed to the development of early virtual reality (VR) simulation systems.[6] Later, in 1968,

Ivan Sutherland developed the first VR head-mounted display system, enabling users to experience immersion in a three-dimensional virtual environment.[7] Subsequently, Steve Mann developed a backpack-based wearable computer capable of processing data from an eye-mounted camera and displaying the information in front of the user's eye.[8] This development is considered an early step toward modern augmented reality (AR) glasses.

Fitbit was founded by James Park and Eric Friedman.[9] In 2008, Fitbit launched the Fitbit Classic, which was one of the first wireless activity trackers capable of synchronizing data with the Internet and enabling access to the same data through mobile devices.[10] In 2009, Samsung released the S9110 smartwatch, which functioned as a dual-band general packet radio service phone with email exchange capability.[11] This smartwatch provided Bluetooth connectivity, a full-color touchscreen, an audio player, and voice recognition functionality. In 2012, Google announced its goal of developing a portable wearable computer through a public project announcement on its social network platform. Following this announcement, Google demonstrated Google Glass to the public, which significantly accelerated the development and adoption of AR and VR wearable technologies.[12]

1.1.2 Next-generation wearable devices

From approximately 2015 to the present, the market for virtual interface–based wearable devices, including AR, VR, extended reality (XR), and mixed reality (MR) glasses and headsets, has expanded rapidly. This growth has been strongly driven by advancements in display technology, computing power, and wireless communication, as well as increasing consumer demand for immersive digital experiences. From an entertainment perspective, the outlook for the VR device market is expected to remain positive due to its applications in gaming, media, and virtual social interaction. In parallel, the importance of wearable technologies in healthcare has increased significantly. In particular, interest in health data tracking systems, including healthcare monitoring and remote diagnosis technologies, has increased following the COVID-19 pandemic, which highlighted the importance of remote patient monitoring and digital healthcare infrastructure.[13, 14] Furthermore, the global aging population has accelerated the expansion of wearable healthcare monitoring technologies, as continuous physiological monitoring is becoming increasingly important for chronic disease management and early medical intervention. [15]

In this context, soft wearable devices have emerged as promising platforms for monitoring physiological signals across various regions of the human body. Although conventional rigid wearable devices have demonstrated well-established electrical performance, they may have limitations when applied to highly curved or frequently moving body regions such as elbows, knees, and shoulders, particularly when stable signal monitoring is required during body motion.[16, 17] This limitation arises from the intrinsic mechanical mismatch between rigid materials—such as gold and silicon, which possess high Young's moduli (> 1 GPa)—and the soft, compliant nature of biological tissues.[18] In contrast, soft wearable devices based on polymers exhibit mechanical properties that are more comparable to those of biological systems (≈ kPa–MPa), enabling their application across diverse and localized regions of the body. For example, polymer-based devices capable of sustaining tensile strains of up to 60% can be applied to various body regions while accommodating mechanical deformations associated with skin stretching and joint movement. This mechanical compatibility enables conformal and cohesive contact between the device and the target tissue or organ, which helps reduce signal noise and minimize signal degradation. Moreover, soft wearable devices improve user comfort and long-term wearability while also reducing the risk of skin irritation and mechanical damage.[19] To achieve mechanical properties comparable to biological tissues, the development of soft metallic electrodes and soft sensing materials based on polymers is critically important in wearable device design. In addition, the solution-processability of polymer-based materials enables scalable fabrication approaches for soft electronic systems.

In addition to mechanical compatibility and processability, one of the major challenges in next-generation wearable electronics is achieving a balance between electrical performance and mechanical compliance. [20, 21] The current industry standard is defined by the high performance of silicon-based rigid electronic devices. Although organic semiconductors can impart mechanical softness to electronic systems, this advantage is often accompanied by a compromise in electrical performance. Therefore, significant efforts are required to approach the performance levels of rigid counterparts while maintaining mechanical deformability. Another challenge in next-generation wearable electronics is energy consumption.[22] Future wearable healthcare devices are expected to operate wirelessly while continuously monitoring physiological signals. Because wireless wearable devices cannot rely on constant external power supply, they must secure sufficient energy storage or generation capability to ensure reliable operation over the required duration. To address

this challenge, self-powered approaches such as energy harvesting technologies and photovoltaic energy conversion systems have been actively investigated.[23, 24] Although self-sustained energy generation systems represent promising solutions, improving overall device energy efficiency through the development of energy-efficient materials and optimized device architectures is also a viable and important strategy.

1.2 Printing technology

Printing technologies have been gaining significant attention and have continuously developed over the past decades. At present, these technologies are widely applied across a broad range of fields, from the fabrication of three-dimensional polymer structures to large-scale concrete printing for construction applications.[25] In addition, there have been numerous research efforts aimed at manufacturing electronic devices using additive manufacturing approaches, as printing technologies generally enable low-cost and facile production processes. Furthermore, low-cost printing processes are associated with reduced material waste, which contributes to environmentally friendly and sustainable manufacturing. According to market analyses reported by industry experts (Precedence Research), the printed electronics market reached approximately $10 billion in 2021 and is expected to grow to $44.4 billion by 2030, corresponding to a CAGR of 18.5% from 2021 to 2030.[26]

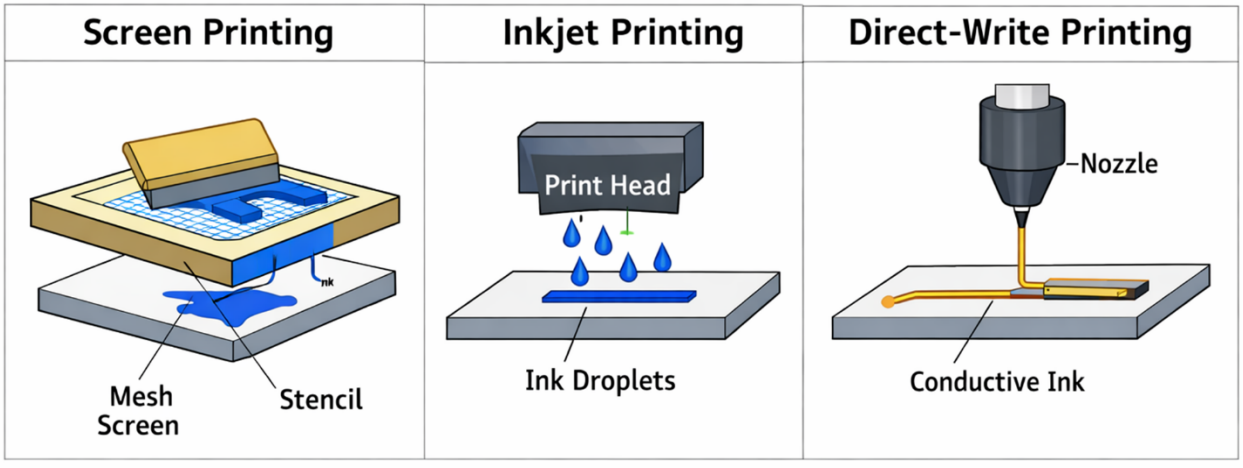

Figure 1.1 Scheme of screen printing, inkjet printing, and direct ink write printing

Several printing techniques have been employed to pattern electronic components, and some of these techniques have already been consolidated at the industrial level (Figure 1.1). Among these, screen printing originates from simple stencil-based printing methods. A typical screen-printing system consists of a patterned screen, a squeegee (rubber blade), and a printing bed or platform. During the printing process, the substrate is placed and secured on the printing bed. Ink is then deposited onto the screen, and as the squeegee moves across the screen surface, the ink is forced through the patterned openings of the stencil and transferred onto the substrate below. Screen printing is generally categorized as a contact-based printing method. Related processes include roll-to-roll printing and transfer printing, in which pre-patterned materials are transferred from a donor substrate onto a receiver substrate. Due to the use of pre-patterned screens, screen printing is highly suitable for repeatable and large-scale production and is relatively simple and cost-effective. However, inks used in screen printing typically require high viscosity to prevent excessive spreading and uncontrolled flow on the substrate surface.[27] In addition, contact-based printing methods can introduce challenges when printing on complex three-dimensional surfaces or when fabricating multilayered structures.[28]

Inkjet printing is a widely used non-contact printing technique based on drop-on-demand deposition. During printing, small droplets of ink are ejected from the printhead nozzle onto the substrate using piezoelectric actuation, without direct physical contact. This non-contact approach enables patterns to be digitally designed and executed using a computer-controlled system, allowing for facile customization of device geometries. In addition, non-contact printing minimizes contamination and mechanical damage to components while also reducing material waste.[29] However, inkjet printing requires strict optimization of ink properties, including viscosity (typically 10–12 cP), solvent volatility, and pH range (typically 4–9). If the ink formulation is not properly optimized, nozzle clogging can occur more frequently compared to other printing technologies.

Direct ink writing (DIW) is another non-contact printing technique that employs a computer-controlled syringe or nozzle to continuously dispense ink onto a substrate. Depending on ink properties, driving forces for ink ejection, and pattern design models, DIW can be further classified into several subcategories. For example, DIW combined with fused deposition modeling (FDM) and three-dimensional pattern design is commonly categorized as three-dimensional printing. DIW processes based on aerodynamic focusing are classified as aerosol jet printing.[30] In aerosol jet

printing, functional inks are first atomized into fine aerosol droplets using ultrasonic or pneumatic methods. The aerosol is then focused into a narrow stream by an inert sheath gas, enabling precise deposition onto the substrate. Compared to inkjet printing, this technique supports a much wider range of ink viscosities without severe nozzle clogging, providing greater versatility in material selection. As a result, DIW-based techniques can be used to print hydrogels, ceramics, polymers, composites, and other functional materials.[31] In addition, the use of digitally designed patterns enables facile customization of device geometries. Owing to these advantages, DIW using solvent-based inks and computer-controlled mechanical pressure dispensing was employed in my PhD works. Furthermore, printable (solution-processable) soft materials were systematically investigated as functional inks for the fabrication of wearable electronic devices.

1.3 Soft conducting materials

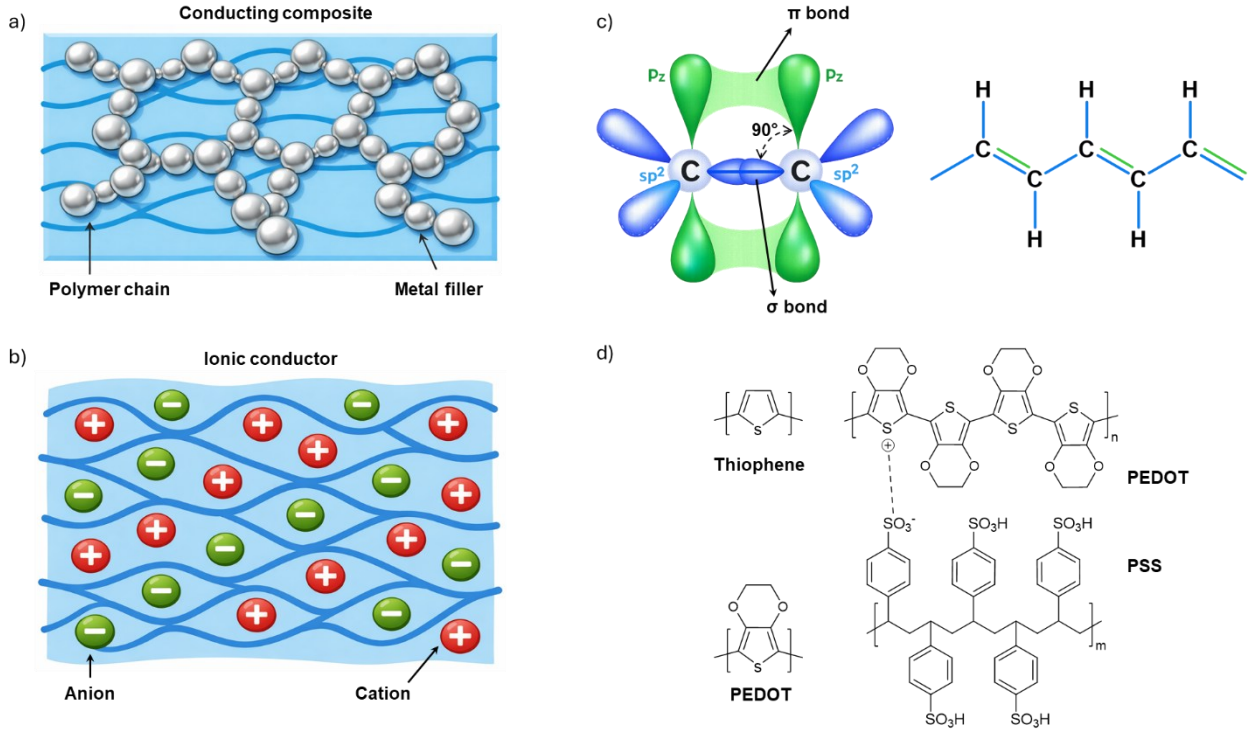

Figure 1.2 schemes of a) conducting composite and b) ionic conductor based on polymer matrix. c) scheme of formation of π bond between two carbon molecules and a segment of polyacetylene. d) chemical stuctures of polythiophene-based conjugated polymers.

A conventional approach to achieving stretchable electronic devices is the combination of rigid active components with stretchable conductors on a stretchable substrate.[32, 33] The soft conductors surrounding the rigid active devices act as interconnects, making a rigid island structure and tolerating mechanical deformation. Unlike rigid island-based electronics, fully stretchable electronics consist of all stretchable components, having relatively stable mechanical matching between active components and interconnects.[34, 35]

Stretchable conductors are essential building blocks for wearable electronic systems. To achieve conductor stretchability, two primary strategies have been explored. First, structural engineering enables conventionally deposited conductors to withdraw physical deformation, such as serpentine,[36] wrinkled,[37] mesh,[38] microcracked,[39] or buckled structures.[40] In contrast, intrinsically soft conductors offer an alternative strategy that can be more suitable for wearable applications. These materials inherently possess mechanical compliance, enabling improved conformability and more intimate contact with biological tissues. Furthermore, intrinsically soft conductors based on polymers are compatible with printing techniques, facilitating scalable and versatile patterning for soft electronic devices. Accordingly, three types of polymer-based soft conductors are introduced and classified below.

Conducting composites are multiphase materials consisting of an electrically insulating matrix combined with electrically conductive fillers, designed to achieve electrical conductivity while maintaining desirable mechanical, processing, and structural properties (Figure 1.2 a). In most cases, the matrix material is an insulating polymer, while the conductive phase can consist of metallic particles, carbon-based nanomaterials, or intrinsically conducting polymers. The overall electrical properties of conducting composites arise from the formation of conductive pathways, commonly referred to as a percolated network, within the insulating matrix. Once the filler concentration exceeds a critical percolation threshold, a continuous conductive pathway is formed, enabling efficient charge transport through the composite material.

Conducting composites offer several advantages compared to bulk conductive materials such as metals. First, they can provide mechanical flexibility and stretchability, which are essential for applications in soft electronics and wearable devices. Second, their electrical properties can be tuned by adjusting filler concentration, filler morphology, and composite structure. Third, conducting composites are often compatible with solution-based processing methods such as

printing, coating, and casting, which enables scalable and low-cost manufacturing. Due to these advantages, conducting composites are particularly attractive for wearable electronic applications, where both electrical conductivity and mechanical compliance are required.

Soft ionic conductors are materials that can transport ions while maintaining soft mechanical properties such as flexibility or stretchability. Unlike conventional rigid ionic conductors, which are typically ceramic or crystalline solid electrolytes, soft ionic conductors are usually based on polymer networks, gels, or elastomers that allow mechanical deformation, maintaining ionic transport functionality. In soft electrolytes, ionic transport occurs through the movement of mobile ionic components, such as dissolved salts or ionic liquids, within a soft matrix (Figure 1.2 b). The soft matrix provides mechanical integrity and enables conformal contact with soft or dynamic surfaces such as bio-tissues, while the mobile ionic species provide ionic conductivity.

Conjugated polymers have a conjugated structure along their polymer backbone, which enables electronic charge transport along the polymer chain and gives these polymers semiconducting or electrically conducting properties. In 1977, Hideki Shirakawa, Alan MacDiarmid, and Alan Heeger discovered that polyacetylene, when doped with iodine, exhibited metallic-level electrical conductivity.[41] This discovery established conjugated polymers as a new class of electrically functional organic materials and provided fundamental insights into the mechanisms of electrical conduction in organic polymers.[42]

Many organic polymers are composed of carbon backbone chains. A carbon atom ($1s^2\ 2s^2\ 2p^2$) contains six electrons in total, of which four are valence electrons. These valence electrons allow carbon atoms to form covalent bonds with surrounding atoms such as carbon and hydrogen. Two primary bonding configurations can be formed depending on the hybridization state of the carbon atom.

First, in sp^3 hybridization, one electron from the 2s orbital is promoted to the 2p orbital, and the s and p orbitals hybridize to form four equivalent sp^3 hybrid orbitals. These orbitals form tetrahedrally directed covalent bonds, which are commonly found in diamond and conventional polymer materials such as polyethylene and other commodity plastics. In polymers based on sp^3 hybridized carbon, all valence electrons are involved in localized σ covalent bonds. As a result, there are no free charge carriers available for electrical conduction, and these polymers behave as electrical insulators.

The second bonding configuration involves sp^2 hybridization combined with a remaining unhybridized p_z orbital. In this configuration, three sp^2 hybrid orbitals form σ covalent bonds arranged in a planar hexagonal geometry, which is commonly observed in conjugated polymers and graphite. Taking polyacetylene as an example, three σ bonds form the backbone of the polymer chain through covalent bonding between adjacent carbon atoms. The remaining p_z orbitals overlap along the polymer backbone, forming a continuous π-electron system (π-bond) (Figure 1.2 c).

The delocalization of π-electrons along this π-bond enables electronic charge transport along the polymer chain. When conjugated polymers are chemically doped, charge carriers such as polarons or bipolarons can be introduced into the π-electron system, significantly increasing electrical conductivity. Therefore, the presence of a delocalized π-electron system is the fundamental structural feature that enables electrical conductivity in conjugated polymers. Owing to the intrinsic electrical conductivity and inherent mechanical softness of conjugated polymers, they are promising materials for use as conductive electrodes and sensing materials in wearable electronic devices.

1.3.1 PEDOT:PSS

Following the discovery of conductive polyacetylene, extensive research efforts were initiated to develop this new class of electrically conductive plastics into practical materials. Although conductive polyacetylene demonstrated extremely high electrical conductivity after chemical doping, significant challenges remained. In particular, maintaining the doped conductive state under ambient air conditions and improving the processability of polyacetylene proved to be difficult.[43] Aromatic rings containing sulfur atoms, such as thiophene, exhibit strong electron-donating characteristics, which help stabilize the positively charged conducting state of doped conjugated polymers.[44] Based on this concept, polythiophene-based conjugated polymers were developed(Figure 1.2 d).

To stabilize the dope state of polythiophene further, ring-closure metathesis of oxygen-containing substituents was introduced to forma six-membered dioxane ring structure, synthesizing 3,4-ethylenedioxythiophene (EDOT) monomer.[45] Polymerized EDOT (PEDOT) exhibited significantly improved electrical conductivity and enhanced stability of the doped state. Due to these advantages, numerous research groups subsequently developed and patented various synthesis methods for PEDOT.

Despite these improvements, early PEDOT materials still exhibited poor processability, particularly in terms of solubility and dispersion. The development of solution-processable PEDOT became an important research objective. This challenge was successfully addressed by introducing poly(styrenesulfonate) (PSS) as a counter-ion dopant and stabilizing agent. In PEDOT:PSS, PEDOT chains are electrostatically bound to the hydrophilic PSS polyanion chains. This structure allows PEDOT:PSS to be dispersed in water, forming a colloidal "core–shell" structure in which conductive PEDOT-rich domains are surrounded by insulating PSS-rich shells. In addition, due to the hydrophilic and ionic nature of PSS, water molecules and external cations can penetrate into PEDOT:PSS films. As a result, the entire volume of PEDOT:PSS can become electrochemically active,[46] which is a key feature enabling its application in electrochemical devices.

1.4 Bioelectronics

Bioelectronics is an interdisciplinary field that integrates principles from electronics, materials science, biology, and medicine to develop electronic systems capable of interfacing with biological environments. The primary objective of bioelectronics is to enable the detection, monitoring, modulation, or stimulation of biological signals using electronic devices. These systems operate at the interface between living tissues and electronic materials, facilitating bidirectional communication between biological systems and electronic circuits. Owing to these characteristics, bioelectronic systems are frequently implemented in the form of wearable devices.

Biological systems primarily rely on ionic and electrochemical signaling, whereas conventional electronic devices rely on electronic charge transport. Therefore, from a materials engineering perspective, mixed ionic–electronic conductors are often employed at the interface between biological systems and electronic devices. Among these materials, PEDOT:PSS is one of the most widely used materials due to its low interfacial impedance, high volumetric capacitance, and good biocompatibility.

1.4.1 Organic electrochemical transistors (OECTs)

From a device engineering perspective, the development of electronic devices capable of effectively sensing biological signals is equally important. A representative example of such devices is the organic electrochemical transistors (OECTs). OECTs operate using an electrolyte as a gating medium to modulate the electrical signal of the device. Because biological systems

generate ion-based signals, OECTs are highly compatible with biological environments. Ionic signals from biological systems can directly interact with the electrolyte and modulate the conductivity of the conducting polymer channel.

In addition, OECTs possess intrinsic signal amplification capability due to their transistor architecture. This intrinsic amplification improves signal detection accuracy and reduces noise interference, enabling reliable detection of weak biological signals. As a result, OECTs are considered highly promising devices for bioelectronic sensing applications, particularly in wearable and implantable bioelectronic systems.

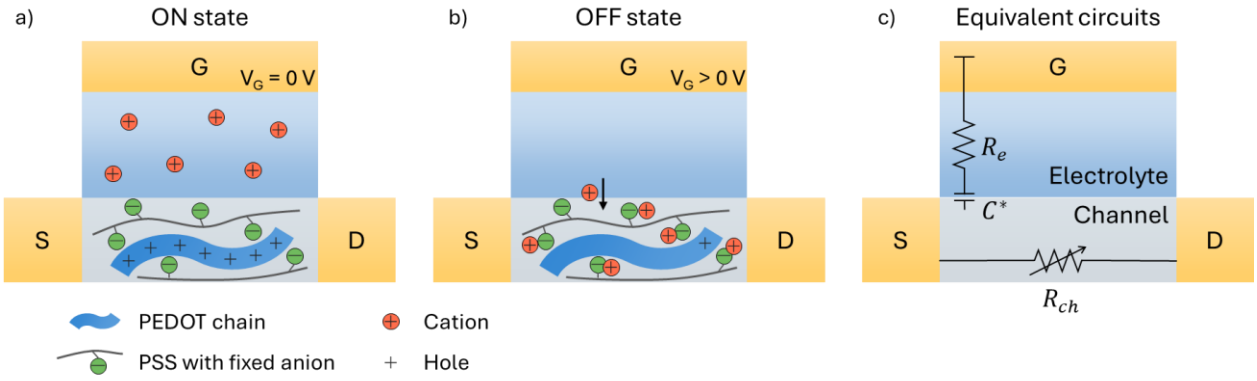

Figure 1.3 Schemes of PEDOT:PSS-based OECTs in a) ON state and b) OFF state with application of a positive gate potential ($V_G > 0$ V). c) scheme of equivalent circuits

Since PEDOT:PSS-based OECTs were the primary focus of this PhD work, the device operation mechanism and physics were investigated mainly using PEDOT:PSS as the semiconducting channel material. PEDOT:PSS behaves as a p-type semiconductor, meaning that the majority charge carriers are positively charged holes. These holes are electrostatically compensated by the sulfonate anions of PSS, which, from a solid-state physics perspective, can be considered as ionized acceptor species.[47]

OECTs based on PEDOT:PSS typically operate in depletion mode. In this mode, hole current flows through the channel even in the absence of an applied gate potential, resulting in the ON state of the device (Figure 1.3 a). When a positive gate bias is applied, cations from the electrolyte are injected into the PEDOT:PSS channel. These injected cations compensate the negatively charged sulfonate groups that originally stabilized the oxidized (doped) PEDOT chains. As a result, the

effective hole concentration in the channel decreases, leading to de-doping of PEDOT (Figure 1.3 b). Because the extracted holes at the drain are not replenished at the source under these conditions, the channel conductivity decreases. This process results in a reduction of the drain current, and the device transitions toward the OFF state.[48]

Due to the volumetric capacitance of PEDOT:PSS, ions can penetrate throughout the entire bulk of the channel material rather than being confined only to the surface interface. Consequently, modulation of the doping level occurs across the entire channel volume. This volumetric electrochemical interaction enables large modulation of channel current at relatively low gate voltages (typically below 1 V), resulting in intrinsic signal amplification and efficient ON–OFF switching behavior.[49]

In addition, compared with conventional field-effect transistors that rely on a dielectric layer, the use of an electrolyte and a volumetrically capacitive channel provides greater flexibility in device architecture. OECT devices can be fabricated using top-gate or bottom-gate configurations, and lateral gate configurations are also possible.[50] Furthermore, the channel structure is not limited to conventional planar geometries, and vertical channel architectures can also be realized.[51, 52]

From a device physics perspective, Bernards and Malliaras established a model describing both the steady-state and transient behavior of OECTs.[48] This “Bernards model” describes the device using coupled electronic and ionic circuit elements (Figure 1.3 c). In this model, the electronic resistance of the channel varies depending on the applied gate potential and the resulting change in hole density due to doping and de-doping processes. Assuming an ideal non-polarizable gate electrode, the ionic circuit can be modeled as a resistor representing the electrolyte and capacitors representing the interfaces between the electrolyte and the channel.

The steady-state drain current in the saturation regime can be expressed as:

$$I_{d,sat} = \mu C^* \frac{Wd}{2L}(V_G - V_T)^2 \tag{1.1}$$

where W, d, and L represent the channel width, thickness, and length, respectively. μ represents hole mobility, and C^*represents the volumetric capacitance of the channel. V_T is the threshold voltage.

Two major figures of merit are commonly used to evaluate OECT performance: ON–OFF ratio and transconductance. The ON–OFF ratio is defined as the ratio of the drain current in the ON state to that in the OFF state:

$$\frac{I_{d,ON}}{I_{d,OFF}} \tag{1.2}$$

Transconductance is another key performance metric and is defined as:

$$g_m = \frac{\partial I_d}{\partial V_G} = \mu C^* \frac{Wd}{L}(V_G - V_T) \tag{1.3}$$

Transconductance corresponds to the slope of the transfer curve and represents the signal amplification capability of the device. This parameter is particularly important for OECT-based sensing applications. To compare intrinsic material performance independent of device geometry and external bias conditions, the product $\mu C^*$is commonly reported as a material-specific figure of merit.[53]

CHAPTER 2 LITERATURE REVIEW

This literature review section focuses on printable soft conductors as key components for wearable electronic devices. Soft wearable electronics consist of multiple functional components that require both electrical conductivity and mechanical compliance. Among these, metal particle-based composites are widely employed as electrodes and interconnects, which are among the most essential elements in wearable electronic systems. PEDOT:PSS can be used as an electrode material for directly sensing physiological signals while interfacing with biological systems. In addition, PEDOT:PSS can function as a semiconducting channel material in OECTs. Although ionic conductors can be used in capacitive sensing applications,[54] this section primarily focuses on gel electrolytes used as gating media in OECTs.

2.1 Conducting composite with metal fillers

In wearable and soft electronics, conducting composites are particularly attractive because they can be engineered to balance electrical performance and mechanical compliance. Metals offer high intrinsic conductivity; however, bulk metals are mechanically rigid and prone to fracture under strain. In contrast, polymer matrices can sustain large deformation but are electrically insulating. Conducting composites seek to combine the advantages of both by embedding metal fillers into a deformable matrix. The composite performance is therefore governed by filler type.

First, gold-based fillers are widely recognized for their exceptional chemical stability and biocompatibility, which makes them attractive for bioelectronics and long-term wearable/skin-contact systems. Au is highly resistant to oxidation and corrosion, which is a significant advantage for devices operating in humid, ionic, or biological environments. Gold conductive inks and composites have therefore been used for printed electrodes, biosensors, and flexible electronic patterns. For example, scalable Au nanoparticle inks have been reported with low resistance (≈9.59 ± 1.2 × 10^{-8} Ω m) after thermal processing at 400 °C for 45 min, illustrating that Au can also be used in printing contexts where stability is prioritized.[55] On the other hand, high-temperature sintering is not required when Au particles are blended with appropriate polymer dispersants. Au nanoparticles can self-assemble within polymer nanocomposites through hydrophilic–hydrophobic interactions, enabling the formation of conductive networks without thermal post-processing. Au composites based on sugar-derived biodegradable polyurethane polymers have demonstrated excellent printability using inkjet printing.[56] This behavior is attributed to the branched structure

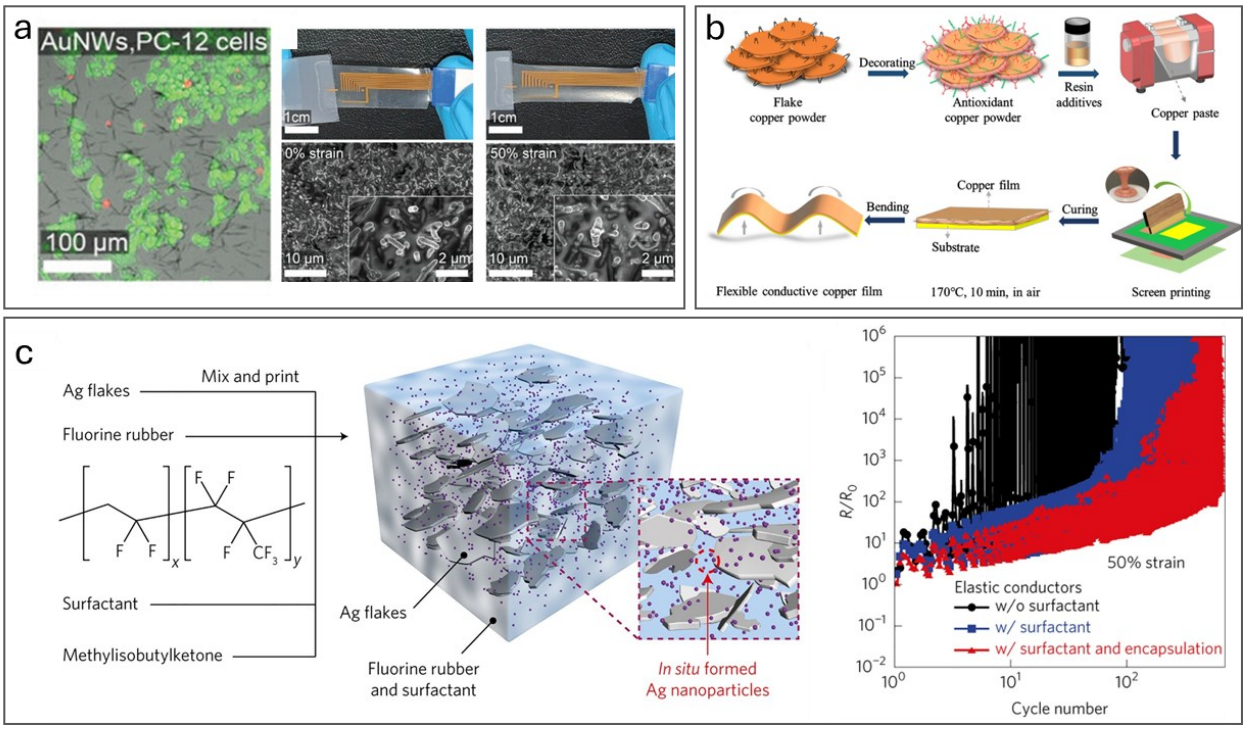

Figure 2.1 a) fluorescence/brightfield merged image of PC-12 cells stained with ethidium bromide (red, dead) and calcein (green, live) in an aqueous Au nanowires (AuNWs) dispersion after 48 h incubation. optical images and scanning electron microscope (SEM) images of printed AuNWs composite. Adapted from Ref.[57] under the Creative Commons CC BY 4.0 license. b) scheme for fabricating antioxidant copper paste and screen printing flexible films. Reproduced from Ref.[61] under the Creative Commons CC BY 4.0 license. c) scheme of Ag flake/particle-based composite and cyclic durability of the composite. Adapted with permission.[64] Copyright © 2017, Springer Nature Limited

of the polymer and its hydrophilic/hydrophobic characteristics, which improve nanoparticle dispersion and ink rheology. The use of different Au particle morphologies has also been investigated. For example, Gold nanowire (AuNW)–silicone composites have demonstrated nerve-like mechanical softness (≈ 250 kPa), high electrical conductivity (≈ 1.6×10^4 S cm^{-1}), and reversible stretchability.[57] The biocompatibility of the AuNW filler was verified through cell viability studies using dyed cells cultured in AuNW dispersions (Figure 2.1a). These non-toxic and mechanically compliant materials have enabled selective functional stimulation and recording of sensory signals in rat sciatic nerves, while also exhibiting long-term operational stability exceeding three years. However, the high cost of Au fillers is often the dominant limitation for practical

implementation, especially in applications involving large-area electrodes or disposable devices, where cost per unit area is critical.[58]

Copper is an attractive alternative filler owing to its high electrical conductivity and significantly lower cost compared to noble metals such as gold. Consequently, copper-filled composites have been widely investigated for printed conductive applications, particularly in systems where low cost and scalability are critical.[59] However, the high susceptibility of copper to oxidation remains a major challenge in both ink formulation and post-processing, as the formation of oxide layers increases interparticle contact resistance and inhibits effective sintering into conductive networks.[60] To address this limitation, antioxidant copper pastes have recently been developed using copper microflakes with surface passivation layers formed by formate ions and thiol molecules (Figure 2.1 b). These materials exhibit high electrical conductivity ($\approx 1.34 \times 10^4$ S cm^{-1}) and have been successfully demonstrated in flexible printed electronic applications, including electromagnetic interference (EMI) shielding films, anti-fog coatings, and radio-frequency identification (RFID) tags.[61]

Lastly, silver is one of the most widely used metallic fillers in conductive composites and printed electronics because it combines very high electrical conductivity (around 6.3×10^5 S cm^{-1}) of bare silver. Ag-based composites typically exhibit electrical conductivities in the range of 10^2 to 10^4 S cm^{-1}.[62] Compared to other metal particles, silver-based inks and composites can often achieve high conductivity with moderate sintering conditions, which is important for temperature-sensitive polymer substrates.[63] Incorporating additives such as surfactants into the polymer matrix can help promote the formation of electrically conductive pathways between Ag particles without requiring high-temperature sintering.

The use of silver particles with different morphologies, including nanoparticles, 2D flakes, and nanowires, has been extensively studied. Silver nanoparticles can rearrange within the polymer matrix, which helps maintain the percolating conductive network and reduces network distortion under mechanical strain (Figure 2.1 c).[64] In addition, combining two different Ag particle morphologies has been shown to further improve both electrical stability and mechanical compliance under strain. [65] Stacked 2D Ag flake structures within composites can help maintain electrical conductivity during mechanical deformation through interflake sliding mechanisms,

which reduce electrical degradation under strain. Meanwhile, high-aspect-ratio Ag nanowires can significantly improve electrical conductivity by forming highly efficient percolated conductive networks.[66] Furthermore, conducting composites incorporating Ag nanowires can exhibit optical transparency while maintaining electrical conductivity, enabling their use as electrodes in stretchable optoelectronic applications.[67]

However, as shown in Figure 2.1c, the electrical properties of Ag-based composites are susceptible to degradation under repeated mechanical deformation. This limitation is common to conducting composites incorporating rigid metal fillers, including Au and Cu. During cyclic stretching, bending, or compressive loading, rigid metal particles may lose electrical contact with neighboring particles or induce microcrack formation within the conductive network. These effects result in an increase in electrical resistance and, ultimately, a degradation of overall electrical performance.[68, 69]

Gallium-based liquid metals (LMs), such as eutectic gallium–indium (EGaIn) and Ga–In–Sn alloys (galinstan), have emerged as attractive alternative metal fillers for conducting composites. In contrast to conventional solid metal fillers, LM fillers remain in a liquid state at or near room temperature, enabling them to accommodate large mechanical deformation while preserving metallic-level electrical conductivity ($\approx 10^6$ S m^{-1}) even under repeated mechanical deformation. Consequently, LM-based soft conductors are considered highly promising materials for stretchable conductors in wearable electronics, where both high electrical conductivity and mechanical compliance are required. However, because gallium and indium are classified as critical materials, increasing attention has been directed toward their efficient use and recycling.[70, 71]

Because LMs are intrinsically soft at around room temperature, pure LM, rather than composite systems, can be considered for direct use in the fabrication of deformable electronic devices. Indeed, numerous studies have reported the direct patterning of bare LM. For example, patterning of bare EGaIn using stencil printing and direct writing techniques has been demonstrated.[72-75] However, due to the high surface tension of EGaIn, printing is generally restricted to specific substrates, particularly silicon oxide-based materials such as glass and polydimethylsiloxane (PDMS). Another approach involves fabricating LM patterns using microfluidic channels, in which LM is introduced into pre-fabricated empty channels using vacuum-assisted filling.[76, 77] However, because microfluidic channel fabrication typically requires complex and multistep

processing, this method can reduce manufacturing throughput. Lithography techniques combined with lift-off processes have also been employed for LM patterning. [78-81] Although lithographic approaches can achieve micron- and submicron-scale linewidth resolution, additional interfacial layers are typically required to improve LM wettability on substrates. Therefore, despite the intrinsic advantages of LM for soft and deformable electronics, the formation of LM composites with polymer matrices represents a practical strategy for rapid, facile, and low-cost patterning of LM on a wide range of substrates, particularly plastic substrates for wearable electronic applications. To overcome these limitations associated with direct LM patterning, composite-based approaches have been developed.

LM composites are typically formed by breaking bulk liquid metal into micro- or nanoscale droplets, which are then dispersed in a fluid medium, such as uncured PDMS (prepolymer) or liquid polymer solutions, through vigorous rotary (shear) mixing[82] or sonication.[83] The resulting suspensions can be formulated as printable inks and processed using various patterning techniques, including stencil printing,[84] spray coating,[85] and direct ink writing, enabling scalable fabrication of stretchable conductive structures. However, as-prepared LM composites typically exhibit low electrical conductivity, as the insulating polymer matrix and the native gallium oxide layer hinder the formation of a percolated conductive network. Therefore, an additional post-treatment step, commonly referred to as activation, is required to establish conductive pathways by breaking these insulating barriers and enabling physical connections between LM droplets.

In prepolymer-based composites, silicone-based elastomers such as PDMS and Ecoflex are commonly used as matrix materials for LM composites in wearable electronics due to their high stretchability, chemical inertness, and biocompatibility.[86, 87] Recently, a silicone-based, water-resistant LM composite exhibiting long-term stability under underwater conditions has been reported.[88] However, the limited solubility of PDMS complicates liquid metal recycling.

LM composites based on polymer solutions have also been extensively investigated. For example, PSS-grafted LM composites fabricated via meniscus-guided direct writing have achieved high-resolution patterning (≈ 50 μm linewidth), high electrical conductivity (1.5×10^4 S cm^{-1}), and stable electromechanical performance. In these materials, electrical resistance increased by only 8% at 200% strain and 40% at 500% strain, indicating excellent electrical stability under large mechanical deformation.[83] Similarly, PVA/LM composites have been developed as highly conductive (1.3

× 10^3 S cm^{-1}) inks suitable for three-dimensional printing on various substrates.[89] These materials have enabled applications in alarm systems, object localization devices, and highly sensitive wearable pressure and motion sensors. Furthermore, the liquid metal component can be recovered through alkaline treatment and reused for subsequent ink preparation, demonstrating the potential for sustainable LM composite processing. However, the polymers used in this type of composites, such as PSS and PVA, are water-soluble, rendering the resulting LM composites vulnerable to aqueous environments.

Despite significant progress, further development is required to realize multifunctional LM composites. In particular, next-generation systems should be compatible with diverse substrates and fabrication techniques while simultaneously achieving electrical stability, mechanical robustness, water resistance, and efficient end-of-life material recovery.

2.2 Printed flexible and stretchable OECTs

As printable conductors and semiconductors have been developed, printed electronics have been extensively investigated. Among various device architectures, OECTs are particularly attractive because they can be fabricated using scalable, low-temperature additive processes that are compatible with plastic substrates. This compatibility enables large-area manufacturing and facile device customization without relying on conventional photolithographic techniques. Simultaneously, extensive efforts have been devoted to modifying conjugated polymer-based channels and electrolytes—key components of OECTs—to enable functional bioelectronic devices for wearable applications.

A milestone for printed OECTs in around 2015 period is the transition from proof-of-concept printing to device optimization and application-oriented characterization. For example, Scheiblin et al. demonstrated screen-printed OECTs for metabolite sensing, which helped establish screen printing as a practical route for producing PEDOT:PSS OECTs with thicknesses and geometries relevant to biosensing.[90] In parallel, Contat-Rodrigo et al. reported the characterization of PEDOT:PSS OECTs fabricated by screen printing on flexible substrates, systematically comparing geometries and investigating ion sensitivity with different cations.[91] This study demonstrates that printing does not merely replicate lithographically fabricated OECTs; rather, the printed device geometry and the printed interfaces (gate/electrolyte/channel) directly influence key device characteristics, including transconductance, current modulation, and ionic selectivity.

Inkjet printing also emerged as a credible alternative for non-contact deposition of OECT components. Afonso et al. investigated inkjet-printed PEDOT:PSS OECTs using highly ion-conducting polymer electrolytes, illustrating how inkjet printing can provide patterned channels with controllable dimensions while shifting constraints toward ink formulation (viscosity/surface tension) and nozzle stability.[92]

Although not specifically focused on stretchable OECTs, numerous studies have explored bioelectronic applications using related material systems and device architectures. Screen-printed OECTs functionalized with enzymes, ion-selective membranes, and bio-recognition elements have also been used as sensors to detect glucose and lactate, ascorbic acid,[93] urea,[94] nutrients in plant sap[95] and DNA.[96]

From the perspective of deformability, all components of a soft OECTs must undergo mechanical strain together with the device during deformation. Conventional OECTs typically employ aqueous electrolytes, such as sodium chloride (NaCl) solutions or phosphate-buffered saline (PBS). These liquid-state electrolytes are generally confined within reservoirs, which makes them susceptible to leakage under various forms of mechanical deformation, such as body motion. In this context, semi-solid gel electrolytes offer a promising alternative, as they can deform in response to external mechanical stimuli without leakage. In addition, unlike liquid electrolytes, gel electrolytes can be patterned using printing techniques, enabling greater design flexibility in device fabrication. Furthermore, such gels can provide a soft interface between electronic devices and biological systems, improving conformal contact and adhesion to tissues.[97]

In addition, gel electrolytes functionalized with bio-recognition elements have been employed for biosensing applications.[94] Two primary classes of gel electrolytes are commonly used in OECTs: ion gels and hydrogels. Ion gels consist of ionic species immobilized within a polymeric matrix. Because ion gels exhibit good mechanical flexibility and thermal stability, they are well suited for flexible electronic applications. Bischak *et al.* utilized an ion gel as an ion exchange layer in a flexible OECT to detect action potentials in a flytrap plant.[98] Gao *et al.* demonstrated synaptic plasticity in ion gel-gated OECTs,[99] as well as long-term synaptic behavior.[100] However, ion gels are generally not biocompatible, particularly those based on imidazolium ionic liquids, which limits their application in bioelectronic systems.[101]

In contrast, biocompatible hydrogels can be fabricated from a wide range of naturally derived, bioinspired, and synthetic polymers, as well as biocompatible salts.[102] Hydrogels also exhibit tissue-like mechanical properties,[103] with Young's moduli ranging from approximately 1 Pa to 300 MPa, spanning the mechanical ranges of biological tissues such as skin and muscle (200–500 kPa), as well as brain tissue and spinal cord (500 Pa–200 kPa).[104] These mechanical characteristics reduce mechanical mismatch with soft tissues, making hydrogels particularly attractive for implantable and wearable bioelectronic applications.

Recently, Wang *et al.* developed stretchable all-polymer OECTs based on biocompatible gelatin hydrogels that function as neuromorphic devices and glucose sensors. Jo *et al.* demonstrated that gelatin electrolyte-based OECTs can be used for pH-modulated electrochemical logic circuits.[105] Ko *et al.* reported self-healing OECTs by incorporating PVA hydrogels into the active channel material to enhance the robustness and durability of wearable bioelectronic systems.[106] More recently, wearable continuous glucose monitoring systems have been realized by integrating hydrogel OECT-based biosensors with microneedle platforms.[107] In this work, the feasibility of continuous glucose monitoring was demonstrated under both in vitro and in vivo conditions.

Despite these advances, the implementation of hydrogel electrolytes in stretchable OECTs remains relatively limited. One limitation is associated with processing constraints. Inkjet printing typically requires low-viscosity inks, whereas screen printing requires high-viscosity inks. However, hydrogels often exhibit rheological properties that fall outside these printable viscosity windows. Consequently, even when the channel and electrodes of OECTs are fabricated using printing techniques, hydrogel electrolytes are frequently cast or manually laminated onto the devices rather than directly printed.[108] A more critical limitation is the tendency of hydrogel electrolytes to undergo dehydration. For the development of long-term stable wearable OECTs, this issue must be effectively addressed.

2.3 Enhanced properties of PEDOT:PSS

PEDOT:PSS is one of the most widely used mixed ion–electron conducting polymers because it combines solution processability, optical transparency, and electrochemical activity. However, the electrical, electrochemical, and mechanical properties of pristine PEDOT:PSS films are often limited by their nanophase-separated morphology, in which PEDOT-rich conductive grains are embedded within a PSS-rich insulating matrix. As a result, charge transport is strongly influenced

not only by the crystallinity and packing of PEDOT within grains, but also by inter-grain connectivity across PSS-rich regions. In addition, hydrophilic PSS domains can absorb significant amounts of water in aqueous environments, which can lead to degradation of both electrical and mechanical properties.[109]

In this context, several strategies have been investigated to improve the performance and environmental stability of PEDOT:PSS for applications as electrodes and OECT channel materials in wearable electronics.

First, to improve the water stability of PEDOT:PSS, crosslinking agents have been incorporated into PEDOT:PSS dispersions. One of the most widely used crosslinkers is (3-glycidyloxypropyl)trimethoxysilane (GOPS). The sulfonic acid groups of PSS can react with the epoxy groups of GOPS, while GOPS molecules can also form crosslinked siloxane networks. Through this crosslinking process, PEDOT:PSS films become stable in aqueous environments. Recent studies have shown that GOPS crosslinking does not significantly affect the oxidation level of PEDOT, thereby preserving the charge carrier density of PEDOT segments. [110] However, crosslinking can modify the microstructure of PEDOT:PSS and reduce charge carrier mobility, which may result in increased electrical resistance.

Second, conductivity enhancement of PEDOT:PSS can be achieved through solvent doping by adding organic polar solvents to the aqueous PEDOT:PSS dispersion. Ethylene glycol (EG), [49] dimethyl sulfoxide (DMSO), [111] and glycerol[112] are among the most commonly used additives. The polar functional groups of these solvents form hydrogen bonds with the sulfonic acid groups of PSS. These interactions weaken the electrostatic interaction between PEDOT and PSS, leading to partial dissolution and redistribution of PSS. As a result, PEDOT chains undergo structural rearrangement and form improved interchain connections, creating more efficient conductive pathways and significantly enhancing electrical conductivity. For bioelectronic applications, such as OECT channels operating in aqueous electrolytes, crosslinkers and solvent dopants are often used simultaneously to achieve both water stability and high electrical conductivity. [113, 114]

Post-treatment using similar organic polar solvents has also been widely investigated. In this process, pre-formed PEDOT:PSS films are soaked in polar solvents. This treatment can reduce the relative PSS content in the film. [115] Because the insulating and hydrophilic PSS fraction is

reduced, electrical conductivity and OECT performance are typically improved, and water stability can also be enhanced. [116, 117]

Strong acid post-treatment can remove excess PSS more effectively than organic solvents. For example, sulfuric acid post-treatment of PEDOT:PSS has been extensively studied. Acid-treated PEDOT:PSS films have demonstrated excellent stability in aqueous environments and superior performance as both sensing and stimulating electrodes, as well as OECT channel materials. [118, 119]

Since PEDOT:PSS is a conjugated polymer composed of polymer chains, the polymer can exhibit anisotropic characteristics depending on chain structure and orientation, i.e., directional dependence of physical and mechanical properties. Electrically anisotropic PEDOT:PSS films have been achieved via a brush-printing technique.[120] The brush-printed PEDOT:PSS/DMSO films exhibit higher electrical conductivity and enhanced power factor along the brushing direction compared to the perpendicular direction. Beyond thin films, PEDOT:PSS has also been investigated in free-standing forms. For example, wet-spun PEDOT:PSS microfibers have been used as OECT channel materials. [121] Due to the anisotropic alignment of PEDOT domains along the fiber axis, fiber-based OECTs exhibit high figures of merit, resulting from enhanced hole mobility along the aligned PEDOT domains. The formation of anisotropic free-standing PEDOT:PSS sheets through wet-winding of PEDOT:PSS fibers has also been reported. [122] These anisotropic conductive sheets have been applied to thermoelectric devices and demonstrated direction-dependent high performance. Highly anisotropic PEDOT:PSS structures have also been achieved through templating approaches. For example, aligned PVA nanofibers prepared via directional freezing have been used as templates, and anisotropic PEDOT:PSS sheets were formed by soaking the aligned matrix in PEDOT:PSS suspension.[123]

Compared to conventional rigid electronics, polymer-based soft devices generally exhibit lower device performance than current industry standards. The anisotropic characteristics of conjugated polymers offer a potential strategy to balance electrical performance and mechanical compliance, thereby improving the performance of soft devices. However, previously reported anisotropic PEDOT:PSS materials are typically bulky and rough, limiting their compatibility with established thin-film device architectures. Thin, smooth, and uniform anisotropic PEDOT:PSS films, which could be seamlessly integrated into conventional device platforms, remain relatively underexplored.

2.4 Research objectives

The importance of wearable devices for remote healthcare monitoring and diagnosis has significantly increased following the global pandemic crisis. Current body monitoring technologies are primarily limited to collecting confined physiological signals from restricted body areas, such as the wrist and fingers. To enable comprehensive monitoring of physiological signals across various regions of the human body, soft wearable devices that can conform to diverse body parts are essential.

Along with the development of wearable electronics, advances in electronic device manufacturing processes should also be addressed. Printing techniques represent a promising manufacturing technology because they directly pattern device components, in contrast to conventional photolithography, thereby enabling rapid fabrication processes. Since printing techniques do not require photoresists or lift-off materials, they offer a low-cost production approach. Furthermore, reduced material waste during fabrication contributes to environmentally friendly and sustainable manufacturing. Digitally controlled printing also enables straightforward customization, facilitating the production of personalized wearable devices tailored to individual users. Based on these advantages, next-generation wearable electronics are expected to increasingly rely on advanced additive manufacturing techniques.

The comprehensive objective of this thesis is to investigate printable soft conducting materials and devices as active components for next-generation wearable electronics.

The first specific objective of this thesis was to investigate printable inks for patterning soft conducting components. Polymers were primarily employed not only to enable solution processability for printability, but also to impart mechanical softness to the printed materials. To achieve this objective, the following tasks were carried out:

- Developed aqueous-based printable gel electrolyte formulations and printed them as gating media for OECT devices.
- Designed and synthesized a polymer ligand to stabilize LM suspensions for use as printable conductive inks.

A DIW printer was employed due to its capability to dispense inks over a wide viscosity range, enabling the patterning of electrodes, interconnects, and OECT components. The performance of

OECTs fabricated using printed gel electrolytes was compared with devices incorporating manually placed gels to verify the advantages of printed gel integration.

The second specific objective was to investigate soft conducting materials and devices capable of functioning reliably under various conditions relevant to healthcare monitoring applications. Wearable devices are frequently subjected to mechanical deformation, such as bending and stretching on the human body. In addition, they are often exposed to aqueous environments arising from biological fluids, sweat, or external environmental conditions such as rainwater. For example, OECTs commonly operate at interfaces between aqueous biological media and electronic systems for sensing applications. Furthermore, the performance of conjugated polymers as active materials in soft wearable electronics must be improved to approach that of their rigid counterparts.

To achieve this objective, the following research tasks were performed:

- Fabricated fully stretchable OECTs using printing techniques and characterized their transfer curves under tensile strain applied in different directions.
- Developed anti-drying gel electrolytes for long-term stable OECT operation and conducted device performance measurements over 50 days.
- Designed and synthesized a polymer matrix for multifunctional LM composites, characterized their electromechanical properties under extreme tensile strain, compared experimental results with theoretical predictions, conducted durability tests under repeated strain in both dry and wet environments, and demonstrated the feasibility of LM composite-based sensors operating underwater.
- Verified the in-plane electrical anisotropy of spin-coated PEDOT:PSS thin films treated with wet-strain processing using four-point probe measurements along different directions.

2.5 Structure of the thesis

Chapter 1 provides background information on current wearable electronics and key considerations for the development of future wearable devices. It also introduces printing techniques as promising manufacturing strategies for soft electronic systems.

Chapter 2 reviews recent advancements in conducting components for soft electronics and gel electrolyte-based OECTs. In addition, it discusses various approaches to enhance the properties of PEDOT:PSS, one of the most widely used materials in wearable and bioelectronic applications.

Chapters 3, 4, and 5 of this thesis consist of journal articles in which the author is listed as the first author.

Article 1:

Chi-Hyeong Kim, Mona Azimi, Jiaxin Fan, Harini Nagarajan, Meijing Wang and Fabio Cicoira, "All-printed and stretchable organic electrochemical transistors using a hydrogel electrolyte", *Nanoscale, 2023,15,3263,* DOI:10.1039/D2NR06731E

Article 2:

Chi-hyeong Kim, Jinsil Kim, Jiaxin Fan, Meijing Wang, Fabio Cicoira, "Recyclable Printed Liquid Metal Composite for Underwater Stretchable Electronics", *Small Science*, 2025, 5, 2400553, DOI:10.1002/smsc.202400553

Article 3:

Chi-hyeong Kim and Fabio Cicoira, "In-Plane Electrical Anisotropy in PEDOT:PSS Thin Films Induced by Wet-Strain Treatment", *MRS Advances*, submitted

Chapter 6 summarizes the conclusions drawn from the work presented in the previous chapters. In addition, it provides recommendations and perspectives for future research directions in the field, building upon the findings and insights obtained from this study.

CHAPTER 3 ARTICLE 1: ALL-PRINTED AND STRETCHABLE ORGANIC ELECTROCHEMICAL TRANSISTORS USING A HYDROGEL ELECTROLYTE

Chi-Hyeong Kim, Mona Azimi, Jiaxin Fan, Harini Nagarajan, Meijing Wang and

Fabio Cicoira*

Department of Chemical Engineering, Polytechnique Montréal, Montréal,

Québec H3C 3A7, Canada

* Corresponding author: fabio.cicoira@polymtl.ca

Nanoscale, Received 1st December 2022, Published 17th January 2023

3.1 Abstract

Stretchable electronic devices are expected to play an important role in wearable electronics. Solution-processable conducting materials are desirable because of their versatile processing. Herein, we report the fabrication of fully stretchable organic electrochemical transistors (OECTs) by printing all components of the device. To achieve the stretchability of the whole body of the devices, a printed planar gate electrode and polyvinyl alcohol (PVA) hydrogel electrolyte were employed. Stretchable silver paste provided a soft feature to drain/source, gate and interconnect, without any additional strategies needed to improve the stretchability of the metallic components. The resulting OECTs showed a performance comparable to inkjet or screen-printed OECTs. The maximum transconductance and on/off ratio were 1.04 ± 0.13 mS and 830, respectively. The device was stable for 50 days and stretched up to 110% tensile strain, which makes it suitable for withstanding the mechanical deformation expected in wearable electronics. This work paves the way for all-printed and stretchable transistors in wearable bioelectronics.

3.2 Introduction

Stretchable electronics have gained increasing attention for their great potential in the field of bioelectronics. Stretchability is critical for applications which require intimate contact with curved surfaces or susceptibility to mechanical deformation, such as artificial skin, implantable electronics, and wearable health monitoring devices.[124-126] On-skin wearable electronics

should conform to the skin and tolerate mechanical deformations, including bending, twisting, and stretching, with tensile strains of around 30%.[36, 127] Stretchable electronics can be achieved mainly by two different approaches: (i) integrating rigid functional devices with stretchable interconnects and (ii) patterning devices with stretchable components.[128, 129] Organic semiconducting and conducting polymers have been extensively employed for stretchable electronics owing to their softness, low-temperature processibility, tunable chemical and electrical properties, and, in some cases, ability to be combined with soft and stretchable materials.

Organic electrochemical transistors (OECTs) are widely explored for bioelectronics, due to their low operation voltages (<1 V) and intrinsic signal amplification. Several studies have demonstrated that OECTs are suitable for stretchable bioelectronics.[130-132] An OECT consists of a conducting polymer channel connected to source and drain electrodes in ionic contact with a gate electrode via an ionic medium (liquid or gel). The channel current is modulated by the gate voltage through reversible electrochemical doping/de-doping of the conducting polymer. Poly(3,4-ethylenedioxythiophene)polystyrene sulfonate (PEDOT:PSS) is the most widely used OECT channel material due to its high electrical conductivity, solution processability, and biocompatibility.[118] Although conducting polymers (e.g. PEDOT:PSS) can be patterned with photolithography,[133] printing technologies are well-suited for fabricating OECTs, since they permit to pattern the metal contacts and the channel with the same equipment and easily allow to modify the device layout.[134]

For all-printed OECTs, inkjet printing allows the patterning of the components with a relatively high resolution.[135, 136] Inkjet printing was employed to fabricate fully printed OECTs with a PEDOT:PSS channel and a graphene gate, used as enzymatic glucose sensors.[137] A water-soluble p-type conjugated polymer, P(DPP-DTT-MS), was inkjet-printed as an active layer of OECTs.[138] Screen printing is faster than inkjet and facilitates mass production.[139] Andersson Ersman et al. developed screen-printed PEDOT:PSS based OECTs on flexible substrates for applications in logic circuits, such as NAND gates, multiplexers[140] and inverters operating at relatively high frequencies,[141] and display driver circuits integrated with organic electrochromic displays.[142] Screen-printed OECTs functionalized with enzymes, ion-selective membranes, and bio-recognition elements have also been used as sensors to detect glucose and lactate,[90] ascorbic acid,[93] urea,[94] nutrients in plant sap[95] and DNA.[96] Although several flexible OECTs have

been fabricated by printing technologies, only a few studies on printed stretchable OECTs have been reported.

For applications requiring a longer device operation, aqueous electrolytes, commonly used for gating OECTs, can be replaced by printable gels containing ions.[143-146] Such gels may also provide a soft interface between electronic devices and biological systems, which improves contact and adhesion on tissues.[97, 147] OECTs based on gel electrolytes have been employed for logic circuits, which can be integrated with biosensors to process detected signals.[148] In addition, a gel electrolyte functionalized with bio-receptors has been used for biosensing.[94] Two main classes of gel electrolytes are commonly used in OECTs: ion gels and hydrogels. Ion gels consist of an ionic immobilized into a polymeric matrix. Since the ion gels are mechanically bendable and thermally stable, they are suitable for flexible electronics. Bischak et al. utilized an ion gel as an ion exchange layer and used a flexible OECT to sense action potential in a flytrap plant.[98] Gao et al. reported synaptic plasticity of ion gel gated OECTs[99] and their long-term synaptic behavior.[100] Ion gels are not generally biocompatible, especially imidazolium-based ones, which prevents their use in bioelectronics,[101, 149] whereas biocompatible hydrogel can be fabricated from a wide range of naturally sourced, bioinspired and biocompatible materials.[102] Hydrogel also show tissue-like mechanical properties,[103] with Young's moduli ranging from 1 Pa to 300 MPa, covering the typical values for skin and muscles (200–500 kPa), brain tissue, and spinal cords (500 Pa–200 kPa).[104] Such mechanical properties minimize the mechanical mismatch with soft tissues, making hydrogels ideal candidates for implants and wearable bioelectronics. Recently, Wang et al. developed stretchable all-polymer OECTs based on biocompatible gelatin hydrogels working as neuromorphic devices and glucose sensors.[102] Jo et al. showed that gelatin electrolyte-based OECTs can be used for pH-modulated electrochemical logic circuits.[105] Ko et al. demonstrated self-healing OECTs by introducing poly(vinyl alcohol) hydrogel to the active channel material.[106] Liu et al. reported OECTs with a dual network anti-freezing hydrogel composed of crosslinked polyacrylamide and carrageenan,[150, 151] able to operate at −30 °C. They also studied the neuromorphic behavior and transient response of the devices. However, the use of hydrogel electrolytes applied to stretchable OECTs remains largely unexplored. This is likely because inkjet and screen printing are not suitable to print hydrogels, as they require inks within specific viscosity ranges (i.e., inkjet printers require low viscosity, whereas screen printers

require high viscosity). Therefore, even when the channel and the electrodes of the OECTs are printed, hydrogel electrolytes are typically casted or manually attached on the devices.[106, 108]

In this study, we fabricated all-printed and stretchable OECTs on stretchable thermoplastic polyurethane (TPU), using a printed circuit board (PCB) printer. Devices gated with hydrogels exhibited performance similar those gated with aqueous gating media and were operated up to 50 days, maintaining the transconductance at around 60% of its initial value. The devices show a stretchability of ≈60% along the channel direction and of ≈150% in the perpendicular direction. This study contributes to the improvement of long-term stability and stretchable characteristics of OECTs, with possible applications in printed biosensors.

3.3 Experimental details

3.3.1 Materials

PEDOT:PSS screen-printing ink (Clevios SV3 STAB, Heraeus, Germany) was purchased from Heraeus (700 Ohm sq^{-1} sheet resistance declared by the supplier). According to the data supplied by the company, the ink contains a significant amount of propane-1,2-diol, 2-2′-oxydiethanol and other additives in lower concentrations. Screen-printing thermoplastic silver (Ag) ink (Ag paste 520 EI) was donated by Chimet S.p.A (Italy). Thermoplastic polyurethane (TPU) on removable silicon paper (Elecrom Stretch White, thickness of 80 μm) was purchased from Policrom Screens (Italy). A silicone elastomer kit (SYLGARD® 184), used to prepare polydimethylsiloxane (PDMS), was purchased from Dow Corning. Polyvinyl alcohol (PVA, M_w 89–98 kDa) and NaCl (≥99.5%) were purchased from Sigma-Aldrich. Dimethyl sulfoxide (DMSO) and glycerol were purchased from Caledon Ltd. Sodium hypochlorite (NaClO) solution (5% w v^{-1}) was purchased from LabChem, Inc. Ag/AgCl (E202) pellet electrode was purchased from Warner Instruments.

3.3.2 Preparation and characterization of hydrogel gating media

Three types of PVA-based hydrogels containing NaCl (Table 3.1) were used as the gating media and were either printed or manually placed on the transistor channel. PVA (13 wt%) was dissolved in a 0.1 M NaCl aqueous solution (PVA hydrogels) at 85 °C under vigorous stirring. As drying over time of hydrogels may hinder the long-term stable operation of OECTs,[152] we prepared hydrogels using mixtures of water with DMSO (normal boiling point 189 °C) and glycerol (normal

boiling point 290 °C), which are known to raise the water boiling point.[102, 153] To prepare these gels, 13% PVA and the equivalent of 0.1 M NaCl were dissolved in water mixed with 30 v/v%, DMSO (hydrogel named D_PVA) and 45 v/v% glycerol (named G_PVA) at 85 °C under vigorous stirring. The amounts of DMSO and glycerol were selected because they yielded a mechanically stable hydrogel.

Hydrogel	PVA (wt%)	H2O (v/v%)	Glycerol (v/v%)	DMSO (v/v%)
PVA	13	100	0	0
G_PVA	13	55	45	0
D_PVA	13	70	0	30

Physical crosslinking of PVA hydrogel was achieved with a freezing and thawing process, by drop-casting the precursor solution on a Petri dish, freezing at −15 °C for 12 hours, and thawing at room temperature.[154]

Table 3.1 Composition and names of the hydrogel electrolytes used in this work

Electrochemical impedance spectroscopy (EIS) of hydrogel electrolytes was carried out in a Swagelok cell (Beyond Battery) with a VERSASTAT 4 (Princeton Applied Research) potentiostat. The drop-casted hydrogel electrolytes (2 mm thickness) were cut in round shapes and loaded between stainless steel electrodes in a Teflon™ body (inner diameter: 13 mm). EIS was carried out with AC voltage of 10 mV in frequency range 10^5–10^{-1} Hz. The ionic conductivity (σ) which was calculated with the following equation:

$$\sigma = \frac{d}{R_b S} \tag{3.1}$$

where d is the thickness of the hydrogel, S is the contact area between the hydrogel and the electrode of the cell, R_b is the bulk resistance, which is equal to the value of the real impedance in the high frequency region (>10^3 Hz).

The mechanical tensile properties of hydrogels were measured using a mechanical tester (Mach-1 v500csst, Biomomentum Inc., Canada). Samples in dog-bone shapes (≈1 mm thickness, ≈3.2 mm width, ≈15 mm length) were stretched at 0.3 mm s^{-1} strain rate.

3.3.3 OECT fabrication

OECTs were patterned on the stretchable TPU substrates with a PCB printer (Voltera V-One), already used by our group to pattern devices on flexible polyethylene terephthalate.[155] The TPU substrates were cleaned with deionized water (DIW), dried using an air-blowing gun and attached to a glass slide (Corning®) with double-sided tape (3 M) to facilitate handling. The stretchable Ag ink, used to pattern gate, source and drain electrodes, was homogenized in a sonicator (CPX2800, Fisherbrand™) for 15 min before use. The Ag/AgCl gate was obtained by patterning the gate electrode, baking at 120 °C for 20 min on a hotplate (Corning®), and bleaching with a 5% NaClO solution for 1 hour. The Ag source and drain electrodes were then patterned next to the Ag/AgCl gate and baked at 120 °C for 20 minutes. The PEDOT:PSS ink was homogenized in the sonicator and filtered using a syringe filter (CHROMSPEC UV Syringe Filters, 5.0 μm pore size) before printing. PEDOT:PSS channels were printed between the source and drain electrodes (channel dimensions: width $W = \approx 1$ mm, length $L = \approx 1.5$ mm, thickness $d = \approx 1$ μm) and baked at 120 °C for 30 min. PDMS (silicone elastomer with a curing agent at a ratio of 10 : 1, mixed for 3 min at 2000 rpm in a centrifugal mixer) was printed over the Ag electrodes and then cured at 120 °C for 30 min on a hotplate. This step is necessary to prevent faradaic reactions between the Ag electrodes and the electrolyte. The hydrogel ink was printed on the top of the channel and the gate electrode (Figure 3.1 a). To achieve crosslinking of the hydrogels, the devices were kept in freezer at −15 °C for 12 hours and thawed at room temperature. To prepare hydrogel electrolytes manually placed on OECTs, the hydrogel inks were drop-casted and gelled by the freezing and thawing process described above. The gel electrolyte solidified on the Petri dish was cut into rectangles (≈1.5 × 1.5 cm^2) and placed on the printed devices.

The thickness of the electrodes and the PEDOT:PSS channels were derived from the cross-section images of field-emission scanning electron microscopy (FE-SEM, JEOL, JSM-7500F).

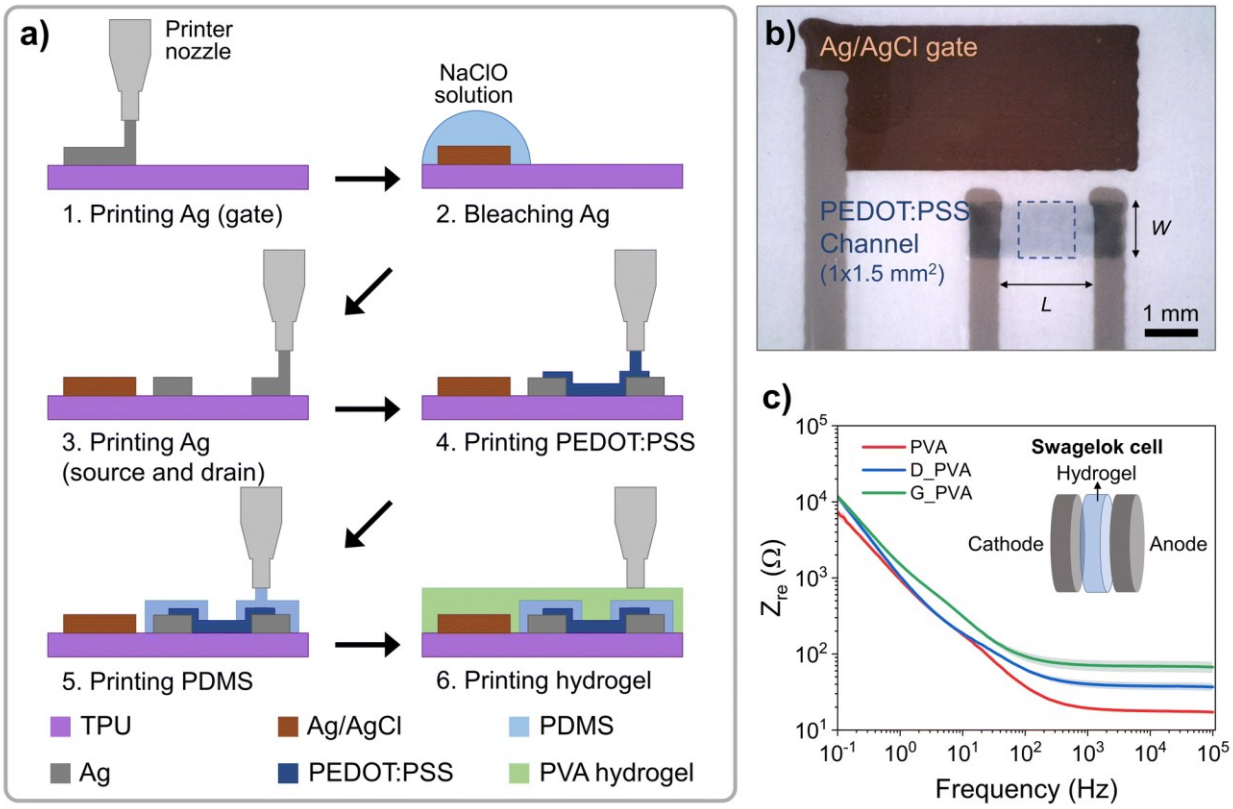

Figure 3.1 (a) Process flow to fabricate the printed OECTs. Step 1: printing stretchable Ag paste as gate electrode on TPU substrate. Step 2: bleaching the printed Ag with NaClO solution to form Ag/AgCl on the surface (thickness ≈20 μm including a ≈5 μm AgCl layer). Step 3: printing the Ag source, drain, and interconnects (thickness ≈20 μm). Step 4: printing of the PEDOT:PSS channel (thickness ≈1 μm). Step 5: printing PDMS to cover source, drain, gate interconnects and the overlap region of PEDOT:PSS with Ag. Step 6: printing hydrogel electrolytes over the gate and channel. (b) Microscopic image of the device. The dashed area indicates the area of the channel (1×1 mm^2), which is not covered by PDMS. (c) Electrochemical impedance (Z_{re}) of the PVA-based hydrogel electrolytes from 10^5 to 10^{-1} Hz, using Swagelok cell. The solid lines are the average values measured from 3 different samples and the shaded area shows the error bars, which represent standard deviation. Since the standard deviation is very small, the shaded area is imperceptible in the graph.

3.3.4 Device characterization

Electrical measurements were performed using an Agilent B1500A source/measure unit (SMU) under ambient conditions. For transfer characteristics (I_D vs V_G), the drain current (I_D) was recorded at a fixed drain–source voltage (V_D) of −0.4 V, while the gate voltage (V_G) was swept from −0.6 V to 1 V. To obtain the output characteristics (I_D vs V_D), V_D was gradually changed from 0 V to −0.8 V, while V_G was varied from −0.6 V to 0.8 V in 0.2 V steps for every V_D sweep. The I vs V characterizations were performed at a scan rate of 20 mV s^{-1}, and the data points were recorded for every 0.01 V step. The transconductance ($g_m = \Delta I_D/\Delta V_G$) of the OECTs was extracted from their transfer curves. Normalized g_m values were obtained by dividing g_m by dimension factors Wd/L.

The switching response of the OECTs was measured using a PXIe-4141 source/measurement unit controlled by LabVIEW software. A gate voltage pulse (ΔV_G = 0.7 V) was applied for 30 s, followed by a 0 V bias maintained for a relaxation time of 80 s while keeping V_D = −0.4 V. For the operational stability test, 500 cycles at 0.4 V gate pulse for 20 s and 0 V for 30 s were done while applying a V_D of −0.4 V.

3.3.5 Electromechanical characterization

The electromechanical properties of the printed stretchable Ag electrodes (15 mm × 1 mm) on TPU were measured using a mechanical tester (Mach-1 v500csst, Biomomentum Inc., Canada) coupled with a Keysight B2902A SMU. The Ag electrodes were stretched parallel to their long direction at a rate of 10% per second.

Stretchable OECTs (channel dimensions of $W = L$ = 8 mm) were measured using a LabVIEW-controlled homemade tensile tester coupled with an Agilent B2900A SMU. In the cyclic strain test, the OECTs were repeatedly stretched and released 1000 times at 30% strain at a rate of 0.2 mm s^{-1}.

3.4 Results and discussion

3.4.1 Fabrication of all-printed and stretchable OECTs

The process flow for OECT fabrication is shown in Figure 3.1a and microscopic image of a printed stretchable OECT is shown in Figure 3.1b. The electrodes were printed using a stretchable Ag ink formulation, instead of using strategies to make rigid electrodes stretchable, such as pre-

stretching[156, 157] or 3D-wavy structures on soft substrates.[132, 158] The Ag electrodes exhibited good stretchability (Figure A.1a), with no significant failures observed below ≈250% strain (Figure A.1b). The resistance of the Ag lines increased ≈10 times at ≈30% strain and remained stable during stretch-release cycles from 0% and 30% (Figure A.1c). The electrodes show a thickness of ≈20 μm, which, in the case of the gate, includes a ≈5 μm AgCl layer (Figure A.2a). The thickness of the PEDOT:PSS channel is ≈1 μm (Figure A.2b). The D_PVA and G_PVA hydrogel electrolytes were stretchable up to ≈500% strain and showed Young's moduli of ≈190 kPa and ≈350 kPa, respectively (Figure A.3). These mechanical properties are suitable for application in stretchable OECTs.

Electrochemical impedance spectroscopy (EIS) was carried out to evaluate the ionic conductivity of the hydrogels (Figure 3.1c). The hydrogels show similar impedance in the low frequency range (<10 Hz). In the high frequency range (>10^3 Hz), D_PVA (≈40 ohms) and G_PVA (≈70 ohms) showed higher impedances than PVA (≈20 ohms). This means that, D_PVA (≈0.05 S cm^{-1}) and G_PVA (≈0.03 S cm^{-1}) possess low ionic conductivities with respect to PVA (≈0.10 S cm^{-1}). Hydrogel electrolytes consist of aqueous solution swollen within a porous polymer network, where hydrated ions can migrate through continuous aqueous pathways. In such systems, the ionic conductivity of hydrogel electrolytes can be influenced by multiple factors. Since all hydrogels characterized by EIS contained the same salt type and concentration, the observed differences in ionic conductivity can primarily be attributed to differences in ion mobility. One of the key parameters governing ion mobility is the ion diffusion coefficient, which is inversely proportional to the viscosity of the aqueous medium. At room temperature, DMSO (≈1.99 cP) and glycerol (≈945 cP) exhibit higher viscosities than water (≈0.89 cP); therefore, ions in hydrogels containing DMSO or glycerol are expected to migrate more slowly through the aqueous pathways.[159] Consequently, the ion mobility in D_PVA and G_PVA may be lower than that in PVA, resulting in reduced ionic conductivity. In addition, this behaviour is likely caused by intermolecular interactions between the glycerol or DMSO molecules and hydrated ions. Both glycerol and DMSO have hydroxyl groups, potentially interacting with hydrated cations through hydrogen bonding and electrostatic forces, interfering with the ion transport in the hydrogel electrolyte.[160, 161] It can be expected that these electrochemical properties have an effect on the transient behaviour of the OECTs.

3.4.2 OECT I vs V characteristics

All printed OECTs exhibited p-type depletion mode operation, as expected for PEDOT:PSS.

The figures of merit of the OECTs using the four types of electrolytes are summarized in Table 3.2. The transfer characteristics (I_D vs V_G) obtained from the average of four devices for each electrolyte (Figure 3.2a), and the output characteristics (Figure 3.2b and Figure A.4) reveal that hydrogel-gated OECTs show comparable performance to those using an aqueous electrolyte gated with a pellet Ag/AgCl electrode (Figure A.5). Devices with printed and manually attached PVA hydrogels show very similar characteristics (Figure A.6). These results prove that our printing technology allows rapid patterning of devices with state-of-the-art characteristics. The backward sweeps of the transfer curves show similar hysteresis characteristics regardless of the electrolyte (Figure A.7). For all devices the maximum transconductance (g_m) is ≈1 mS (at V_G = 0.1 V). The output current show similar values at the same applied voltages and the threshold voltages are ~ 0.6 V. The capacitance and the charge carrier mobility of the semiconducting channel and applied gate potential between the electrolyte and the channel mainly contribute to the steady state performance of OECTs. Therefore, it is expected that devices with the same channel, gate electrode and electrolyte ion concentration show similar behavior. The negligible difference in the I vs V

characteristics of the OECTs may be attributed to the influence of freezing-thawing process or anti-drying agents in the hydrogel electrolytes.

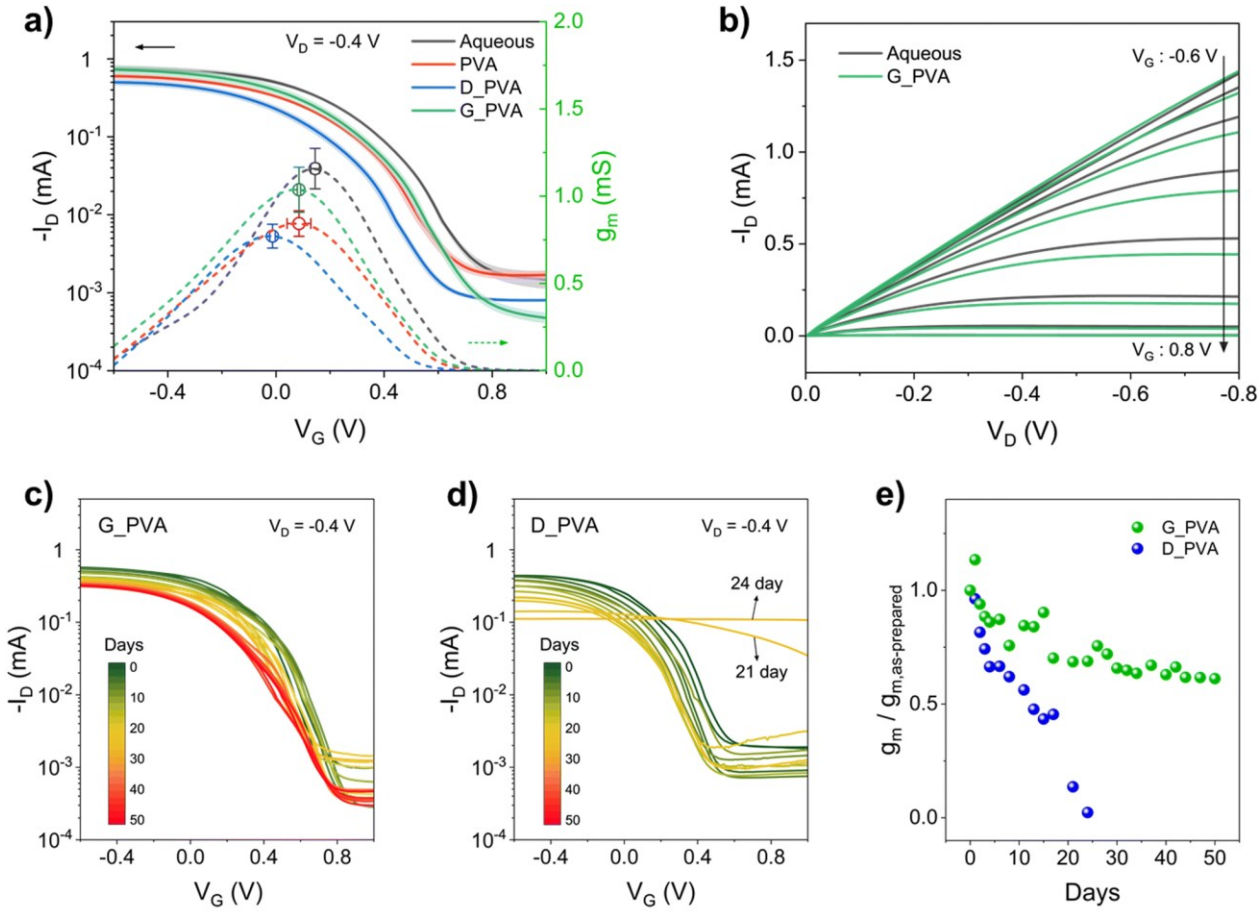

Figure 3.2 OECT current–voltage characteristics. (a) Transfer (solid line) and transconductance (dashed line) curves with 4 types of electrolytes; NaCl 0.1 M aqueous solution (black), PVA hydrogel (red), D_PVA (blue), and G_PVA (green). The solid curves represent the mean values of four device measurements for each electrolyte and the shaded areas indicate the error. The points at each maximum transconductance are plotted with error bars, which represents standard deviation. (b) Output curves obtained with aqueous electrolyte and G_PVA. Long-term stability tests of (c) D_PVA and (d) G_PVA hydrogel-based OECTs. (e) The ratio of transconductances extracted from (c) and (d) with respect to the g_m of as prepared (day 0) OECT. (Blue circle: D_PVA, green circle: G_PVA). For transfer characteristics (I_D vs V_G), the drain current (I_D) was recorded at a fixed drain–source voltage (V_D) of −0.4 V, while the gate voltage (V_G) was swept from −0.6 V to 1 V. To obtain the output characteristics (I_D vs V_D), V_D was gradually changed from 0 V to −0.8 V, while V_G was varied from −0.6 V to 0.8 V in 0.2 V steps for every V_D sweep.

Table 3.2 Figures of merits of all-printed OECTs. The average values in this work were calculated from the results of 4 different samples for each type of electrolyte. Error values represent standard deviation. Dimensionally normalized g_m in this work and other references was calculated from the transconductance and the channel dimension (Wd/L) given in the references

Printing method	Channel material	Electrolyte	W/L/d (μm)	On/off ratio	g_m (mS)	Dimensionally normalized g_m (S cm^{-1})	Time constant τ (ms)	Ref.
PCB (direct-ink write)	PEDOT:PSS	NaCl solution	1000/1000/1	350 ±30	1.2 ± 0.1	17.4 ± 1.7	14.5 ± 2.7	This work
		PVA		150 ±10	0.9 ± 0.1	12.8 ± 1.4	20.7 ± 3.5	
		D_PVA		280 ±20	0.8 ± 0.1	11.6 ± 1.0	41.8 ± 8.0	
		G_PVA		830 ±80	1.0 ± 0.1	15.6 ± 1.9	156.4 ± 26.0	
Inkjet	PEDOT:PSS	cellulose-lithium-based hydrogel	1000/500/0.208	46	0.06	5.77	N/A	[162]
	P(DPP-PTT-MS)-PE cleaved	PVDF-HFP /[EMIM][TFSI]	2000/200/0.05	N/A	0.8	2.2	N/A	[138]
	PEDOT:PSS	PBS solution	1000/3000/1	N/A	≈1	30	N/A	[137]
	PEDOT:PSS	PEO_{25}/LiTFSI	2000/3000/N/A	175	1.67	N/A	N/A	[92]
Screen	PEDOT:PSS	PBS solution	2000/3000/0.28	N/A	0.004	0.21	N/A	[96]
	PEDOT:PSS	KCl solution	700/700/2.5	N/A	5	20	N/A	[95]
	PEDOT:PSS	Chitosan-based sol-gel	500/5000/0.5	N/A	0.017	3.4	N/A	[90]
3D	PEDOT:PSS	NaCl solution	953/417/9	775	43.32	20.91	N/A	[163]
	PEDOT:PSS	NaCl solution	178/118/7.1	1330	31.8	27.99	N/A	[164]

To long-term stability of the G_PVA and D_PVA devices was evaluated by measuring the devices consecutively for several days after fabrication and storage under ambient conditions. Devices using G_PVA as a gating medium worked until the 50th day. The I_D at $V_G = -0.6$ V decreased from ≈0.6 mA to ≈0.3 mA after 40 days and then remained stable until the 50th day (Figure 3.2c). The transconductance (g_m) converged to about 60% of its initial value on the 50th day (Figure 3.2e). For

the D_PVA OECT (Figure 3.2d), the on-current gradually decreased until the hydrogel was dehydrated and partially delaminated on the 21st day, and completely dried on the 24th day. As shown by the data above, the device degradation over time mostly depends on drying of the hydrogels, although smaller contributions from the degradation of PEDOT:PSS cannot be totally excluded.

3.4.3 Transient behavior of the OECTs

To investigate the switching speed of OECTs, we measured the OECT transient responses (Figure 3.3a and Figure A.8). It is worth noticing that the ON–OFF (dedoping) is faster than the OFF–ON (doping) response. This behavior may be attributed to the slow migration of the cations trapped in the PEDOT:PSS films below the protective PDMS layer (Figure A.9a) when the device is on the OFF state. This assumption is supported by the faster OFF–ON switching in absence of the PDMS protective layer (Figure A.9b). Therefore, we analyzed the ON–OFF response to study the switching properties of the devices. The 4th spike was selected to allow pre-conditioning of the devices and fitted using an exponential decay model to extract the time constants. Since the monolithic decay model was unfitted with the measured I_D, a triple exponential decay model was employed, based on the following equation:[165]

$$I_D(t) = I_0 - I_1 \exp\left(-\frac{t}{\boldsymbol{\tau_1}}\right) - I_2\, exp\left(-\frac{t}{\boldsymbol{\tau_2}}\right) - I_3\, exp\left(-\frac{t}{\boldsymbol{\tau_3}}\right) \tag{3.2}$$

where t is time, and I_0 is the initial drain current. I_1, I_2, and I_3 are the current coefficients for fitting. $\boldsymbol{\tau_1}$, $\boldsymbol{\tau_2}$, and $\boldsymbol{\tau_3}$ are the time constants for the dedoping process (results of the fitting shown in Figure 3.3b). The triple exponential decay of the drain current may be ascribed to different ion and charge carrier transport contributions within the device, such as de-doping the channel under the applied gate bias, holes transport within the channel between source and drain, and the delayed re-doping due to PDMS insulator overlapping with the PEDOT:PSS layer. A correlation of the exact mechanism with each specific time constant and current coefficient would require more extensive studies. The weight averages of the time constants for all four types of OECTs were calculated with the following equation:[166]

$$\tau = \frac{I_1\tau_1 + I_2\tau_2 + I_3\tau_3}{I_1 + I_2 + I_3} \tag{3.3}$$

The results of the arithmetic mean time constants acquired from three different devices for each electrolyte type are reported in Table 3.2. The time constants indicate the speed of de-doping process in the channel. The fastest dedoping occurs in devices using aqueous electrolytes. A higher time constant is found for PVA OECTs, likely due hindered transport of hydrated cations due to an increase in ionic resistance.[167] Unlike the aqueous electrolyte, the PVA electrolyte contains a porous polymer mesh that imposes additional constraints on ion transport pathways, likely increasing ionic resistance by restricting ion migration.[168] The D_PVA and G_PVA OECTs showed larger time constants. This behaviour is consistent with the lower ionic conductivity of D_PVA (≈5 S cm^{-1}) and G_PVA (≈3 S cm^{-1}) with respect to PVA (≈10 S cm^{-1}), which may be caused by the higher viscosities of the solutions within the hydrogels, as well as intermolecular interactions between hydrated ions and DMSO or glycerol. In the transient behaviour of OECTs, the drain current can be characterized with ion and hole (or electron) transit time.[48] In our case, hole transport in the PEDOT:PSS layer is expected to be nearly the same since the OECTs have the same channel material. The current based on ion transport in the electrolytes dominantly influences the difference between the time constants of the electrolytes. Ion mobility and ion concentration mainly contribute to Ionic conductivity.[169]60 Since the ion concentration in the hydrogel electrolytes is the same, the smaller ionic conductivity of the D_PVA and G_PVA likely leads to slower ion transport and larger ion transit time, which reflects the value of the time constants found for our OECTs of OECTs. Therefore, G_PVA based OECTs show characteristics that are more suitable for applications that do not require rapid monitoring.

The operational stability test of the G_PVA OECTs was performed with trains of gate-potential pulses for 7 h (Figure 3.3c). Although the ON current during the last cycles decreased by ≈50% compared to the initial value, the average ON/OFF ratio for the last five cycles increased only of about 10% with respect to the first five cycles. This indicates that G_ PVA OECTs are capable of continuous operation over a long period.

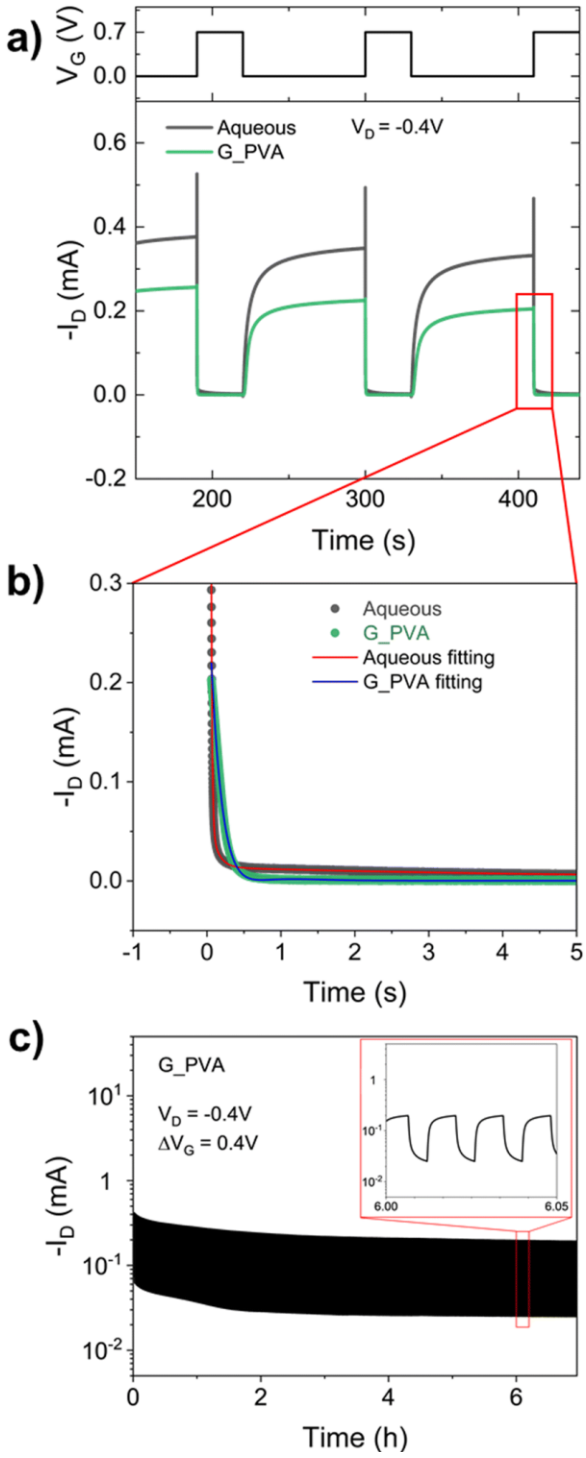

Figure 3.3 Transient response of OECTs. (a) Source–drain current spikes of aqueous and G_PVA electrolytes. A 0.7 V gate pulse was applied for 30 s and 0 V bias was maintained for 80 s as the relaxation time. (b) Fitting with triple decay exponential model. (c) Operational stability test of G_PVA with 500 cycles of between 0 V and 0.4 V gate potential pulse for 20 s and relaxing time for 30 s. The inset is a magnified plot from 6 h for 3 min.

3.4.4 OECT operation under strain

To evaluate the stretchability of the printed OECTs and their stability under strain, bi-axial electromechanical tests were conducted using G_PVA OECTs, as they exhibit the most stable long-term performance. When stretched by 10% increments in the length direction of the PEDOT:PSS channel (parallel strain, Figure 3.4a and b), the OECTs can withstand strains up to 60%. As the OECT was stretched to 50%, the ON current and the maximum g_m gradually decreased to ≈60% and ≈70% of their initial values, respectively. The two values at 60% strain further decreased to ≈20% and ≈40%. The ON/OFF ratio of the stretched OECT remained ≈100 up to 50% strain. The electrical connection of the device was interrupted at 70% strain, and cracks in the width direction of the channel were found on the PEDOT:PSS film (Figure A.10). The device released from 70% to 0% strain showed the same performance as the 60% stretched OECT (dashed line in Figure 3.4b). When the device was released, the physical contact of the cracked PEDOT:PSS films led to the recovery in the electrical connection. Applying the strain in the width direction of the PEDOT:PSS channel strains (perpendicular strain, Figure 3.4d and e), led to a decrease of the ON current and an increase of the OFF current. At approximately 120% strain, the g_m decreased significantly. The ON/OFF ratio of the OECT was reduced below 10^2 while stretching more than 70% and decrease to less than 10 under 120%. The cracks in the PEDOT:PSS film were in this case parallel to the channel. Overall, our results show that the OECTs are sufficiently strain-insensitive up to 50% for parallel and up to 100% for perpendicular strain. These properties are very promising for applications in wearable and on-skin electronics.[36]

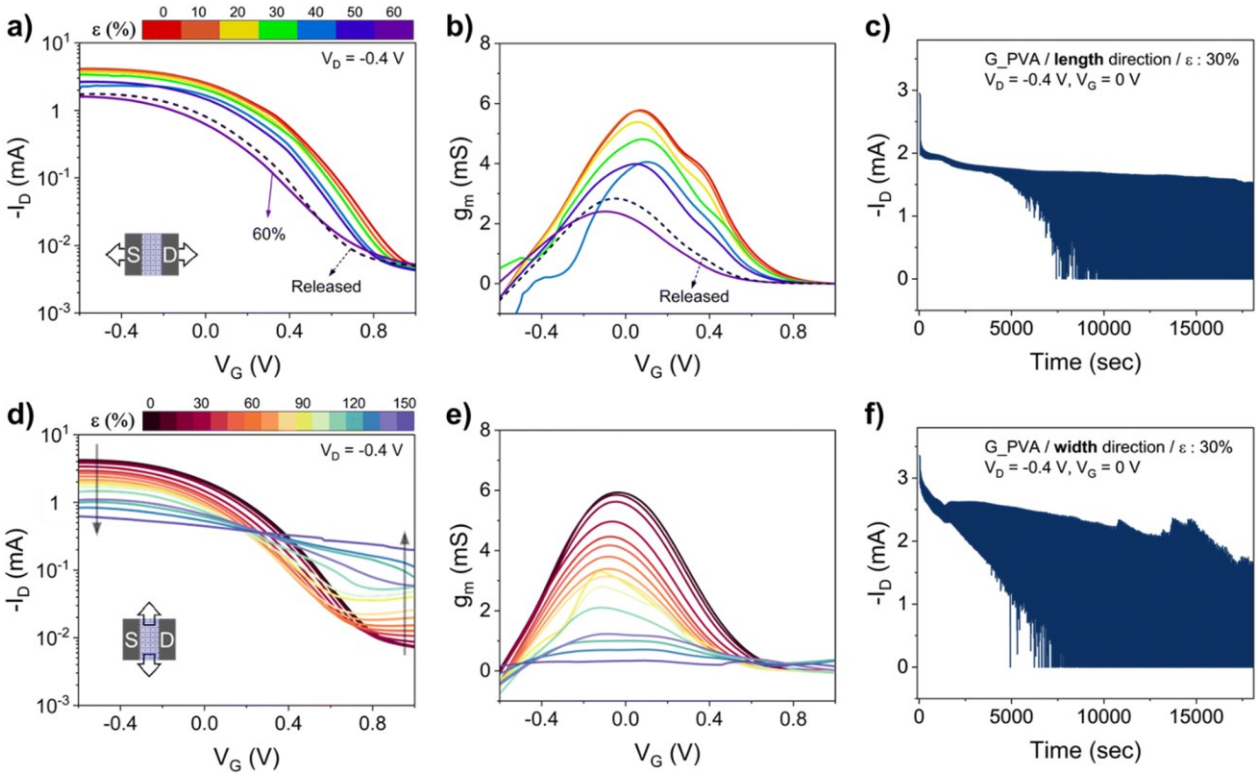

Figure 3.4 Electromechanical test of G_PVA OECTs (channel $W = L = 8$ mm) under bi-axial tensile strain. (a) Transfer curves under strain in a length direction of the active channel. The transfer curves share the color bar with g_m. The transfer curves were obtained with 10% strain increment between measurement. Dashed line represents the transfer curve when released from 70% strain (channel of the device was broken). (b) g_m was calculated from (a). (c) Drain current was measured with 0 V gate bias while repeatedly stretching by 30% for 1000 cycles in length direction. (d) Transfer curves under strain in a width direction of the channel. (e) g_m was extracted from (d). (f) Drain current was measured with 0 V gate potential while multiply stretching by 30% for 1000 cycles in width direction.

Our group previously reported stretchable OECTs obtained via several strategies. Devices with stretchability as high as 30% were achieved via the pre-stretched method.[156] Strain-insensitive OECTs up to 30% strain were achieved by controlling the thickness and baking temperature of the active channel.[170] Introduction of polyethylene glycol to channel enhanced the stretchability of the OECTs to 45% strain.[171] Fabrication of sub-micro fibrous structure of the channel by

electrospinning resulted in the stretchable devices as 50% strain.[172] In this work, we further improved the stretchability of OECTs up to 60%.

These values are in line with findings of other research groups. OECTs on the biomimicking-buckled substrate achieved omnidirectional stretchability up to 30%.[132] OECTs fabricated by combining the pre-stretching method and engineering the topography of the substrate showed 30% stretchability.[158] OECT arrays on a honeycomb grid substrate stably performed under 15% tensile strain.[131] Integration of 100% pre-stretching and honeycomb structure of the channel exhibited the high stretchability of the OECTs up to 100%.[157] Anther OECT also achieved stability in 100% tensile strain using a 3D-microstructured channel, serpentine organic material interconnects, and an additive for the active channel.[102]

Multiple-cycle stretchability tests were performed at a 30% cyclic strain (Figure 3.4c and f). A drop in the drain current was observed after a few initial strain cycles, and the current slightly decreased until approximately 7000 s in the length direction and approximately 5000 s in the width direction. The initial changes in the drain current are consistent with the resistance change of stretched PEDOT:PSS films in our previous work.[155] The sudden current changes after 5000 s, are likely related to the stretchable Ag interconnects. According to the magnified plot of the multiple-cycle stretchability tests (Figure A.11), the current spiked every time the OECTs were stretched and released. In our previous work, a similar test at 30% cyclic strain was conducted with PEDOT:PSS films printed on the TPU substrate without the Ag electrodes and no spikes were observed. [155] The spikes might be alleviated by patterning serpentine interconnects and replacing the Ag with conducting polymer interconnects.[102]

We summarized the main device parameters of some examples of all-printed OECTs found in the literature along with our results in Table 3.2. Most of these studies utilized PEDOT:PSS as the channel material, likely due to its commercial availability in various formulations, which accommodates the requirements for different printing techniques. Compared to other all-printed OECTs, our devices with printed hydrogel electrolytes not only show performances within the comparable range but also exhibit stability in the long term and perform under high tensile deformation.

3.5 Conclusions

We have successfully fabricated long-term stable and stretchable all-printed OECTs using direct-ink write technology. The devices gated with the hydrogel containing glycerol remained functional for 50 days without significant performance deterioration and showed continuous operation for about 7 hours. The results of OECTs operation under strain (60% in length direction and 110% in width direction) indicate that the devices can withstand the mechanical deformation strain required for wearable and on-skin electronics. The device performance under mechanical deformation can be further improved by introducing additives to enhance the stretchability of the channel and contact materials. In addition to the advantages in long-term operation and stretchability, the device performance of G_PVA OECTs is comparable to other all-printed OECTs. Therefore, we expect the all-printing method for fully stretchable OECTs with printable hydrogel electrolytes will contribute to the development of all-printed wearable bioelectronics.

CHAPTER 4 ARTICLE 2: RECYCLABLE PRINTED LIQUID METAL COMPOSITE FOR UNDERWATER STRETCHABLE ELECTRONICS

Chi-hyeong Kim, Jinsil Kim, Jiaxin Fan, Meijing Wang, Fabio Cicoira

Department of Chemical Engineering, Polytechnique Montréal, Montréal,

Québec H3C 3A7, Canada

* Corresponding author: fabio.cicoira@polymtl.ca

Small Science, Received: November 2, 2024, Published online: March 31, 2025

4.1 Abstract

Multifunctional stretchable conductors are crucial components in fully stretchable circuits for wearable bioelectronics. Conductive composites made from liquid metal (LM) fillers and polymer matrices have garnered significant interest due to their high electrical conductivity, adjustable mechanical properties, biocompatibility, and recyclability. Herein, a printable LM composite is developed using a custom-designed block copolymer to ensure electromechanical stability in both wet and dry conditions. The LM composite demonstrates high conductivity (around 10^5 S m^{-1}), stretchability up to 500%, and maintains stable resistance with cyclic strain ranging from 0 to 50% for over 16 h, in both ambient and aqueous environments. Furthermore, bulk LM is successfully recovered from printed composites using green solvents, supporting the composite's recyclability.

4.2 Introduction

Soft wearable electronics are in high demand for various applications, including electronic skin and wearable healthcare monitoring systems.[173-178] For these applications, devices based on stretchable conductors are desirable due to their ability to conform closely to the surface of biological tissues.[34, 35] To ensure the stability and durability of wearable electronic devices, these conductors must retain consistent conductivity when subjected to repeated deformation and exposure to aqueous environments, such as rainwater or sweat.

Significant effort has been dedicated to developing multifunctional stretchable conductors to meet the key requirements of wearable electronics. Conducting polymers, often mixed with additives to enhance electrical conductivity (0.1–1000 S cm^{-1}),[128, 179] stretchability,[180] recyclability,[112] and self-healing properties,[181] have been employed

as active components in stretchable devices, such as sensing electrodes and transistor channels. Additionally, they have been explored for interfaces with biological tissues, exhibiting biocompatibility and electrical stability in aqueous environments.[119, 182] Conducting composites, which incorporate electrically conductive fillers (e.g., metal nanoparticles[35, 183] and carbon-based materials[112]) within a polymer matrix, have been investigated as electrodes and interconnects in flexible and stretchable electronics, achieving high electrical conductivity (1000–70 000 S cm^{-1}).[179] However, these composites may exhibit electrical instability under repeated mechanical deformation.[68, 69] The electromechanical properties of stretchable conductors can be improved using fillers based on gallium-based liquid metals (LMs), such as eutectic gallium indium (EGaIn) and gallium indium tin alloy (galistan). These materials have low melting points (below room temperature), high conductivity (≈10^6 S m^{-1}), and are biocompatible.[184] Given that gallium and indium are critical materials, considerable attention has been directed toward their recycling.[70, 71, 177, 185]

LM composites are typically formed by breaking down bulk LM into micro- or nanodroplets, which are dispersed in a fluid, such as uncured polydimethylsiloxane (PDMS) or a liquid polymer solution, through vigorous rotary (shear) mixing[82] or sonication.[83, 186] These suspensions can be used as inks for various patterning techniques, such as stencil printing,[84] spray coating,[85] and direct ink writing.[83] However, immediately after processing, the composites exhibit insulating behavior or low conductivity due to the presence of the insulating shell of gallium oxide (Ga_2O_3) and the polymer matrix.[62] Activation processes, such as mechanical compression or extension,[71, 89, 187, 188] laser sintering,[85] or acid treatment,[83] are typically used to break the oxide layer and the polymer matrix, forming electrically conductive pathways within LM composites.[189]

Silicone-based elastomers such as PDMS and Ecoflex are commonly used as matrices for LM composites in wearable electronics due to their high stretchability, chemical inertness, and biocompatibility.[86, 87, 190] Recently, a silicone-based water-resistant LM composite with long-term stability underwater was reported.[88] However, the limited solubility of PDMS complicates LM recycling. To improve the dispersion in polymer solutions, the LM droplets can be functionalized with polymer ligands through interactions between surface oxides and functional groups, such as hydroxyls.[186, 191, 192] High-resolution printing (≈50 μm linewidth) of poly(styrene sulfonate)-grafted LM composites using meniscus-guided direct writing has yielded

materials with high conductivity (1.5×10^6 S m^{-1}) and stable electromechanical properties, with resistance increasing by only 8 at 200% strain and 40 at 500% strain.[83] A composite of poly(vinyl alcohol) (PVA) and LM has been used to develop a highly conductive (1.3×10^5 S m^{-1}) 3D printing ink compatible with various substrates,[89] which has enabled applications in alarm systems, object locators, and highly sensitive wearable pressure and motion sensors. The LM could be recycled through alkaline treatment and reused for ink preparation. While LM composites with excellent electromechanical performance, improved sustainability, and good printability have been developed, further research is needed to achieve multifunctional LM composites that are compatible with various substrates and deposition techniques, offering electrical and mechanical stability, water resistance, and end-of-life material recovery.

In this study, we report a printable LM composite based on EGaIn and a custom-designed block copolymer, poly(acrylic acid)-*b*-poly(styrene-*ran*-butyl acrylate) (PASTA). The combination of PASTA with LM provided suspension stability and enabled the printing on stretchable thermoplastic polyurethane (TPU). After activation, achieved through acetic acid exposure and mechanical stretching, the PASTA-grafted EGaIn (LM/PASTA) composite exhibited high conductivity (in the 10^5 S m^{-1} range), high stretchability (500%), and stable electromechanical performance with minimal variations under cyclic strain in dry and wet conditions. The successful demonstration of a wearable strain sensor with nearly identical performance in air and underwater highlights the potential of our LM/PASTA composite for practical applications. Furthermore, we successfully recycled LM from the printed LM/PASTA electrodes using green solvents. Our recyclable and electromechanically durable materials offer promising contributions to the advancement of emerging soft wearable electronics

4.3 Results and Discussion

4.3.1 Synthesis of a Custom-Designed PASTA

We designed and synthesized a novel block copolymer, PASTA (Figure 4.1), to develop a multifunctional LM composite with high electrical conductivity and electromechanical stability, suitable for direct ink printing (refer to Experimental Section for details).

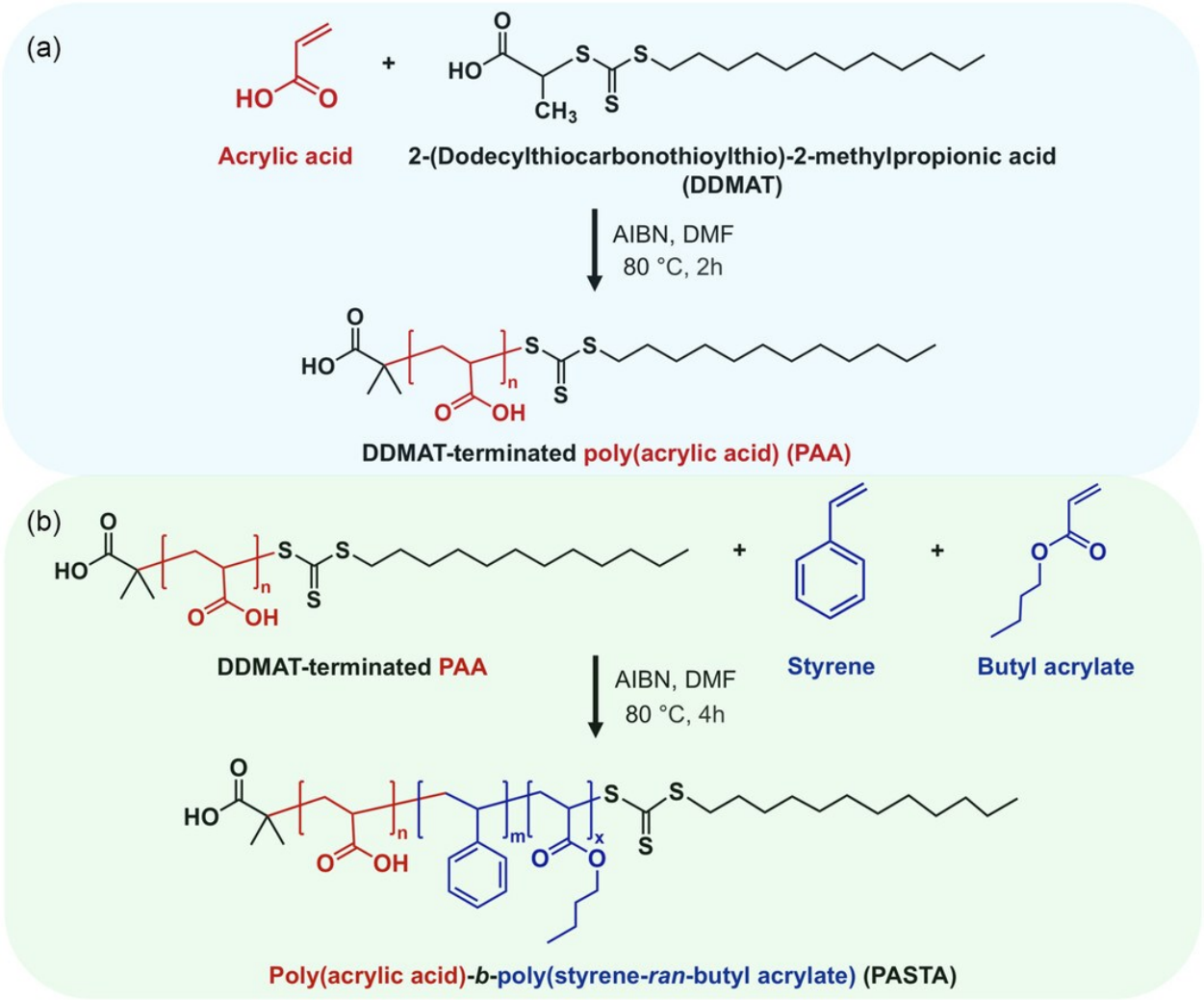

Figure 4.1 Scheme of polymer synthesis. a) DDMAT-terminated PAA was synthesized by RAFT, and b) PASTA was synthesized by random polymerization from a DDMAT-terminated PAA chain (refer to Experimental Section for details).

Anchoring groups for metal oxides are typically hydrophilic (e.g., carboxylate or alcohol).[191] Consequently, LM composites based on homopolymers containing such groups, like poly(acrylic acid) (PAA) or PVA, tend to be hydrophilic and, in some cases, water-soluble. To prevent dissolution and enhance water resistance, we designed a block heteropolymer in which the anchoring carboxylic groups are attached to a minor PAA block, while the major poly(styrene-ran-butyl acrylate) block is hydrophobic.

The synthesis was carried out through reversible addition–fragmentation chain transfer (RAFT) polymerization, followed by random free-radical polymerization. In the first step, using a chain transfer agent (DDMAT), we synthesized DDMAT-terminated PAA (Figure 4.1a), which serves as an anchoring block to the surface of the LM droplets by bonding carboxyl groups to the native gallium oxide,[191] enabling the formation of a stable LM suspension suitable for printing. Next, a poly (styrene-ran-butyl acrylate) block was grown from DDMAT-terminated PAA (Figure 4.1b). Butyl acrylate was chosen to impart softness and elasticity to the polymer, due to the relatively high mobility of its butyl ester side chain,[193] while styrene was incorporated to enhance mechanical strength, owing to its aromatic ring structure.[194] Preliminary tests indicated that an optimized ratio of monomers in the poly(styrene-ran-butyl acrylate) block yielded a polymer with both stretchability and strength. ^{1}H-NMR and gel permeation chromatography (GPC) confirmed the successful synthesis of PASTA through well-controlled polymerization (Figure B.1 and B.2, Supporting Information). Mechanical characterization (Figure B.3, Supporting Information) via stress–strain testing and differential scanning calorimetry (DSC) (Figure B.4, Supporting Information) demonstrated the high stretchability of PASTA (≈1000%).

4.3.2 LM Ink Preparation and Printing LM/PASTA

To prepare the LM suspension ink, EGaIn was added to a PASTA solution in toluene and broken down into microscale droplets via tip sonication (Figure 4.2a). Composites were prepared using different LM-to-PASTA ratios, with the materials produced with 15, 35, and 70 mg PASTA in the solution designated as P15, P35, and P70, respectively (refer to Section **4** for details). The dissolved PASTA grafted onto the droplets via PAA blocks, forming a polymer brush architecture (Figure 4.2b) that led to the formation of a stable suspension.[195, 196] The stability of the LM/PASTA suspension was maintained over time (Figure 4.2c,d and Figure B.5, Supporting Information), making it suitable for printing.[83]

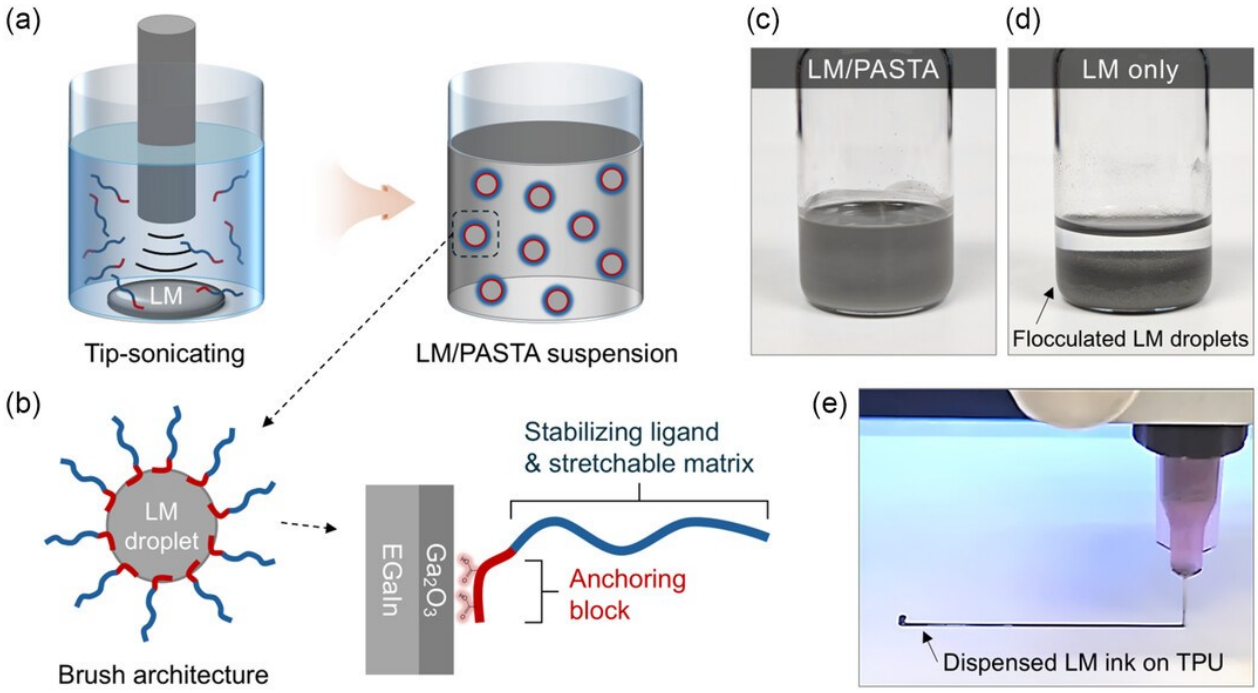

Figure 4.2 a) Schematics of a LM/PASTA suspension prepared by tip sonication in toluene and b) a PASTA-grafted LM droplet with polymer brush architecture. Digital photograph of c) LM/PASTA ink and d) control LM ink without the polymer. e) Digital photograph of the printed LM/PASTA ink on TPU.

4.3.3 Microstructure and Activation of LM/PASTA

Printing on a TPU substrate (Figure 4.2e; see Experimental Section for details) resulted in the formation of an LM composite (P35, thickness ≈14.4 µm, Figure B.6, refer to Supporting Information for details) consisting of nearly circular droplets with an average size of ≈1.2 µm (Figure 4.3a). Initially, the composites exhibited insulating behavior because of the presence of the gallium oxide layer and the polymer matrix surrounding the droplets, making activation necessary to enhance electrical conductivity.[197] To gain insight into the activation process, we first investigated the effect of chemical and mechanical treatment individually, followed by a combined approach. Chemical treatment was performed by exposing the composite to a solution of 10 vol% acetic acid in acetone. Acetone was chosen as the solvent because it partially dissolves PASTA before evaporation, facilitating the penetration of the acid through the composite. Scanning electron microscopy (SEM) images reveal that after chemical treatment the spacing between the LM

droplets increased (Figure 4.3b and Figure B.7, Supporting Information). The energy-dispersive X-ray spectroscopy (EDX) maps of gallium and carbon (Figure 4.3c-e) strikingly reveal a

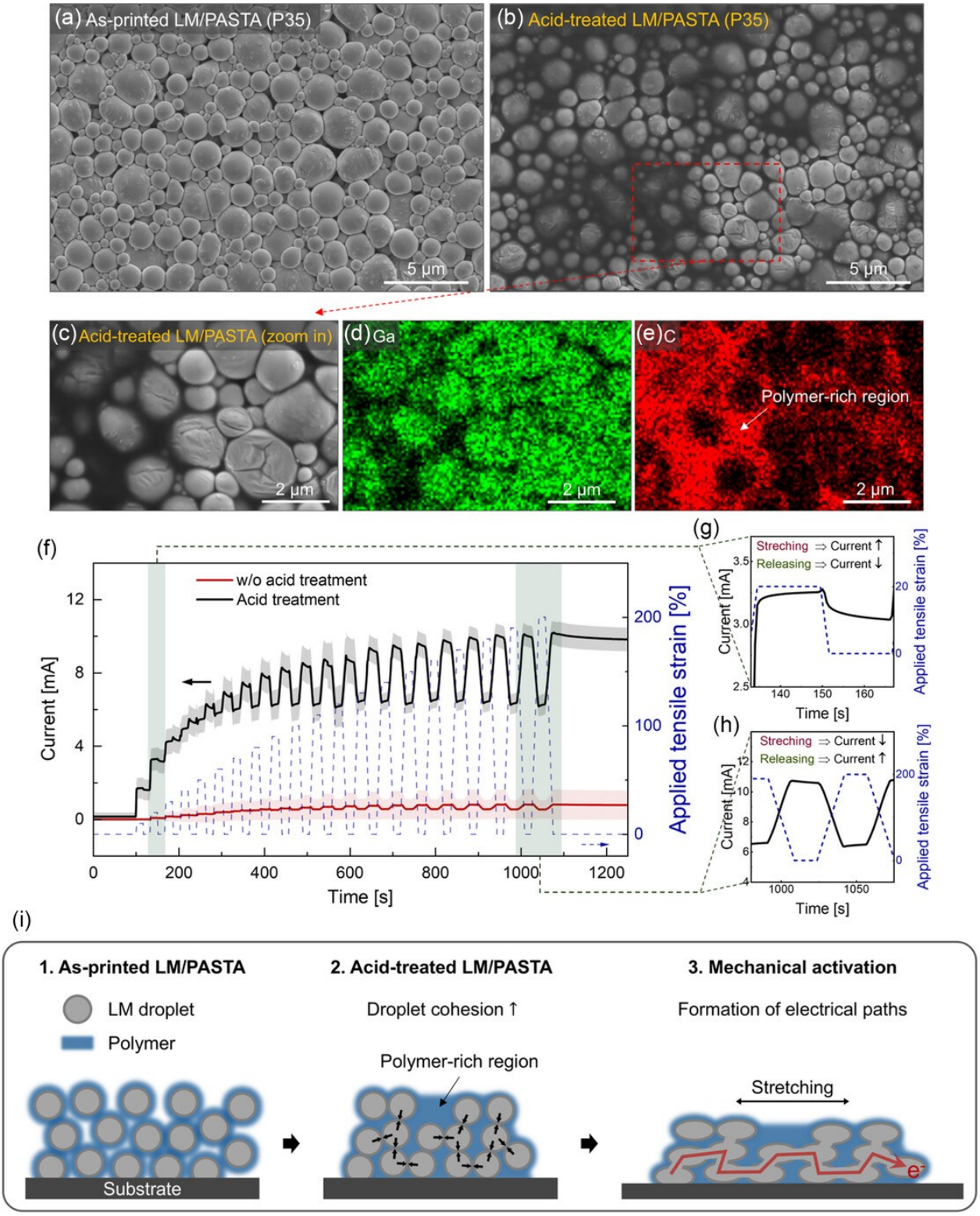

significantly higher carbon content in the gaps between the LM droplets, highlighting these areas as polymer-rich regions.

Figure 4.3 SEM images of a) as-printed and b) acid-treated LM/PASTA composites (P35) on TPU. c) Magnified SEM image to highlight the EDX mapping of d) Ga (green) and e) C (red). f) Average current versus time plot showing the currents of the LM (P35) composites during mechanical activation alone (red curve) and combined chemical and mechanical activation (black curve). A constant voltage of 30 mV was applied. The shaded area around the curves represents the standard deviation extracted from three (mechanical treatment) and five (combined treatment) samples. The dashed blue line (right axis) represents the applied strain, which was increased in 10% increments from 0 to 200% (right axis). Magnified plots of current change at g) 20% strain and h) 200% strain in the stepwise mechanical activation process. i) Scheme of the acid treatment and mechanical activation processes of the LM composite.

This suggests that acetic acid may partially remove the surface gallium oxide, to which PASTA is anchored, causing the polymer to detach and occupy the space between the droplets, leading to morphological changes. This acid treatment also led to optical color alterations in the composite (Figure B.8, Supporting Information), a phenomenon similar to the one previously reported for DMSO-treated LM composites.[198] The chemical reactions involved in this process are explained in a later section.

However, following this treatment, the composites remained insulating, indicating that exposure to acetic acid solution alone was insufficient to establish electrical pathways between the LM droplets. To increase the conductivity, we investigated the effect of mechanical treatment (red curve, Figure 4.3f) by applying stepwise uniaxial tensile strain (0–200%) and then combined this with chemical treatment (black curve, Figure 4.3f). The composite activated by stretching alone (red curve) exhibited a current increase from the noise level (10^{-8}–10^{-7} mA, Figure B.9, Supporting Information) to ≈1 mA after activation at 10–50% strain, with poor sample-to-sample reproducibility (Figure B.9, Supporting Information). The average conductivity of the activated samples was $\approx 2.0 \times 10^4$ S m^{-1}.

The combined treatment, consisting of acetic acid treatment followed by mechanical activation, was more effective to increase electrical conductivity (Figure 4.3f, black curve).

The highest current observed in the activated samples was in the 10 mA range, corresponding to an average conductivity of $\approx 3 \times 10^5$ S m^{-1}, which is one order of magnitude higher than that obtained by mechanical activation alone. The current showed a steep increase upon applying strains in the 10–50% range, followed by a gradual increase up to 200% strain, indicating that the LM composite was nearly fully activated at ≈50% strain. Treatment with acetone followed by mechanical activation resulted in a conductivity similar to that obtained after mechanical activation alone (Figure B.11, Supporting Information), confirming that acetic acid is responsible for chemical activation.

Interestingly, different electromechanical coupling behaviors were observed across various activation strain ranges. In the 10–30% strain range (Figure 4.3g), the composites exhibited a higher current when stretched than when released, even under repeated 20% strain for 1000 cycles (Figure B.10, Supporting Information), as already observed for a few other LM composites.[199] For applied strains beyond 40%, the current in the stretched state was lower than in the released state (Figure 4.3h), a behavior commonly observed in stretchable conducting composites.[35, 83, 84, 112] Activation by acid treated and 50% strain was performed to achieve a common electromechanical coupling behavior (current in the stretched state lower than in the released state).

Based on the above results, we illustrated the activation process with a schematic (Figure 4.3i). Initially, the composites are insulating due to the gallium oxide and polymer layer surrounding the droplets. Upon acid treatment, the grafted polymer is removed from the droplets and diffuses toward the surface of the composite, forming a polymer-rich region. This migration of polymer chains likely reduces the thickness of the insulating barrier around the LM droplets and enhances droplet cohesion. Finally, tensile activation physically ruptures the insulating gallium oxide, allowing LM leakage that forms conductive pathways within the polymer matrix. Acid treatment likely facilitates the formation of these conductive paths during mechanical activation. Thus, the combination of acid treatment and mechanical strain successfully activated the LM/PASTA, resulting in high conductivity.

To optimize the polymer content, we compared materials prepared with different PASTA contents (P15, P35, and P70, Table B.1 and Figure B.12, Supporting Information). P15 exhibited conductivity similar to that of P35 but with poor reproducibility and nonuniform droplet sizes. In

contrast, P70 exhibited a conductivity approximately one order of magnitude lower, likely due to an excess of insulating polymer between the LM droplets. Consequently, P35 composites were used for the remainder of this study, as they provided high conductivity and a uniform morphology.

4.3.4 Electromechanical Characteristics in Dry and Wet States

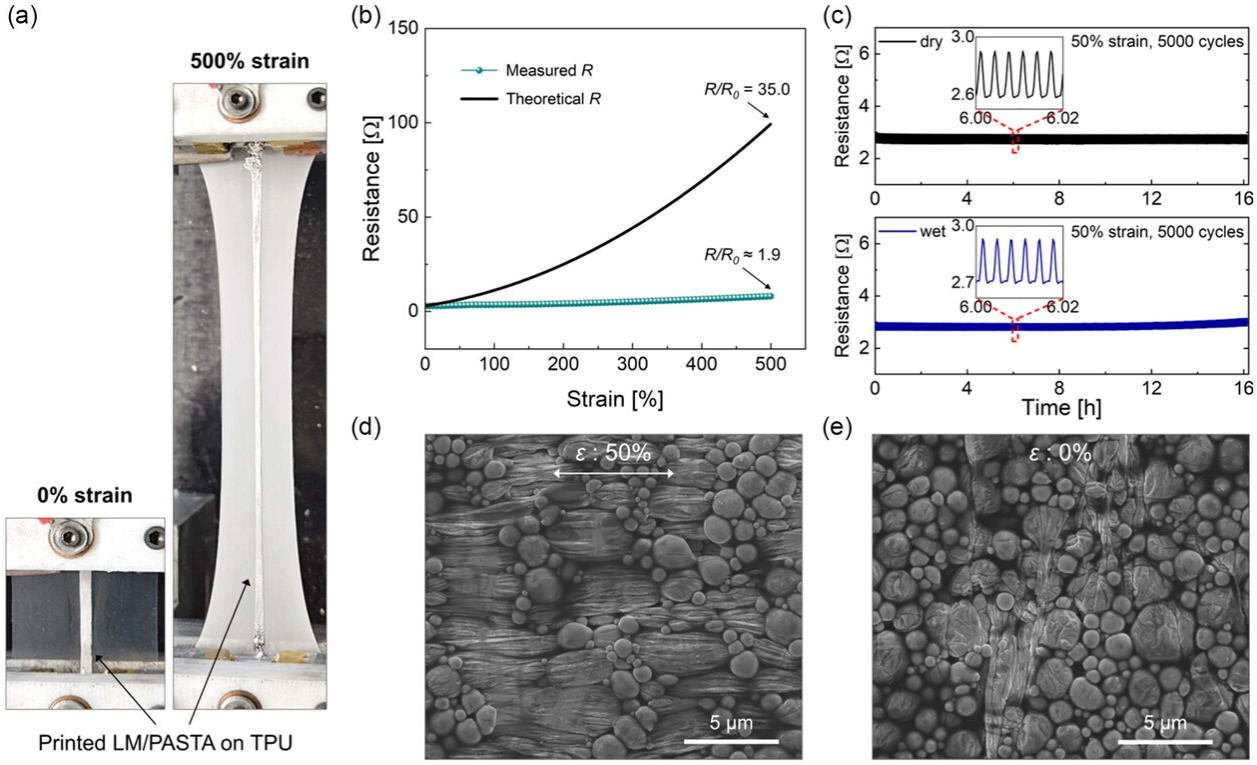

Figure 4.4 a) Digital photograph of a LM/PASTA composite ($2 \times 25\ mm^2$) printed on thermoplastic polyurethane (TPU) at 0% and 500% strains. b) Measured and theoretical resistances versus strain of the printed LM composite. The sample was stretched at a speed of $2\ mm\ s^{-1}$. c) Resistance versus time of LM/PASTA (P35) over 5000 cycles of 50% strain conducted over 16 h under dry and wet conditions. The insets show the magnified plots (6.00–6.02 h). For the wet conditions test, the LM composite was wet with water supplied by a syringe pump (Figure B.13, Supporting Information). SEM images of d) a uniaxially stretched (50%) sample and e) a released (0%) sample used in the durability test.

To further investigate the electromechanical properties, we conducted electromechanical characterization of the composites activated by stretching them 20 times to 50% tensile strain. The composites were subjected to a continuous tensile strain of up to 500% (Figure 4.4a), and the change in the resistance was monitored (Figure 4.4b). The samples with an initial resistance of

≈3 Ω at 0% strain exhibited a resistance increase of ≈5% at 30% strain, ≈20% at 100% strain, and ≈40% at 200% strain. The change in the measured resistance is much smaller than that of the theoretical value, which can be expressed with the equation (see Note, Supporting Information for details) below.[84]

$$R(t) = R_0\big(1 + \varepsilon(t)\big)^2 \tag{4.1}$$

where $R(t)$ is the theoretical resistance at a given time (t), which was derived from a typical resistance equation for materials with constant conductivity and volume. R_0 is the resistance of the unstretched LM composite, and $\varepsilon(t)$ is the applied strain at the time t. Based on Equation (**1**), the theoretical resistance of LM/PASTA is expected to increase to ≈100 Ω (3500%) at 500% strain; however, a resistance increase of only ≈8 Ω (≈185%) was observed (Figure 4.4b).

The electromechanical durability test was performed by applying repeated tensile strain (loading–unloading) while monitoring the resistance change (Figure 4.4c), under both dry and wet conditions. Under both conditions, the composites showed stable performance over 5000 cycles of 50% strain conducted over 16 h (additional results are available in Figure B.14, Supporting Information) and remained stable even after the same number of cycles of 100% strain (Figure B.15, Supporting Information). The stretchable PASTA matrix effectively prevented significant cracking and delamination of the composite from the substrate during the mechanical deformation. Moreover, the stability under wet conditions can be attributed to the hydrophobic blocks of PASTA, which protect the polymer matrix from swelling and weakening in water.

To gain insight into the electromechanical behavior of the composite, we examined the morphology of a stretched (50% strain) and a released sample after the durability test (5000 cycles). Overall, SEM images showed that the durability test did not induce major morphological changes, such as cracks or droplet ruptures, which align with the observed electromechanical stability. Upon stretching (Figure 4.4d), relatively large droplets on the surface of the composite were elongated in the direction of the applied tensile strain while small droplets remained spherical shapes. In the released state (Figure 4.4e), most large droplets returned to nearly circular shapes and showed wrinkles due to stretching.

Overall, the materials reported here exhibited stretchability and electrical performance comparable to previously reported LM composites (Table B.2, Supporting Information), while demonstrating

exceptional electromechanical durability in water, an area still largely unexplored. These characteristics make these composites ideal materials for electrodes and interconnects in wearable electronics, especially when exposed to aqueous environments such as sweat or rain.

4.3.5 Strain Sensor Based on Printed LM Composite

As a proof of principle, we fabricated a strain sensor by printing the LM/PASTA composite on a stretchable TPU substrate. LM composite-based strain sensors working in the dry state were previously reported.[89, 188, 200] To evaluate the suitability of the LM composite for use in aqueous environments, we performed measurements in water after attaching the sensor to the wrist of a volunteer using Tegaderm tape (Figure 4.5a). The wrist wearing the sensor was repeatedly bent and released in the air and underwater (Figure 4.5b). The resistance change ($\Delta R/R_0$) during wrist bending under dry and wet conditions exhibited a similar behavior (Figure 4.5c). Additionally, the resistance change in both conditions was close to 2%, indicating that the LM/PASTA-based strain sensor performs equally well in air and water. This demonstrated the potential of the LM composite as a wearable strain sensor in various underwater applications, including swimming, scuba diving, or rehabilitation in water for monitoring body motions.

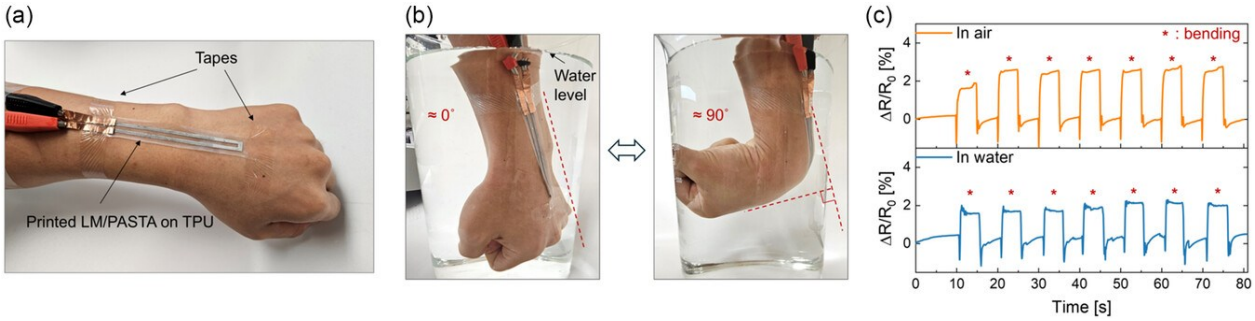

Figure 4.5 a) Digital photograph of printed LM composite-based sensor on TPU, fixed on the wrist of a volunteer using Tegaderm tape. b) Wrist with strain sensor repeatedly bent around underwater. c) Resistance change versus time upon multiple bending of the sensor in air and underwater.

4.3.6 Recycling of the Liquid Metal

Recyclable components and eco-friendly chemicals are key to sustainable electronics. EGaIn, an alloy of two critical materials, is highly recommended for recycling. Extraction of EGaIn from LM-based electronics has been achieved using hydrochloric acid and sodium hydroxide.[83, 89,

185] Here, we performed LM recycling using acetone and acetic acid, both of which are classified as green solvents.[201] The printed LM composite on TPU was dissolved in acetone (Figure 4.6a). Since PASTA is soluble in acetone (Table B.3, Supporting Information), PASTA-grafted LM droplets were redispersed in acetone after the removal of the TPU substrate (Figure 4.6b). The LM collected by centrifugation maintained its droplet state, as the surface oxides prevented the droplets from merging (Figure 4.6c). After adding acetic acid and applying moderate heat, the droplets merged into reusable bulk LM (Figure 4.6d). During this step, the following chemical reaction likely occurred on the surface of LM droplets[202]

$$6CH_3COOH\ (l) + Ga_2O_3\ (s) \rightarrow 2Ga(CH_3COO)_3\ (aq) + 3H_2O\ (l) \qquad (4.2)$$

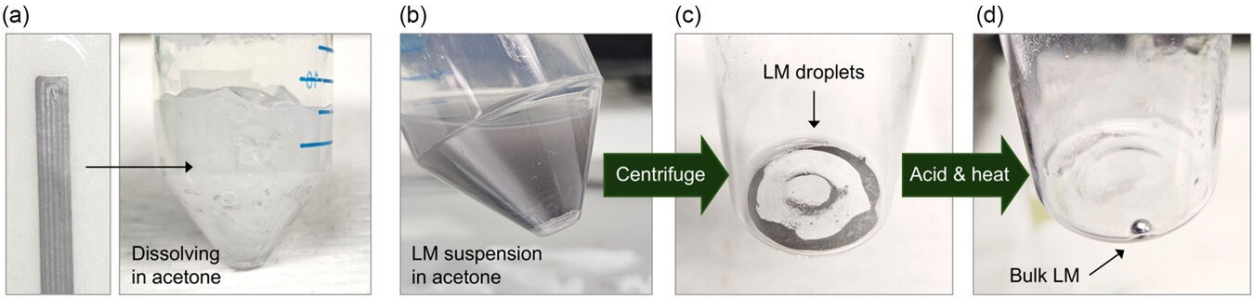

Figure 4.6 LM recycling process. a) LM/PASTA composite printed on TPU soaked in acetone. b) LM suspension in acetone after removal of the insoluble TPU. c) LM droplets collected after centrifugation. The droplets were separated by native oxide on their surface. d) Bulk LM after adding acetic acid and heating.

Upon contact with acetic acid, gallium acetate ($Ga(CH_3COO)_3$) formed on the surface of the LM droplets, replacing the gallium oxide layer. We hypothesize that the gallium acetate on the droplet surface is dissolved by the acetic acid, allowing the pure EGaIn droplets to merge into bulk LM before additional gallium oxide could form. Given that the gallium oxide layer is typically 0.5–5 nm thick,[203] the loss of gallium compounds during recycling is negligible. The yield of recycled LM was ≈95%. This demonstrates that the EGaIn in the LM/PASTA composite can be effectively recycled using a simple extraction process with green solvents. Furthermore, compared

to other polymer matrices, PASTA facilitates LM recycling, contributing to a sustainable LM composite with high performance (Table B.2, Supporting Information).

4.4 Conclusion

In this study, we developed a highly conductive and stretchable printable LM composite with a minimal resistance change under mechanical strain and exceptional stability under cyclic mechanical strain in both dry and wet environments. The composite incorporates a specifically designed block copolymer as the polymer matrix, featuring a polyacrylic acid functional block to interact with LM droplets ensuring suspension stability, and a poly(styrene-*ran*-butyl acrylate) block to provide softness, stretchability, and hydrophobicity. The resulting material met the key requirements for a stretchable conductor: metallic conductivity (in the 10^5 S m^{-1} range), high stretchability (≈500%), and minimal resistance change upon strain (≈5% at 30% strain). The LM composite exhibited exceptional durability with negligible degradation in electrical performance for 16 h of cyclic strain at 50% in both dry and wet conditions, which made possible its use in underwater strain sensors. In addition to its impressive performance, the composite can be easily dissolved in green organic solvents to recover valuable LM, promoting the recycling of critical materials.

4.5 Experimental Section

4.5.1 Materials

Azobisisobutyronitrile (AIBN, Millipore Sigma) was purified by recrystallization from ethanol and dried in a vacuum oven at 50 °C for ≈16 h. EGaIn (Ga 75.5%/In 24.5%, ≥99.99%), 2-(dodecylthiocarbonothioylthiododecylthiocarbonothioylthio)-2-methylpropionic acid (DDMAT) (98%), acrylic acid (99%), n-hexane (≥95%), diethyl ether (≥99%), tetrahydrofuran (THF) (≥99.5%), cyclohexane (≥99%), and 1-Octanol (≥99%) were purchased from Millipore Sigma and used as received. *N*,*N*-dimethylformamide (DMF) (99.8%), butyl acrylate (>99%), styrene (99%), toluene (99.8%), acetic acid (99.7%), acetone (99.5%), and anisole (99%) were purchased from Thermo Fisher Scientific. Thermoplastic polyurethane (TPU) on removable silicone paper (Elecrom Stretch White, thickness 80 μm) was purchased from Policrom Screens (Italy).

4.5.2 Polymer Synthesis

The synthesis of the polymer PASTA consisted of two steps: 1) synthesis of DDMAT-terminated poly (acrylic acid) (PAA) via RAFT polymerization (Figure 4.1a) and 2) free radical random polymerization of PASTA using the synthesized DDMAT-terminated PAA and monomers (styrene and butyl acrylate) (Figure 4.1b). Both RAFT and random polymerization were conducted following previously reported procedures.[204, 205] The ratios of reagents in all reactions were determined based on the reaction stoichiometry. Through preliminary tests of different monomer ratios, we selected the one in which the polymer exhibited rubber-like mechanical properties, assessed by manual stretching.

To synthesize DDMAT-terminated PAA, AIBN (23 mg, 0.14 mmol), as the initiator, and DDMAT (50 mg, 0.14 mmol), as the chain transfer agent, was introduced into a round-bottom flask, which was sealed with a rubber septum and purged with N_2 gas for 10 min. DMF (3.63 g, 3.85 mL) was added, and the mixture was stirred for 5 min at room temperature. Acrylic acid (1.48 g, 0.02 mol) was successively added to the mixture, and then polymerization was conducted at 80 °C for 2 h while stirring with a magnetic stirrer. The reaction was stopped by cooling the flask to room temperature in a water bath. The resulting DDMAT-terminated PAA dissolved in DMF was purified by precipitation in hexane/diethyl ether (1:1 $w\,w^{-1}$) twice, and the precipitate was collected with a filter paper (Whatman quantitative filter paper, 16 μm pore size) using a vacuum pump. The solid DDMAT-terminated PAA was then dried in a vacuum oven (VWR 1400 E) at 50 °C for ≈16 h. This process resulted in a reaction yield of ≈90%, which was determined by comparing the weight differences between the synthesized polymer and monomers used in the reaction.

To synthesize PASTA, AIBN (45 mg, 0.27 mmol) and 50 mg of the synthesized DDMAT-terminated PAA were introduced into a round-bottom flask, which was sealed with a rubber septum and purged with N_2 gas for 10 min, then the DMF (21.30 g, 22.56 mL) solvent was added, and the temperature was increased to 80 °C. Butyl acrylate (10.46 g, 0.82 mol) and styrene (3.64 g, 0.35 mol) were added, and polymerization was carried out at 80 °C for 24 h. PASTA dissolved in DMF was precipitated twice in hexane/diethyl ether (10:1, $w\,w^{-1}$). The precipitate was filtered through filter paper using a vacuum pump. The solid polymer was dried in a vacuum oven at 50 °C for ≈16 h (yield of ≈85%).

4.5.3 Polymer Characterization

The synthesized DDMAT-terminated PAA and PASTA samples were examined in deuterated chloroform using ^{1}H-NMR spectroscopy (Figure B.1, Supporting Information). Spectra were obtained using a Bruker AVANCE II 400 spectrometer operating at 400 MHz to confirm the chemical structures of DDMAT-terminated PAA and PASTA. For GPC sample preparation to determine polymer molecular weight distribution, PASTA was diluted to a concentration of 0.2 wt% in THF. The analysis was performed using a 1260 Infinity GPC system equipped with a WAT044228 Styragel HR 5 E column manufactured by Waters. THF was used as the eluent and was maintained at 30 °C at a flow rate of 1 mL min^{-1}. In this study, we achieved a polydispersity index (PDI) of 2 for free-radical polymerization (Figure B.2, Supporting Information). DSC analysis (Q2000, TA Instruments, USA) was conducted to determine the glass transition temperature (T_g) of the PASTA samples. ≈12 mg of the sample were loaded into a standard aluminum pan and subjected to a constant flow of nitrogen. To ensure the accurate representation of the thermal behavior without thermal history, the samples were initially cooled to −30 °C and then heated to 200 °C at a rate of 10 °C min^{-1}. Subsequently, a second heating cycle was performed from −30 to 200 °C at the same heating rate. The analysis was based on data collected during the second heating cycle. To prepare the samples for tensile tests, 50 wt% PASTA was dissolved in DMF. The solution was drop cast in a Teflon dog-bone mold and dried at 30 °C on a hotplate for 24 h. PASTA dog bone with ≈4.1 mm width, ≈10.3 mm length, and ≈1.2 mm thickness was obtained. The tensile tests were performed using a Mach-1 V500cst MA009 mechanical tester (Biomomentum Inc., Canada) at a stretching speed of 500 mm min^{-1}.

4.5.4 Preparation of LM/PASTA Ink

To study the effects of the polymer content on the composite properties, the LM/PASTA suspensions were prepared by dissolving various amounts of PASTA (15, 35, and 70 mg) in toluene (3 mL) in a 20 mL glass vial and adding EGaIn (1.1 g). These polymer-to-LM ratios were selected in agreement with previous studies of polymer-grafted LM droplets. The mixture was placed in a cooling water bath at room temperature and subjected to tip sonication (450 Sonifier, Branson, 400 W) for 12 min to obtain uniform suspensions. The LM composites containing 15, 35, and 70 mg PASTA were named P15, P35, and P70, respectively. The suspensions were then stored under ambient conditions in sealed glass vials.

4.5.5 Suspension Stability Test

To demonstrate the effect of PASTA as a surface ligand, an LM suspension was prepared with EGaIn (2.2 g) and PASTA (70 mg) in toluene (6 mL) by tip sonication, as previously described. A control LM suspension was prepared using EGaIn (2.2 g) and pure toluene (6 mL). The resulting LM suspensions were observed for 7 days.

PASTA was found to be soluble in DMF, toluene, anisole, acetone, *o*-xylene, and tetrahydrofuran (Table B.3, Supporting Information). However, the composite in DMF flocculated within an hour (Figure B.16, Supporting Information). Polar solvents with high dipole moments, such as DMF, may interfere with the interaction between the oxide layer of the droplets and the carboxyl groups of the polymer ligands,[195] leading to poor suspension stability. Among the other nonpolar solvents tested, toluene was selected for the preparation of the LM suspension because of its relatively low toxicity and chemical compatibility with our printing equipment.

4.5.6 Printing of LM/PASTA Ink

The LM/PASTA composite was printed on thermoplastic polyurethane (TPU) substrates using a direct ink writing printer (Voltera NOVA) with a 30-gauge stainless steel dispensing nozzle (Nordson EFD) attached to a 3 cc syringe. The patterns were designed using the DipTrace software. The printed materials were dried at room temperature because of the high volatility of toluene. The dried samples were treated with a 10 vol% acetic acid solution in acetone by drop casting with a micropipette and then dried at 80 °C for 30 min. The samples were stored under ambient conditions prior to characterization. The TPU substrates with the printed composites were peeled off from the removable silicone paper lining before characterization.

4.5.7 Scanning Electron Microscopy (SEM)

The morphologies of the printed materials were studied using a Quattro Environmental SEM (Thermo Fisher Scientific) at 5 kV. The elemental composition and mapping were obtained using EDX at 5 kV.

4.5.8 Electrical and Electromechanical Characterization

The samples (length = 25 mm, width = 2 mm) were treated with acetic acid solution and mechanically activated with 50% strain 20 times.

The electrical resistance was measured using a four-point probe (Jandel) connected to a source-measure unit (SMU, Agilent A1902). The thickness (d) of the composite was measured using a dynamic white-light interferometer (Fogale Nanotech Photomap 3-D). The conductivities (σ) of the LM composites were calculated as follows.

$$\sigma = \frac{1}{R_s d} \tag{4.3}$$

where R_s denotes the sheet resistance of the sample.

The electromechanical characterization was performed using a uniaxial homemade translational manipulator equipped with (Agilent A1902). The sample underwent varying strains while being subjected to a constant voltage of 30 mV, and the current was recorded to monitor electrical stability. To test the electromechanical properties, the LM composite was stretched to 500% strain at a speed of 2 mm s^{-1}. The electromechanical durability test was performed with 5000 cycles of 50% repeated tensile strain at a speed of 5 mm s^{-1}. To test the durability of the composite in the wet state, water was continuously delivered to the composite surface using a syringe pump at a flow rate of 0.2 mL h^{-1}. The SEM images of two samples used in the dry state durability test were obtained while one was stretched at 50% strain, and another remained without strain.

4.5.9 Strain Sensor

Strain sensors (length = 20 cm, width = 2 mm) were printed on the TPU substrates. The sensors were activated by acid treatment followed by stretching to 50% strain 20 times. For on-body measurements, the sensor was attached to the wrist of a volunteer using Tegaderm tape, and an electrical connection to the SMU was established using copper tape with alligator clamps. The change in current with wrist bending was recorded under a constant applied voltage of 0.03 V. To validate the sensor performance underwater, the same measurement was conducted while the volunteer's hand was immersed in water in a 4 L beaker. Informed written consent was obtained from the volunteer for the test. The protocol for human experiments was approved by the ethical committee of Polytechnique Montréal (approval number CER- 2021-04-D).

4.5.10 Recycling of EGaIn

For recyclability tests, the printed LM composite on a TPU substrate was soaked in acetone for 30 min. This process dissolved the LM composite, and undissolved TPU was manually removed

from the solution using tweezers. The LM suspension in acetone was centrifuged at 1500 rpm for 15 min to separate the polymer (supernatant) from LM droplets. The supernatant was discarded, and the remaining LM droplets were transferred to a 20 mL glass vial. Finally, concentrated acetic acid (1 mL, 99.7%) was added to the vial, which was heated at 100 °C on a hot plate until the acid was fully evaporated, leaving bulk EGaIn. The recycling yield was calculated by comparing the weights of EGaIn in the printed composite and that of recycled bulk EGaIn.

All data mentioning sample size (*n*) were represented by their mean standard deviation.

CHAPTER 5 ARTICLE 3: IN-PLANE ELECTRICAL ANISOTROPY IN PEDOT:PSS THIN FILMS INDUCED BY WET-STRAIN TREATMENT

Chi-hyeong Kim and Fabio Cicoira

Department of Chemical Engineering, Polytechnique Montréal, Montréal,

Québec H3C 3A7, Canada

* Corresponding author: fabio.cicoira@polymtl.ca

MRS Advances, Submitted: January 26, 2026

5.1 Abstract

Conducting polymers offer attractive opportunities for flexible electronic devices when their electrical properties can be directionally controlled. Here, we report a scalable approach to fabricate in-plane anisotropic poly(3,4-ethylenedioxythiophene):polystyrene sulfonate (PEDOT:PSS) thin films by combining spin coating with wet-strain. The electromechanical coupling behavior of the films was systematically examined in dry and ethylene glycol (EG)-wetted states to identify suitable strain-treatment conditions. While dry films largely followed the resistance changes expected from geometric deformation, EG-wetted films exhibited a pronounced negative electromechanical response at low strain. Analysis of apparent resistivity trends revealed a distinct minimum at approximately 25% strain, suggesting a condition of strain-induced structural reorganization. PEDOT:PSS films treated under these conditions displayed clear in-plane electrical anisotropy, with lower sheet resistance along the strain direction. This wet-strain processing strategy provides a practical route to introduce electrical anisotropy into PEDOT:PSS films, while maintaining compatibility with established device architectures on flexible substrates.

5.2 Introduction

Conducting polymers have attracted significant interest due to their mechanical flexibility, chemical tunability, and low-cost processability [206, 207]. Among them, poly(3,4-ethylenedioxythiophene):polystyrene sulfonate (PEDOT:PSS) s widely used in flexible and bioelectronic devices owing to its mixed ionic–electronic conduction, biocompatibility, and self-healing properties [112, 208-211].

Chain-structure-driven anisotropy is an intrinsic feature of conducting polymers, enabling directional electrical properties without the need for additional materials or matrix blending [123, 212]. Considerable effort has therefore been devoted to developing anisotropic PEDOT:PSS to improve charge transport. In this approach, and device performance. For example, heating-assisted electric-field treatment has been used to induce in-plane conductivity anisotropy in PEDOT:PSS films [213]. In this approach, the application of a high electric field (5 kV cm^{-1}) at elevated temperature for several hours, promotes preferential orientation of PEDOT:PSS domains through interaction between the applied electric field and the polymer dipoles, resulting in anisotropic electrical transport orthogonal to the field direction. Strain engineering has also been successfully employed to produce anisotropic PEDOT:PSS microfibers [121]. When mechanical stress was applied to wet PEDOT:PSS fibers during drying, the polymer crystallites preferentially reoriented along the fiber axis. This alignment of PEDOT chains was verified by wide-angle X-ray diffraction, which revealed that both lamellar ordering and π–π stacking were predominantly oriented perpendicular to the fiber axis. As a result, charge transport was enhanced along the fiber direction, leading to improved hole mobility and enabling high-performance fiber-based OECTs. This strategy was further extended to fabricate free-standing anisotropic PEDOT:PSS sheets for thermoelectric applications [122], using wet-spun microfibers collected onto a spool and consolidated during a flattening process with an additional aqueous PEDOT:PSS dispersion . More recently, brush printing has been demonstrated as a direct route to fabricate anisotropic PEDOT:PSS films without post-treatments [120]. However, the relatively high surfaces roughness associated with this method restricts its applicability to specific device platforms, such as thermoelectric devices.

Most advanced PEDOT:PSS-based devices rely on thin (< 2 μm), smooth, and uniform films typically prepared by spin coating. To fully leverage these established fabrication approaches, further development of anisotropic PEDOT:PSS films that remain compatible with standard device architectures is required.

Here, we report the fabrication of in-plane electrically anisotropic PEDOT:PSS thin films by combining conventional spin coating with a wet-strain post-treatment. The electromechanical coupling behavior of PEDOT:PSS films in dry and wet states was systematically examined to identify the suitable strain-treatment conditions. The resulting wet-stretched films retain the smooth, uniform surfaces characteristic of spin-coated layers, enabling straightforward integration

into existing PEDOT:PSS-based devices on flexible plastic substrates. This approach provides a scalable route to introduce electrical anisotropy into PEDOT:PSS thin films for next-generation electronic and energy applications.

5.3 Experimental Section

5.3.1 Materials

PEDOT:PSS aqueous dispersion (Clevios™ PH1000) was purchased from Heraeus Precious Materials (Germany). EGaIn (Ga 75.5% / In 24.5%, ≥99.99%), dodecyl benzene sulfonic acid (DBSA) (99%), and ethylene glycol (99%) were purchased from Millipore Sigma. Isopropanol (IPA) (99.5%) was purchased from Thermo Fisher Scientific. Polyethylene terephthalate (PET) films (XF-122, 25 μm thickness) were purchased from Polyonics (USA).

5.3.2 PEDOT:PSS film preparation

PET substrates were mounted onto supporting glass plates (7x5 cm^2) and rinsed with IPA. A PEDOT:PSS aqueous dispersion blended with 0.5 v/v% DBSA was spin-coated onto the PET substrate at 800 rpm for 30 s, followed by heating at 120 °C for 30 min (Figure C.1, Supporting information). The PET substrates bearing the spin-coated PEDOT:PSS film were peeled off from the supporting glass plates. To prepare wet PEDOT:PSS films, ethylene glycol (EG) was drop-cast onto the spin-coated films and allowed to infiltrate for 15 min.

5.3.3 Measurement

Electromechanical characterization was performed using a custom-built uniaxial translational manipulator coupled to a source-measure unit (SMU, Keysight A1902). Liquid metal contacts were employed to maintain stable electrical connections between the PEDOT:PSS films and the SMU during stretching (Figure C.2, Supporting information). Electrical resistance was measured using a four-point probe (solid tungsten carbide, 1 mm probe tip spacing, Jandel) connected to the same SMU. Optical microscopy images were acquired using a Carl Zeiss AX10 microscope. The film thickness was measured using a dynamic white-light interferometer (Fogale Nanotech Photomap 3D).

5.4 Results and Discussion

5.4.1 Film thickness–dependent stretchability of PEDOT:PSS

Spin-coating was employed as an established technique to deposit thin, uniform PEDOT:PSS films (Figure 5.1). Rather than using ozone treatment on polyethylene terephthalate (PET) substrates, dodecyl benzenesulfonic acid (DBSA) was blended into the aqueous PEDOT:PSS dispersion to enhance wettability on the hydrophobic PET surface during spin coating [113]. This approach was adopted because PEDOT:PSS films containing DBSA remained well adhered during subsequent wet-stretching in electromechanical characterization, whereas PEDOT:PSS films deposited on ozone-treated PET without DBSA frequently exhibited delamination and fracture.

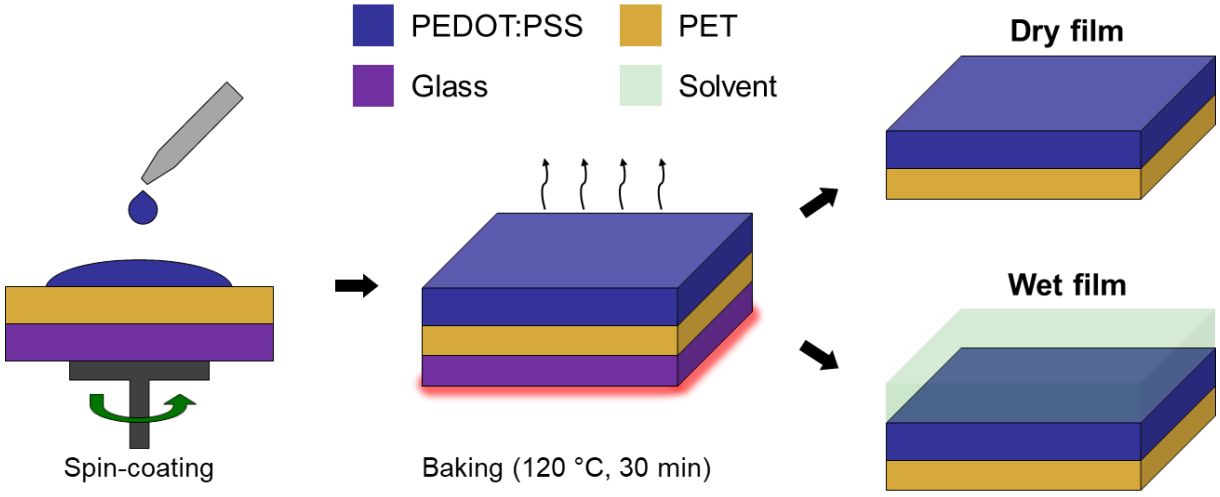

Figure 5.1 Schematic illustration of the preparation process for PEDOT:PSS films in dry and wet states

To investigate the influence of film thickness on strain tolerance, PEDOT:PSS films with varying thicknesses were prepared by varying the number of the spin-coating cycles (one, two, four, and eight). As determined from measurements of four samples for each condition, the thickness of the film prepared by a single spin-coating cycle was 226.95±34.23 nm, while films prepared by two, four, and eight spin-coating cycles exhibited thicknesses of approximately 431.21±40.07, 776.17±51.42, and 1505.80±105.35 nm, respectively. The film thickness increased with the number of spin-coating cycles, showing an approximately linear trend, which is consistent with previous reports [214]. The stretchability of dry (as-prepared) PEDOT:PSS films was first

evaluated by applying an 80% tensile strain. As shown in Figure 5.2, films prepared using one or two spin-coating cycles exhibited no visible damage after stretching. In contrast, films prepared using four or eight spin-coating cycles developed microcracks, with more pronounced cracking observed in the thickest films. Reduced stretchability in thicker PEDOT:PSS films has been reported in previously [215]. On the basis on these results, films prepared by one or two spin-coating cycles were selected for subsequent electromechanical characterization under wet-strain conditions.

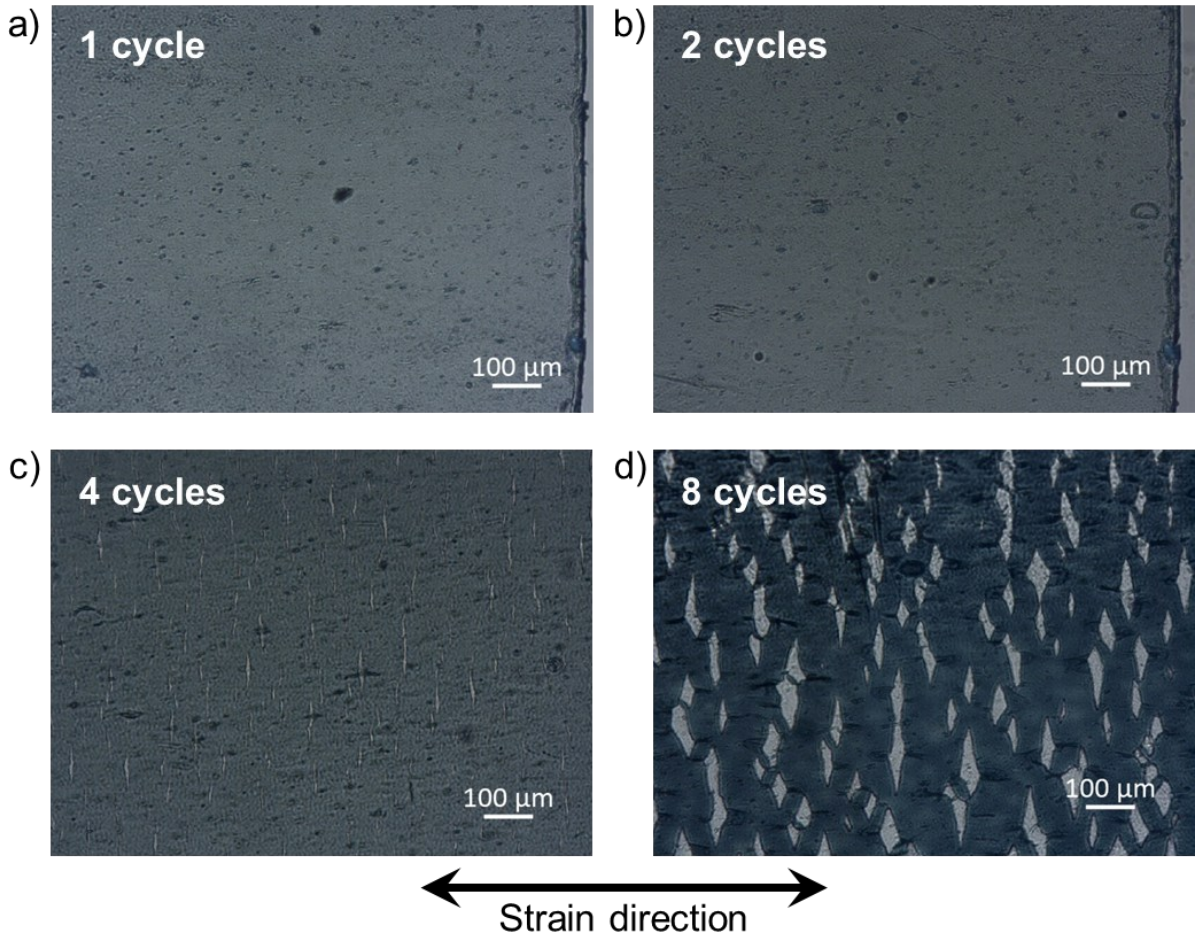

Figure 5.2 Optical microscopy images of dry PEDOT:PSS films after 80% uniaxial tensile strain, prepared by (a) one, (b) two, (c) four, and (d) eight spin-coating cycles

5.4.2 Electromechanical characterization

To identify suitable strain-treatment conditions, the electromechanical coupling behavior of PEDOT:PSS films was systematically investigated. For comparison, the electrical resistance of both dry and ethylene glycol (EG)–wetted PEDOT:PSS films was measured under uniaxial tensile strain (Figure 5.3). EG was used to wet the films, which also resulted in an increase in their electrical conductivity. To assess the influence of deformation rate, tensile strain was applied at different stretching speeds (0.1, 0.3, and 0.5 mm s^{-1}). The experimentally measured resistance was compared with a theoretical prediction accounting solely for geometric deformation, as described by the expression below (see Note in the Supplementary Material for details) [84].

$$R(t) = R_0\big(1 + \varepsilon(t)\big)^2 \tag{5.1}$$

where $R(t)$ is the theoretical resistance at time t, derived from a standard resistance expression under the assumption of constant film volume and conductivity during deformation. R_0 represents the initial resistance in the unstretched state, and $\varepsilon(t)$ is the applied strain at time t. Accordingly, R(t) accounts exclusively for changes arising from geometric deformation and excludes changes in intrinsic material properties.

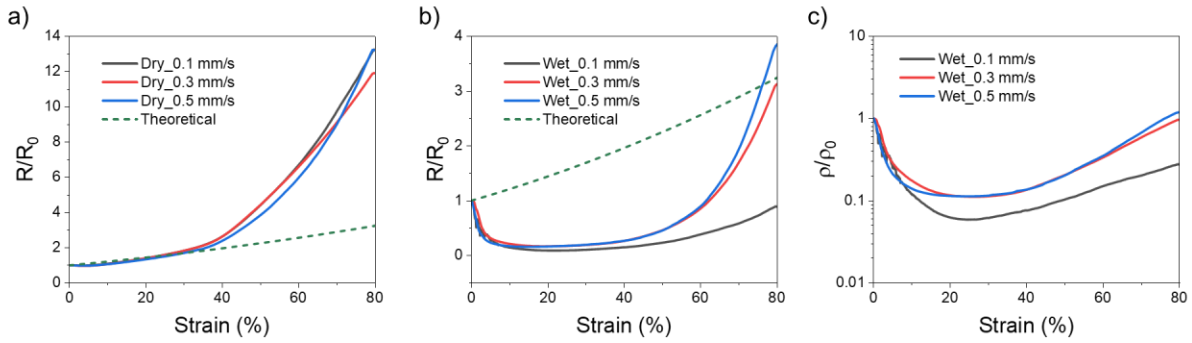

Figure 5.3 Changes in normalized resistance of (a) dry and (b) ethylene glycol (EG)–wetted PEDOT:PSS films during uniaxial stretching. (c) Corresponding resistivity trends calculated from the normalized resistance and film length

As shown in Figure 5.3a, the resistance of dry PEDOT:PSS films closely followed the theoretical prediction up to approximately 30% strain. At low strain (< 8%), a slight decrease in resistance was observed (a magnified view of this low-strain region is provided in Figure C.3, Supplementary Material), consistent with strain-induced structural rearrangement within the PEDOT:PSS network [216, 217]. Pristine PEDOT:PSS is commonly described by a core–shell morphology, consisting

of a conducting PEDOT-rich core surrounded by an insulating PSS-rich shell [218]. Under tensile deformation, partial redistribution of PEDOT segments into the surrounding PSS regions may occur, promoting coalescence of neighboring PEDOT-rich domains [216, 217]. Such reorganization can improve charge transport pathways, resulting in a modest reduction of electrical resistance. Beyond ≈30% strain, the measured resistance increased more sharply than predicted. Assuming constant film volume during stretching, this deviation suggests a reduction in the intrinsic conductivity of PEDOT:PSS. At higher strain levels. In contrast, PEDOT:PSS films wetted with EG exhibited an unconventional electromechanical response (Figure 5.3b). The electrical resistance decreased sharply within the initial ≈5% strain and continued to decrease more gradually up to ≈30% strain, after which the resistance increased upon further stretching. At a stretching rate of 0.1 mm s^{-1}, the resistance increase at high strain was minimal, whereas the highest stretching rate (0.5 mm s^{-1}) produced the largest deviation above the theoretical prediction. This negative electromechanical coupling behavior is consistent with strain-induced structural reorganization of the polymer network. EG is known to weaken interchain interactions between PEDOT and PSS and to increases the free volume of the polymer network, leading to higher chain mobility compared to the dry polymer [124, 219]. We propose that the enhanced chain mobility in the presence of EG facilitates strain-induced rearrangement of the conducting PEDOT network from a disordered to a preferentially oriented configuration under uniaxial deformation. This interpretation is consistent with previous reports showing enhanced electrical conductivity in wet-spun PEDOT:PSS microfibers subjected to stretching, which has been attributed to strain-induced chain alignment [121].

To decouple resistance changes arising from geometric deformation from those associated with intrinsic material behavior, a resistivity trend was evaluated according to:

$$\rho = R\frac{A}{L} = R\frac{V}{L^2} \tag{5.2}$$

$$\frac{\rho}{\rho_0} = \frac{R{L_0}^2}{R_0 L^2} \tag{5.3}$$

Where ρ is the film resistivity, R is the measured resistance, A is the film cross-sectional area, and L is the film length. The cross-sectional area can be expressed with V/L, where V is the film volume. Assuming that the film volume remains constant during stretching, changes in resistivity are governed by variations in resistance and length only. Accordingly, without determining

absolute resistivity values, the resistivity trend ρ/ρ_0 as a function of strain can be obtained by dividing the normalized resistance (R/R_0) by L^2/L_0^2 (Figure 5.3c).

All stretching rates exhibited a pronounced minimum in the resistivity trend at approximately 25% strain, with minimum values reaching ≈10% of the initial resistivity. This minimum suggests a strain condition associated with maximal strain-induced structural reorganization of the PEDOT:PSS network and, consequently, enhanced electrical anisotropy. On the basis of these results, wet-strain treatment for inducing anisotropy was performed on EG-wetted PEDOT:PSS films at 25% strain using a stretching rate of 0.01 mm s^{-1}.

5.4.3 Sheet resistance in different directions

The in-plane electrical anisotropy of the PEDOT:PSS films was evaluated using sheet resistance measurements. Control samples were prepared by treating unstrained films with EG for 20 min. Both wet-stretched and EG-treated unstrained films were subsequently dried in a vacuum oven at 50 °C for 12 hours. For each condition (wet-stretched and control), four independent samples were prepared, and their sheet resistances were measured in two orthogonal directions, parallel and perpendicular to the strain axis (Figure 5.4). The average values and corresponding standard deviations, used as error estimates, were calculated from these measurements.

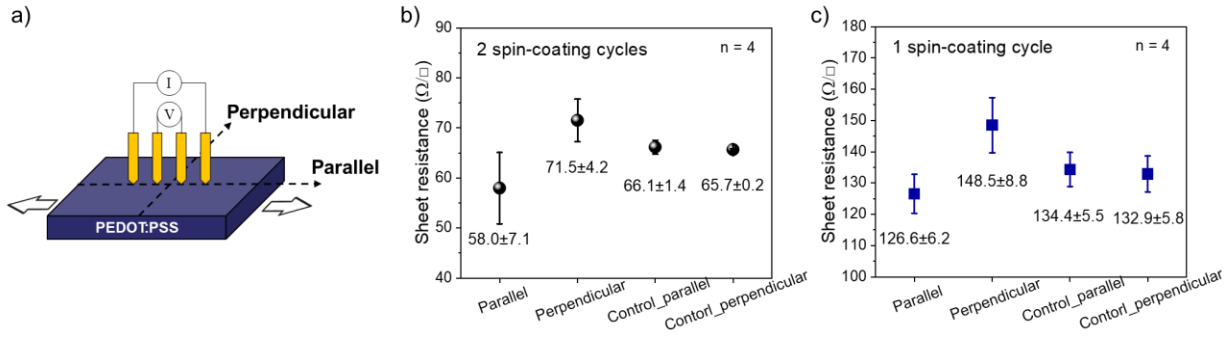

Figure 5.4 (a) Schematic illustration of the four-point probe measurements performed along directions parallel and perpendicular to the strain axis. Sheet resistance of PEDOT:PSS films prepared by (b) two and (c) one spin-coating cycles. The sheet resistances labeled control_parallel and control_perpendicular correspond to unstrained, ethylene glycol (EG)–treated PEDOT:PSS films

The overall trends were consistent for films of different thicknesses, whether spin-coated twice or once. Control samples exhibited identical sheet resistances ($R_{S,con}$) in both directions, consistent with isotropic electrical transport. In contrast, strain-treated films displayed clear directional dependence: the sheet resistance measured parallel to the strain direction ($R_{S,\parallel}$) was the lowest, whereas the perpendicular sheet resistance ($R_{S,\perp}$) was the highest.

PEDOT:PSS is a semi-crystalline material; therefore, films without strain treatment are expected to possess randomly oriented PEDOT crystallites, resulting in isotropic electrical properties. In strain-treated films, on the other hand, the PEDOT crystalline domains are expected to preferentially orient along the stretching direction, resulting in ordered domains aligned with the strain axis, with PEDOT chains predominantly directed along the applied strain. [121] In conjugated polymers such as PEDOT:PSS, charge transport is generally more efficient along the polymer backbone due to carrier delocalization over the π-conjugated chains, compared to the slower hopping-mediated transport between adjacent chains.[220] Consequently, alignment of PEDOT chains along the strain direction can promote more efficient intrachain charge transport in that direction. In addition, chain alignment in semi-crystalline conjugated polymers has been shown to improve intercrystallite transport by facilitating charge transfer between neighboring crystalline domains.[120] In general, disordered amorphous regions exhibit energetic disorder that can give rise to trap states, where charge carriers become localized, thereby limiting mobility.[221] In contrast, improved alignment within the amorphous phase can reduce tortuosity in the connecting chains linking crystalline grains, bringing these pathways closer to linear transport routes and facilitating smoother charge transport between ordered domains. Therefore, such preferential orientation can enhance hole transport when the applied electric field is parallel to the strain direction, as charge carriers encounter shorter and more efficient transport pathways through both aligned crystalline and amorphous regions. Consequently, the electrical anisotropy arising from this chain alignment can be attributed predominantly to enhanced hole mobility. Notably, the difference between $R_{S,\perp}$ and $R_{S,con}$ is smaller than the resistance changes observed during electromechanical measurements (Figure 5.3c). This suggests that although significant structural reorganization occurs in the wet-stretched state, partial relaxation or redistribution of the polymer network likely takes place during the subsequent drying process.

The electrical resistance anisotropic ratios ($R_{S,\perp}/R_{S,\parallel}$) were ±0.09 for films spin-coated twice and 1.17±0.05 for films spin-coated once. These values are comparable to the anisotropy ratio reported

for brush-printed PEDOT:PSS films (about 1.23) [120]. These results demonstrate that electrically anisotropic PEDOT:PSS films with smooth and uniform surfaces can be produced through strain treatment of spin-coated layers. Importantly, this approach remains fully compatible with established PEDOT:PSS-based device architectures fabricated on flexible plastic substrates.

5.5 Conclusion

In summary, we demonstrated a strain-based strategy to fabricate in-plane anisotropic PEDOT:PSS thin films that is compatible with conventional spin-coating processes. By systematically examining the electromechanical coupling behavior of PEDOT:PSS films in dry and EG-wetted states, we identified a pronounced negative electromechanical response in wet films, consistent with enhanced polymer chain mobility and strain-induced chain reorganization. Analysis of resistivity trends revealed a distinct minimum at approximately 25% strain, which was used as a practical criterion for selecting strain-treatment conditions. PEDOT:PSS films processed under these conditions exhibited clear in-plane electrical anisotropy, with lower sheet resistance along the strain direction and anisotropy ratios comparable to those achieved using fabrication methods limited to specific device platforms. Importantly, the anisotropic films retained the smooth and uniform morphology characteristic of spin-coated layers, preserving compatibility with existing PEDOT:PSS-based devices fabricated on flexible plastic substrates. This wet-strain treatment strategy provides a scalable and device-compatible route to introduce electrical anisotropy into PEDOT:PSS thin films for electronic and energy applications.

CHAPTER 6 CONCLUSION AND PERSPECTIVES

This PhD thesis demonstrated the potential of printing technologies as scalable manufacturing approaches for soft wearable electronic devices through the development of printable bioelectronic devices, multifunctional stretchable conducting composites, and structure-engineered conducting polymer thin films. By focusing on solution-processable polymer-based materials, this work established clear relationships between material processing, microstructure evolution, electrical transport properties, and device-level performance in soft electronic systems.

In the first study, fully printable and stretchable OECTs were successfully fabricated using a PVA-based hydrogel electrolyte and PEDOT:PSS as the semiconducting channel material. Stretchable silver electrodes were used for the drain/source, gate, and interconnect structures, enabling fully deformable transistor architectures. The printed OECTs exhibited a maximum transconductance of 1.04 ± 0.13 mS and an on/off ratio of 830, demonstrating device performance comparable to conventionally fabricated OECTs. In addition, the devices maintained stable operation for 50 days and sustained tensile strain up to 110%, confirming their suitability for wearable bioelectronic applications. These results demonstrate that fully printed and mechanically compliant transistor architectures can achieve high-performance operation while enabling large-area and customizable wearable device fabrication.

In the second study, a printable multifunctional LM composite was developed as a stretchable conductor for wearable electronic applications. Through rational design and synthesis of the polymer matrix, stable dispersion of LM droplets, high printability, and environmental compatibility were achieved. The composite exhibited high electrical conductivity on the order of 10^5 S m^{-1} while maintaining extreme mechanical stretchability up to 500% strain. The material maintained stable electrical resistance under cyclic mechanical deformation between 0 and 50% strain for more than 16 hours in both ambient and aqueous environments, demonstrating robust electromechanical stability. In addition, approximately 95% of the liquid metal was recoverable using environmentally friendly solvents, highlighting the potential for sustainable and recyclable soft electronic conductor systems. This work demonstrates that polymer–LM composite systems can overcome key limitations of bare liquid metal patterning, including poor substrate wettability and limited process compatibility, enabling rapid, low-cost, and scalable fabrication of stretchable conductors on diverse substrates, including plastics for wearable electronics.

In the final study, electrical anisotropy was introduced into PEDOT:PSS thin films through an EG-assisted wet-strain treatment. This process induced strain-driven structural reorganization and alignment of PEDOT domains, enabling directional charge transport. Analysis of apparent resistivity revealed a distinct minimum at approximately 25% strain, indicating an optimal condition for microstructural reconfiguration. Under these conditions, PEDOT:PSS films exhibited clear in-plane electrical anisotropy, with lower sheet resistance along the strain direction compared to the perpendicular direction. Importantly, this processing strategy is compatible with conventional thin film fabrication and can be readily extended to printed PEDOT:PSS films. This approach provides a scalable route for engineering anisotropic electrical transport in conducting polymer thin films, which is promising for improving energy efficiency and device performance in soft and wearable electronic systems.

Overall, this thesis systematically investigated soft conductive material components for wearable electronics by integrating printable device architectures, multifunctional stretchable conductors, and structure-controlled conducting polymer thin films. Across the three works, this work demonstrated that soft, printable electronic materials can simultaneously achieve millisiemens-level transistor performance, metallic-level composite conductivity ($\approx 10^5$ S m^{-1}), extreme mechanical stretchability (up to 500% strain), and controllable anisotropic charge transport through scalable fabrication strategies compatible with established manufacturing processes. Because polymers intrinsically provide mechanical softness, solution processability, and structural tunability, polymer-based material systems provide a powerful platform for next-generation wearable electronics.

Future work will focus on extending wet-strain-induced anisotropy to printed PEDOT:PSS thin films and investigating their electromechanical behavior under dynamic deformation conditions. In addition, further development of multifunctional soft conductors with improved sustainability, environmental compatibility, and device integration capability will be essential for next-generation wearable and bioelectronic systems. The strategies developed in this thesis provide a foundation for the scalable fabrication of high-performance, mechanically compliant, and energy-efficient wearable electronic devices.

Perspectives for Future Research

To further advance the development and commercialization of wearable electronic technologies, several research directions are recommended.

First, for practical and scalable manufacturing, printing technologies should be further developed to ensure compatibility with conventional manufacturing processes. Although printing is a powerful additive manufacturing approach for soft electronics, widespread industrial adoption requires seamless integration with existing manufacturing infrastructure. In particular, further efforts are needed to improve printing resolution and patterning accuracy beyond the current limits. The development of printing techniques capable of achieving smaller feature sizes while maintaining high throughput will be essential for enabling high-density device integration and large-scale industrial production of wearable electronic systems.

Second, further development of soft conductors capable of operating in extreme environments is required. Although this thesis demonstrated multifunctional liquid metal (LM) composites that are stable under underwater conditions, next-generation wearable electronics may require reliable operation under a broader range of environmental conditions. For example, while LM composites exhibit excellent electrical conductivity and mechanical compliance near room temperature, their use at low temperatures may present challenges. Although micro- and nanoscale LM particles can exhibit freezing behavior that differs from that of bulk LM, further systematic studies are required to understand and control LM composite performance under extreme thermal environments. The development of soft conductors with stable electrical and mechanical performance across wide temperature ranges will be important for future wearable and environmental monitoring applications.

Third, future progress toward commercialization of wearable electronics will require the integration of individual device components into fully functional wearable electronic systems. To date, much of the research effort has focused on developing individual components, such as sensors, electrodes, interconnects, and transistors. However, practical wearable electronic platforms require seamless integration of multiple components into unified systems. Achieving this goal will likely require interdisciplinary and collaborative efforts across materials science, device engineering, manufacturing engineering, and system-level design. The development of fully integrated wearable electronic systems will be critical for enabling real-world applications in healthcare monitoring, human–machine interfaces, and environmental sensing.

REFERENCES

Uncategorized References

[1] G. V. Research. "Wearable technology market size, share & trends analysis report by product (eyewear & headwear, wristwear), by application (consumer electronics, healthcare), by region, and segment forecasts, 2025–2030." https://www.grandviewresearch.com/industry-analysis/wearable-technology-market (accessed.

[2] T. C. o. Optometrists. "The College of Optometrists, The Invention of Spectacles: How and Where Glasses May Have Begun." https://www.collegeoptometrists.org/the-college/museum/online-exhibitions/virtual-spectaclesgallery/the-invention-of-spectacles.html (accessed.

[3] D. Boettcher, "The "Invention" of the Wristwatch," 2019. [Online]. Available: https://www.vintagewatchstraps.com/wristwatchinvention.php.

[4] G. Myre, "From Wristwatches To Radio, How World War I Ushered in the Modern World," in *NPR*, ed, 2017.

[5] J. Stamp. "A Partial History of Headphones." https://web.archive.org/web/20130409012634/http://blogs.smithsonianmag.com/design/2013/03/a-partial-history-of-headphones/ (accessed.

[6] B. Ticknor, *Virtual reality and the criminal justice system: exploring the possibilities for correctional rehabilitation*. Bloomsbury Publishing, 2018.

[7] T. Emerson, "Mastering the art of VR: on becoming the HIT Lab cybrarian," *The Electronic Library,* vol. 11, no. 6, pp. 385-391, 1993, doi: 10.1108/eb045261.

[8] S. Mann. "Designing EyeTap digital eyeglasses for continuous lifelong capture and sharing of personal experiences." https://www.academia.edu/63760479/Designing_EyeTap_digital_eyeglasses_for_continuous_lifelong_capture_and_sharing_of_personal_experiences (accessed.

[9] C. Marshall. "The story of Fitbit: How a wooden box was bought by Google for $2.1bn." https://www.wareable.com/fitbit/story-of-fitbit-7936 (accessed.

[10] J. Biggs. "TC50: FitBit, A Fitness Gadget That Makes Us Want To Exercise." https://techcrunch.com/2008/09/09/tc50-fitbit-fitness-gadget-the-makes-us-want-to-exercise/?utm_source=chatgpt.com (accessed.

[11] "Watch Out: A Timely History of the Smartwatch." Media Genesis. (accessed.

[12] E. B. Picaro. "Google Glass: A brief history." Pocket-lint. https://www.pocket-lint.com/ar-vr/news/google/132399-google-glass-a-brief-history/ (accessed.

[13] A. Channa, N. Popescu, J. Skibinska, and R. Burget, "The Rise of Wearable Devices during the COVID-19 Pandemic: A Systematic Review," *Sensors (Basel),* vol. 21, no. 17, Aug 28 2021, doi: 10.3390/s21175787.

[14] S. Huhn *et al.*, "The Impact of Wearable Technologies in Health Research: Scoping Review," *JMIR Mhealth Uhealth,* vol. 10, no. 1, p. e34384, Jan 25 2022, doi: 10.2196/34384.

[15] S. Fan *et al.*, "Digital health technology combining wearable gait sensors and machine learning improve the accuracy in prediction of frailty," *Front Public Health,* vol. 11, p. 1169083, 2023, doi: 10.3389/fpubh.2023.1169083.

[16] J. Yin, S. Wang, T. Tat, and J. Chen, "Motion artefact management for soft bioelectronics," *Nature Reviews Bioengineering,* vol. 2, no. 7, pp. 541-558, 2024, doi: 10.1038/s44222-024-00175-4.

[17] J. Kim *et al.*, "Ultrathin Soft Wearable Sensor Materials and Structures: A Review of Current Trends and Prospectives," *ACS Appl. Mater. Interfaces,* vol. 17, no. 44, pp. 59994-60027, Nov 5 2025, doi: 10.1021/acsami.5c14329.

[18] S. Liu, Y. Rao, H. Jang, P. Tan, and N. Lu, "Strategies for body-conformable electronics," *Matter,* vol. 5, no. 4, pp. 1104-1136, 2022, doi: 10.1016/j.matt.2022.02.006.

[19] S. Stuart *et al.*, "Critical Design Considerations for Longer-Term Wear and Comfort of On-Body Medical Devices," *Bioengineering (Basel),* vol. 11, no. 11, Oct 24 2024, doi: 10.3390/bioengineering11111058.

[20] K. Liu, B. Ouyang, X. Guo, Y. Guo, and Y. Liu, "Advances in flexible organic field-effect transistors and their applications for flexible electronics," *npj Flex. Electron.,* vol. 6, no. 1, 2022, doi: 10.1038/s41528-022-00133-3.

[21] S. Gupta, W. T. Navaraj, L. Lorenzelli, and R. Dahiya, "Ultra-thin chips for high-performance flexible electronics," *npj Flex. Electron.,* vol. 2, no. 1, 2018, doi: 10.1038/s41528-018-0021-5.

[22] A. Ometov *et al.*, "A Survey on Wearable Technology: History, State-of-the-Art and Current Challenges," *Computer Networks,* vol. 193, 2021, doi: 10.1016/j.comnet.2021.108074.

[23] S. Zhang and F. Cicoira, "Flexible self-powered biosensors," *Nature,* vol. 561, no. 7724, pp. 466-467, Sep 2018, doi: 10.1038/d41586-018-06788-1.

[24] A. Ali, H. Shaukat, S. Bibi, W. A. Altabey, M. Noori, and S. A. Kouritem, "Recent progress in energy harvesting systems for wearable technology," *Energy Strategy Reviews,* vol. 49, 2023, doi: 10.1016/j.esr.2023.101124.

[25] G. Cameron. "3D Concrete Printing: Commercial Construction's New Frontier." ConstructConnect. https://news.constructconnect.com/3d-concrete-printing-commercial-constructions-new-frontier?utm_source=chatgpt.com (accessed.

[26] D. X. H. Raghu Das. "Flexible, Printed and Organic Electronics 2020-2030: Forecasts, Technologies, Markets." IDTechEx. https://www.idtechex.com/en/research-report/flexible-printed-and-organic-electronics-2020-2030-forecasts-technologies-markets/687 (accessed.

[27] R. Søndergaard, M. Hösel, D. Angmo, T. T. Larsen-Olsen, and F. C. Krebs, "Roll-to-roll fabrication of polymer solar cells," *Mater. Today,* vol. 15, no. 1-2, pp. 36-49, 2012, doi: 10.1016/s1369-7021(12)70019-6.

[28] H. Wu, Y. Tian, H. Luo, H. Zhu, Y. Duan, and Y. Huang, "Fabrication Techniques for Curved Electronics on Arbitrary Surfaces," *Adv. Mater. Technol.,* vol. 5, no. 8, 2020, doi: 10.1002/admt.202000093.

[29] P. Martins *et al.*, "Advances in Printing and Electronics: From Engagement to Commitment," *Adv. Funct. Mater.,* vol. 33, no. 16, 2023, doi: 10.1002/adfm.202213744.

[30] H. Yi *et al.*, "Material and process integrated innovations in Aerosol Jet Printing: A review," *Mater. Today,* vol. 91, pp. 431-458, 2025, doi: 10.1016/j.mattod.2025.11.001.

[31] H. Liu *et al.*, "3D Printed Flexible Strain Sensors: From Printing to Devices and Signals," *Adv. Mater.,* vol. 33, no. 8, p. e2004782, Feb 2021, doi: 10.1002/adma.202004782.

[32] K. Sim *et al.*, "Metal oxide semiconductor nanomembrane-based soft unnoticeable multifunctional electronics for wearable human-machine interfaces," *Sci. Adv.,* vol. 5, no. 8, p. eaav9653, Aug 2019, doi: 10.1126/sciadv.aav9653.

[33] J. C. Yang *et al.*, "Geometrically engineered rigid island array for stretchable electronics capable of withstanding various deformation modes," *Sci. Adv.,* vol. 8, no. 22, p. eabn3863, Jun 3 2022, doi: 10.1126/sciadv.abn3863.

[34] C. H. Kim, M. Azimi, J. Fan, H. Nagarajan, M. Wang, and F. Cicoira, "All-printed and stretchable organic electrochemical transistors using a hydrogel electrolyte," *Nanoscale,* vol. 15, no. 7, pp. 3263-3272, Feb 16 2023, doi: 10.1039/d2nr06731e.

[35] Y. Jiang *et al.*, "A universal interface for plug-and-play assembly of stretchable devices," *Nature,* vol. 614, no. 7948, pp. 456-462, Feb 2023, doi: 10.1038/s41586-022-05579-z.

[36] D. H. Kim *et al.*, "Epidermal electronics," *Science,* vol. 333, no. 6044, pp. 838-43, Aug 12 2011, doi: 10.1126/science.1206157.

[37] S. Park *et al.*, "Self-powered ultra-flexible electronics via nano-grating-patterned organic photovoltaics," *Nature,* vol. 561, no. 7724, pp. 516-521, Sep 2018, doi: 10.1038/s41586-018-0536-x.

[38] Z. Rao *et al.*, "Curvy, shape-adaptive imagers based on printed optoelectronic pixels with a kirigami design," *Nat. Electron.,* vol. 4, no. 7, pp. 513-521, 2021, doi: 10.1038/s41928-021-00600-1.

[39] J. H. Koo *et al.*, "A vacuum-deposited polymer dielectric for wafer-scale stretchable electronics," *Nat. Electron.,* vol. 6, no. 2, pp. 137-145, 2023, doi: 10.1038/s41928-023-00918-y.

[40] M. Kaltenbrunner *et al.*, "An ultra-lightweight design for imperceptible plastic electronics," *Nature,* vol. 499, no. 7459, pp. 458-63, Jul 25 2013, doi: 10.1038/nature12314.

[41] H. Shirakawa, E. J. Louis, A. G. MacDiarmid, C. K. Chiang, and A. J. Heeger, "Synthesis of electrically conducting organic polymers: halogen derivatives of polyacetylene, (CH) x," *J. Chem. Soc., Chem. Commun.,* no. 16, 1977, doi: 10.1039/c39770000578.

[42] A. J. Heeger, "Semiconducting and Metallic Polymers: The Fourth Generation of Polymeric Materials," *J. Phys. Chem. B,* vol. 105, no. 36, pp. 8475-8491, 2001, doi: 10.1021/jp011611w.

[43] H. K. Müller, J. Hocker, K. Menke, K. Ehinger, and S. Roth, "Long-term conductivity decrease in polyacetylene samples," *Synthetic Metals,* vol. 10, no. 4, pp. 273-280, 1985, doi: 10.1016/0379-6779(85)90033-5.

[44] G. Tourillon and F. Garnier, "New electrochemically generated organic conducting polymers," *Journal of Electroanalytical Chemistry and Interfacial Electrochemistry,* vol. 135, no. 1, pp. 173-178, 1982, doi: 10.1016/0022-0728(82)90015-8.

[45] M. Shimizu *et al.*, "Two-Step Synthesis of 3,4-Ethylenedioxythiophene (EDOT) from 2,3-Butanedione," *Heterocycles,* vol. 88, no. 1, 2014, doi: 10.3987/com-13-s(s)8.

[46] J. Rivnay *et al.*, "High-performance transistors for bioelectronics through tuning of channel thickness," *Sci. Adv.,* vol. 1, no. 4, p. e1400251, May 2015, doi: 10.1126/sciadv.1400251.

[47] J. Rivnay, S. Inal, A. Salleo, R. M. Owens, M. Berggren, and G. G. Malliaras, "Organic electrochemical transistors," *Nature Reviews Materials,* vol. 3, no. 2, 2018, doi: 10.1038/natrevmats.2017.86.

[48] D. A. Bernards and G. G. Malliaras, "Steady-State and Transient Behavior of Organic Electrochemical Transistors," *Adv. Funct. Mater.,* vol. 17, no. 17, pp. 3538-3544, 2007, doi: 10.1002/adfm.200601239.

[49] D. Khodagholy *et al.*, "High transconductance organic electrochemical transistors," *Nat. Commun.,* vol. 4, p. 2133, 2013, doi: 10.1038/ncomms3133.

[50] F. Torricelli *et al.*, "Electrolyte-gated transistors for enhanced performance bioelectronics," *Nat Rev Methods Primers,* vol. 1, 2021, doi: 10.1038/s43586-021-00065-8.

[51] M. Azimi, C. H. Kim, J. Fan, and F. Cicoira, "Effect of ionic conductivity of electrolyte on printed planar and vertical organic electrochemical transistors," *Faraday Discuss.,* vol. 246, no. 0, pp. 540-555, Oct 12 2023, doi: 10.1039/d3fd00065f.

[52] M. J. Donahue *et al.*, "High-Performance Vertical Organic Electrochemical Transistors," *Adv. Mater.,* vol. 30, no. 5, Feb 2018, doi: 10.1002/adma.201705031.

[53] S. Inal, G. G. Malliaras, and J. Rivnay, "Benchmarking organic mixed conductors for transistors," *Nat. Commun.,* vol. 8, no. 1, p. 1767, Nov 24 2017, doi: 10.1038/s41467-017-01812-w.

[54] Y. Tian *et al.*, "Connective tissue inspired elastomer-based hydrogel for artificial skin via radiation-indued penetrating polymerization," *Nat. Commun.,* vol. 15, no. 1, p. 636, Jan 20 2024, doi: 10.1038/s41467-024-44949-1.

[55] T. Valayil Varghese *et al.*, "Multijet Gold Nanoparticle Inks for Additive Manufacturing of Printed and Wearable Electronics," *ACS Mater Au,* vol. 4, no. 1, pp. 65-73, Jan 10 2024, doi: 10.1021/acsmaterialsau.3c00058.

[56] B. Begines *et al.*, "Design of highly stabilized nanocomposite inks based on biodegradable polymer-matrix and gold nanoparticles for Inkjet Printing," *Sci. Rep.,* vol. 9, no. 1, p. 16097, Nov 6 2019, doi: 10.1038/s41598-019-52314-2.

[57] L. Seufert *et al.*, "Stretchable Tissue-Like Gold Nanowire Composites with Long-Term Stability for Neural Interfaces," *Small,* vol. 20, no. 43, p. e2402214, Oct 2024, doi: 10.1002/smll.202402214.

[58] B. Zhu, S. Gong, and W. Cheng, "Softening gold for elastronics," *Chem. Soc. Rev.,* vol. 48, no. 6, pp. 1668-1711, Mar 18 2019, doi: 10.1039/c8cs00609a.

[59] S. Ding *et al.*, "One-Step Fabrication of Stretchable Copper Nanowire Conductors by a Fast Photonic Sintering Technique and Its Application in Wearable Devices," *ACS Appl. Mater. Interfaces,* vol. 8, no. 9, pp. 6190-9, Mar 9 2016, doi: 10.1021/acsami.5b10802.

[60] W. Li *et al.*, "The rise of conductive copper inks: challenges and perspectives," *Applied Materials Today,* vol. 18, 2020, doi: 10.1016/j.apmt.2019.100451.

[61] S. Hong *et al.*, "Antioxidant high-conductivity copper paste for low-cost flexible printed electronics," *npj Flex. Electron.,* vol. 6, no. 1, 2022, doi: 10.1038/s41528-022-00151-1.

[62] T. Sakorikar *et al.*, "A Guide to Printed Stretchable Conductors," *Chem Rev,* vol. 124, no. 3, pp. 860-888, Feb 14 2024, doi: 10.1021/acs.chemrev.3c00569.

[63] L. Mo *et al.*, "Silver Nanoparticles Based Ink with Moderate Sintering in Flexible and Printed Electronics," *Int. J. Mol. Sci.,* vol. 20, no. 9, Apr 29 2019, doi: 10.3390/ijms20092124.

[64] N. Matsuhisa *et al.*, "Printable elastic conductors by in situ formation of silver nanoparticles from silver flakes," *Nat. Mater.,* vol. 16, no. 8, pp. 834-840, Aug 2017, doi: 10.1038/nmat4904.

[65] J. Kim *et al.*, "High-Quality Microprintable and Stretchable Conductors for High-Performance 5G Wireless Communication," *ACS Appl. Mater. Interfaces,* vol. 14, no. 47, pp. 53250-53260, Nov 30 2022, doi: 10.1021/acsami.2c18424.

[66] J. Liang, K. Tong, and Q. Pei, "A Water-Based Silver-Nanowire Screen-Print Ink for the Fabrication of Stretchable Conductors and Wearable Thin-Film Transistors," *Adv. Mater.,* vol. 28, no. 28, pp. 5986-96, Jul 2016, doi: 10.1002/adma.201600772.

[67] Y. Chen, R. S. Carmichael, and T. B. Carmichael, "Patterned, Flexible, and Stretchable Silver Nanowire/Polymer Composite Films as Transparent Conductive Electrodes," *ACS Appl. Mater. Interfaces,* vol. 11, no. 34, pp. 31210-31219, Aug 28 2019, doi: 10.1021/acsami.9b11149.

[68] D. C. Kim, H. J. Shim, W. Lee, J. H. Koo, and D. H. Kim, "Material-Based Approaches for the Fabrication of Stretchable Electronics," *Adv. Mater.,* vol. 32, no. 15, p. 1902743, Apr 2020, doi: 10.1002/adma.201902743.

[69] H. Joo, D. Jung, S. H. Sunwoo, J. H. Koo, and D. H. Kim, "Material Design and Fabrication Strategies for Stretchable Metallic Nanocomposites," *Small,* vol. 16, no. 11, p. 1906270, Mar 2020, doi: 10.1002/smll.201906270.

[70] A. Hajalilou *et al.*, "Digitally Printable Magnetic Liquid Metal Composite for Recyclable Soft-Matter Electronics," *Adv. Mater. Technol.,* vol. 8, no. 10, p. 2201621, 2023, doi: 10.1002/admt.202201621.

[71] R. Tutika, A. B. M. T. Haque, and M. D. Bartlett, "Self-healing liquid metal composite for reconfigurable and recyclable soft electronics," *Commun. Mater.,* vol. 2, no. 1, p. 64, 2021, doi: 10.1038/s43246-021-00169-4.

[72] S. H. Jeong, A. Hagman, K. Hjort, M. Jobs, J. Sundqvist, and Z. Wu, "Liquid alloy printing of microfluidic stretchable electronics," *Lab Chip,* vol. 12, no. 22, pp. 4657-64, Nov 21 2012, doi: 10.1039/c2lc40628d.

[73] N. Lazarus, S. S. Bedair, and I. M. Kierzewski, "Ultrafine Pitch Stencil Printing of Liquid Metal Alloys," *ACS Appl. Mater. Interfaces,* vol. 9, no. 2, pp. 1178-1182, Jan 18 2017, doi: 10.1021/acsami.6b13088.

[74] J. W. Boley, E. L. White, G. T. C. Chiu, and R. K. Kramer, "Direct Writing of Gallium-Indium Alloy for Stretchable Electronics," *Adv. Funct. Mater.,* vol. 24, no. 23, pp. 3501-3507, 2014, doi: 10.1002/adfm.201303220.

[75] Y. G. Park, H. S. An, J. Y. Kim, and J. U. Park, "High-resolution, reconfigurable printing of liquid metals with three-dimensional structures," *Sci. Adv.,* vol. 5, no. 6, p. eaaw2844, Jun 2019, doi: 10.1126/sciadv.aaw2844.

[76] Y. Lin, O. Gordon, M. R. Khan, N. Vasquez, J. Genzer, and M. D. Dickey, "Vacuum filling of complex microchannels with liquid metal," *Lab Chip,* vol. 17, no. 18, pp. 3043-3050, Sep 12 2017, doi: 10.1039/c7lc00426e.

[77] Q. Gao, H. Li, J. Zhang, Z. Xie, J. Zhang, and L. Wang, "Microchannel Structural Design For a Room-Temperature Liquid Metal Based Super-stretchable Sensor," *Sci. Rep.,* vol. 9, no. 1, p. 5908, Apr 11 2019, doi: 10.1038/s41598-019-42457-7.

[78] B. A. Gozen, A. Tabatabai, O. B. Ozdoganlar, and C. Majidi, "High-density soft-matter electronics with micron-scale line width," *Adv. Mater.,* vol. 26, no. 30, pp. 5211-6, Aug 13 2014, doi: 10.1002/adma.201400502.

[79] C. W. Park *et al.*, "Photolithography-Based Patterning of Liquid Metal Interconnects for Monolithically Integrated Stretchable Circuits," *ACS Appl. Mater. Interfaces,* vol. 8, no. 24, pp. 15459-65, Jun 22 2016, doi: 10.1021/acsami.6b01896.

[80] G. Li and D. W. Lee, "An advanced selective liquid-metal plating technique for stretchable biosensor applications," *Lab Chip,* vol. 17, no. 20, pp. 3415-3421, Oct 11 2017, doi: 10.1039/c7lc00768j.

[81] M. G. Kim, D. K. Brown, and O. Brand, "Nanofabrication for all-soft and high-density electronic devices based on liquid metal," *Nat. Commun.,* vol. 11, no. 1, p. 1002, Feb 21 2020, doi: 10.1038/s41467-020-14814-y.

[82] P. Bhuyan, Y. Wei, M. Choe, D. Cho, S. Lee, and S. Park, "Liquid-metal-microdroplets-incorporated ultrasoft dielectric gel toward stretchable and healable waste-energy-harvesting devices," *Nano Energy,* vol. 108, p. 108214, 2023, doi: 10.1016/j.nanoen.2023.108214.

[83] G. H. Lee *et al.*, "Rapid meniscus-guided printing of stable semi-solid-state liquid metal microgranular-particle for soft electronics," *Nat. Commun.,* vol. 13, no. 1, p. 2643, May 12 2022, doi: 10.1038/s41467-022-30427-z.

[84] S. Chen *et al.*, "Ultrahigh Strain-Insensitive Integrated Hybrid Electronics Using Highly Stretchable Bilayer Liquid Metal Based Conductor," *Adv. Mater.,* vol. 35, no. 5, p. 2208569, Feb 2023, doi: 10.1002/adma.202208569.

[85] S. Liu *et al.*, "Laser Sintering of Liquid Metal Nanoparticles for Scalable Manufacturing of Soft and Flexible Electronics," *ACS Appl. Mater. Interfaces,* vol. 10, no. 33, pp. 28232-28241, Aug 22 2018, doi: 10.1021/acsami.8b08722.

[86] G. Wang, J. Chen, W. Zheng, and B. Shen, "High-efficiency flexible liquid metal/elastomer composite film with designability for strain-invariant electromagnetic shielding and Joule-heating applications," *Chem. Eng. J.,* vol. 488, p. 151052, 2024, doi: 10.1016/j.cej.2024.151052.

[87] E. J. Markvicka, M. D. Bartlett, X. Huang, and C. Majidi, "An autonomously electrically self-healing liquid metal-elastomer composite for robust soft-matter robotics and electronics," *Nat. Mater.,* vol. 17, no. 7, pp. 618-624, Jul 2018, doi: 10.1038/s41563-018-0084-7.

[88] E. J. Barron, E. T. Williams, B. T. Wilcox, D. H. Ho, and M. D. Bartlett, "Liquid metal-elastomer composites for water-resilient soft electronics," *J. Polym. Sci.,* vol. 62, no. 16, pp. 3818-3829, 2023, doi: 10.1002/pol.20230616.

[89] J. Xu *et al.*, "Printable and Recyclable Conductive Ink Based on a Liquid Metal with Excellent Surface Wettability for Flexible Electronics," *ACS Appl. Mater. Interfaces,* vol. 13, no. 6, pp. 7443-7452, Feb 17 2021, doi: 10.1021/acsami.0c20549.

[90] G. Scheiblin *et al.*, "Screen-printed organic electrochemical transistors for metabolite sensing," *MRS Commun.,* vol. 5, no. 3, pp. 507-511, 2015, doi: 10.1557/mrc.2015.52.

[91] L. Contat-Rodrigo, C. Perez-Fuster, J. V. Lidon-Roger, A. Bonfiglio, and E. Garcia-Breijo, "Characterization of Screen-Printed Organic Electrochemical Transistors to Detect Cations of Different Sizes," *Sensors (Basel),* vol. 16, no. 10, Sep 28 2016, doi: 10.3390/s16101599.

[92] M. Afonso, J. Morgado, and L. Alcacer, "Inkjet printed organic electrochemical transistors with highly conducting polymer electrolytes," (in English), *J. Appl. Phys.,* vol. 120, no. 16, Oct 28 2016, doi: Artn 165502

10.1063/1.4966651.

[93] L. Contat-Rodrigo, C. Pérez-Fuster, J. V. Lidón-Roger, A. Bonfiglio, and E. García-Breijo, "Screen-printed Organic Electrochemical Transistors for the detection of ascorbic acid in food," *Org. Electron.,* vol. 45, pp. 89-96, 2017, doi: 10.1016/j.orgel.2017.02.037.

[94] M. Berto *et al.*, "Label free urea biosensor based on organic electrochemical transistors," (in English), *Flex. Print. Electron.,* vol. 3, no. 2, Jun 2018, doi: ARTN 024001

10.1088/2058-8585/aac8a8.

[95] E. J. Strand *et al.*, "Printed Organic Electrochemical Transistors for Detecting Nutrients in Whole Plant Sap," (in English), *Adv. Electron. Mater.,* vol. 8, no. 4, Apr 2022, doi: ARTN 2100853

10.1002/aelm.202100853.

[96] M. Sensi *et al.*, "Monitoring DNA Hybridization with Organic Electrochemical Transistors Functionalized with Polydopamine," (in English), *Macromol. Mater. Eng.,* vol. 307, no. 5, May 2022, doi: ARTN 2100880

10.1002/mame.202100880.

[97] T. Someya, Z. Bao, and G. G. Malliaras, "The rise of plastic bioelectronics," *Nature,* vol. 540, no. 7633, pp. 379-385, Dec 14 2016, doi: 10.1038/nature21004.

[98] C. G. Bischak, L. Q. Flagg, and D. S. Ginger, "Ion Exchange Gels Allow Organic Electrochemical Transistor Operation with Hydrophobic Polymers in Aqueous Solution," *Adv. Mater.,* vol. 32, no. 32, p. e2002610, Aug 2020, doi: 10.1002/adma.202002610.

[99] C. Qian *et al.*, "Artificial Synapses Based on in-Plane Gate Organic Electrochemical Transistors," *ACS Appl. Mater. Interfaces,* vol. 8, no. 39, pp. 26169-26175, Oct 5 2016, doi: 10.1021/acsami.6b08866.

[100] L.-a. Kong *et al.*, "Long-term synaptic plasticity simulated in ionic liquid/polymer hybrid electrolyte gated organic transistors," *Org. Electron.,* vol. 47, pp. 126-132, 2017, doi: 10.1016/j.orgel.2017.05.017.

[101] M. Petkovic, K. R. Seddon, L. P. Rebelo, and C. Silva Pereira, "Ionic liquids: a pathway to environmental acceptability," *Chem. Soc. Rev.,* vol. 40, no. 3, pp. 1383-403, Mar 2011, doi: 10.1039/c004968a.

[102] W. Wang *et al.*, "High-Transconductance, Highly Elastic, Durable and Recyclable All-Polymer Electrochemical Transistors with 3D Micro-Engineered Interfaces," *Nano-Micro Lett.,* vol. 14, no. 1, p. 184, Sep 12 2022, doi: 10.1007/s40820-022-00930-5.

[103] H. Yuk, B. Lu, and X. Zhao, "Hydrogel bioelectronics," *Chem. Soc. Rev.,* vol. 48, no. 6, pp. 1642-1667, Mar 18 2019, doi: 10.1039/c8cs00595h.

[104] X. Liu, J. Liu, S. Lin, and X. Zhao, "Hydrogel machines," *Mater. Today,* vol. 36, pp. 102-124, 2020, doi: 10.1016/j.mattod.2019.12.026.

[105] Y. J. Jo, K. Y. Kwon, Z. U. Khan, X. Crispin, and T. I. Kim, "Gelatin Hydrogel-Based Organic Electrochemical Transistors and Their Integrated Logic Circuits," *ACS Appl. Mater. Interfaces,* vol. 10, no. 45, pp. 39083-39090, Nov 14 2018, doi: 10.1021/acsami.8b11362.

[106] J. Ko, X. Wu, A. Surendran, B. T. Muhammad, and W. L. Leong, "Self-Healable Organic Electrochemical Transistor with High Transconductance, Fast Response, and Long-Term Stability," *ACS Appl. Mater. Interfaces,* vol. 12, no. 30, pp. 33979-33988, 2020, doi: 10.1021/acsami.0c07913.

[107] J. Bai *et al.*, "Coin-sized, fully integrated, and minimally invasive continuous glucose monitoring system based on organic electrochemical transistors," *Sci. Adv.,* vol. 10, no. 16, p. eadl1856, Apr 19 2024, doi: 10.1126/sciadv.adl1856.

[108] I. Cunha *et al.*, "Healable Cellulose Iontronic Hydrogel Stickers for Sustainable Electronics on Paper," (in English), *Adv. Electron. Mater.,* vol. 7, no. 3, Mar 2021, doi: ARTN 2001166

10.1002/aelm.202001166.

[109] S. R. Dupont, F. Novoa, E. Voroshazi, and R. H. Dauskardt, "Decohesion Kinetics of PEDOT:PSS Conducting Polymer Films," *Adv. Funct. Mater.,* vol. 24, no. 9, pp. 1325-1332, 2013, doi: 10.1002/adfm.201302174.

[110] A. Håkansson *et al.*, "Effect of (3-glycidyloxypropyl)trimethoxysilane (GOPS) on the electrical properties of PEDOT:PSS films," *J. Polym. Sci., Part B: Polym. Phys.,* vol. 55, no. 10, pp. 814-820, 2017, doi: 10.1002/polb.24331.

[111] J. Y. Kim, J. H. Jung, D. E. Lee, and J. Joo, "Enhancement of electrical conductivity of poly(3,4-ethylenedioxythiophene)/poly(4-styrenesulfonate) by a change of solvents," *Synthetic Metals,* vol. 126, no. 2-3, pp. 311-316, 2002, doi: 10.1016/s0379-6779(01)00576-8.

[112] J. Kim *et al.*, "Self-healing, stretchable and recyclable polyurethane-PEDOT:PSS conductive blends," *Mater Horiz,* vol. 11, no. 15, pp. 3548-3560, Jul 29 2024, doi: 10.1039/d4mh00203b.

[113] S. Zhang, P. Kumar, A. S. Nouas, L. Fontaine, H. Tang, and F. Cicoira, "Solvent-induced changes in PEDOT:PSS films for organic electrochemical transistors," *APL Materials,* vol. 3, no. 1, 2015, doi: 10.1063/1.4905154.

[114] J. G. Troughton *et al.*, "Simultaneous measurement of electrical characteristics and microstructure of crystallised PEDOT:PSS based OECTs under strain," *Org. Electron.,* vol. 92, 2021, doi: 10.1016/j.orgel.2021.106108.

[115] Y. H. Kim, C. Sachse, M. L. Machala, C. May, L. Müller-Meskamp, and K. Leo, "Highly Conductive PEDOT:PSS Electrode with Optimized Solvent and Thermal Post-Treatment for ITO-Free Organic Solar Cells," *Adv. Funct. Mater.,* vol. 21, no. 6, pp. 1076-1081, 2011, doi: 10.1002/adfm.201002290.

[116] J. A. Ávila-Niño, E. Araujo, and F. González, "Study of the doping of PEDOT:PSS films and the reversibility in organic electrochemical transistors," *Synthetic Metals,* vol. 299, 2023, doi: 10.1016/j.synthmet.2023.117465.

[117] T.-R. Chou, S.-H. Chen, Y.-T. Chiang, Y.-T. Lin, and C.-Y. Chao, "Highly conductive PEDOT:PSS films by post-treatment with dimethyl sulfoxide for ITO-free liquid crystal display," *J. Mater. Chem. C,* vol. 3, no. 15, pp. 3760-3766, 2015, doi: 10.1039/c5tc00276a.

[118] S.-M. Kim *et al.*, "High-performance, polymer-based direct cellular interfaces for electrical stimulation and recording," *NPG Asia Mater.,* vol. 10, no. 4, pp. 255-265, 2018, doi: 10.1038/s41427-018-0014-9.

[119] S. M. Kim *et al.*, "Influence of PEDOT:PSS crystallinity and composition on electrochemical transistor performance and long-term stability," *Nat. Commun.,* vol. 9, no. 1, p. 3858, Sep 21 2018, doi: 10.1038/s41467-018-06084-6.

[120] B. Zhang *et al.*, "Brush and Dry: A Posttreatment-Free Simple Process to Pattern PEDOT:PSS Films with Enhanced Thermoelectric Performance via Shear Flow-Induced Morphology Tuning," *ACS Appl. Mater. Interfaces,* vol. 17, no. 13, pp. 20236-20247, Apr 2 2025, doi: 10.1021/acsami.5c00803.

[121] Y. Kim *et al.*, "Strain-Engineering Induced Anisotropic Crystallite Orientation and Maximized Carrier Mobility for High-Performance Microfiber-Based Organic Bioelectronic Devices," *Adv. Mater.,* vol. 33, no. 10, p. e2007550, Mar 2021, doi: 10.1002/adma.202007550.

[122] Z. Chen, X. Guan, N. Wen, L. Pan, and Z. Fan, "Construction of Flexible, Self-Supporting, and In-Plane Anisotropic PEDOT:PSS Thermoelectric Films via the Wet-Winding Approach," *ACS Applied Polymer Materials,* vol. 5, no. 4, pp. 2905-2916, 2023, doi: 10.1021/acsapm.3c00122.

[123] Y. W. Kim *et al.*, "Anisotropically Conductive Hydrogels with Directionally Aligned PEDOT:PSS in a PVA Matrix," *ACS Appl. Mater. Interfaces,* vol. 16, no. 3, pp. 4013-4023, Jan 24 2024, doi: 10.1021/acsami.3c16094.

[124] X. Fan *et al.*, "PEDOT:PSS for Flexible and Stretchable Electronics: Modifications, Strategies, and Applications," *Adv. Sci.,* vol. 6, no. 19, p. 1900813, Oct 2 2019, doi: 10.1002/advs.201900813.

[125] M. Wang *et al.*, "Artificial Skin Perception," *Adv. Mater.,* vol. 33, no. 19, p. e2003014, May 2021, doi: 10.1002/adma.202003014.

[126] T. Q. Trung and N. E. Lee, "Flexible and Stretchable Physical Sensor Integrated Platforms for Wearable Human-Activity Monitoringand Personal Healthcare," *Adv. Mater.,* vol. 28, no. 22, pp. 4338-72, Jun 2016, doi: 10.1002/adma.201504244.

[127] J. Zhao *et al.*, "Recent developments of truly stretchable thin film electronic and optoelectronic devices," *Nanoscale,* vol. 10, no. 13, pp. 5764-5792, Mar 29 2018, doi: 10.1039/c7nr09472h.

[128] Y. Wang *et al.*, "A highly stretchable, transparent, and conductive polymer," *Sci. Adv.,* vol. 3, no. 3, p. e1602076, Mar 2017, doi: 10.1126/sciadv.1602076.

[129] S. Wang *et al.*, "Skin electronics from scalable fabrication of an intrinsically stretchable transistor array," *Nature,* vol. 555, no. 7694, pp. 83-88, Mar 1 2018, doi: 10.1038/nature25494.

[130] Y. Dai *et al.*, "Stretchable Redox-Active Semiconducting Polymers for High-Performance Organic Electrochemical Transistors," *Adv. Mater.,* vol. 34, no. 23, p. e2201178, Jun 2022, doi: 10.1002/adma.202201178.

[131] W. Lee *et al.*, "Nonthrombogenic, stretchable, active multielectrode array for electroanatomical mapping," *Sci. Adv.,* vol. 4, no. 10, p. eaau2426, Oct 2018, doi: 10.1126/sciadv.aau2426.

[132] Y. Z. Li, N. X. Wang, A. N. Yang, H. F. Ling, and F. Yan, "Biomimicking Stretchable Organic Electrochemical Transistor," (in English), *Adv. Electron. Mater.,* vol. 5, no. 10, Oct 2019, doi: ARTN 1900566

10.1002/aelm.201900566.

[133] S. Zhang, E. Hubis, C. Girard, P. Kumar, J. DeFranco, and F. Cicoira, "Water stability and orthogonal patterning of flexible micro-electrochemical transistors on plastic," *J. Mater. Chem. C,* vol. 4, no. 7, pp. 1382-1385, 2016, doi: 10.1039/c5tc03664j.

[134] X. Du, S. P. Wankhede, S. Prasad, A. Shehri, J. Morse, and N. Lakal, "A review of inkjet printing technology for personalized-healthcare wearable devices," *J. Mater. Chem. C,* vol. 10, no. 38, pp. 14091-14115, 2022, doi: 10.1039/d2tc02511f.

[135] F. A. Viola *et al.*, "A sub-150-nanometre-thick and ultraconformable solution-processed all-organic transistor," *Nat. Commun.,* vol. 12, no. 1, p. 5842, Oct 6 2021, doi: 10.1038/s41467-021-26120-2.

[136] F. Molina-Lopez *et al.*, "Inkjet-printed stretchable and low voltage synaptic transistor array," *Nat. Commun.,* vol. 10, no. 1, p. 2676, Jun 18 2019, doi: 10.1038/s41467-019-10569-3.

[137] S. Demuru *et al.*, "All-Inkjet-Printed Graphene-Gated Organic Electrochemical Transistors on Polymeric Foil as Highly Sensitive Enzymatic Biosensors," *ACS Appl. Nano Mater.,* vol. 5, no. 1, pp. 1664-1673, 2022, doi: 10.1021/acsanm.1c04434.

[138] B. Schmatz, A. W. Lang, and J. R. Reynolds, "Fully Printed Organic Electrochemical Transistors from Green Solvents," (in English), *Adv. Funct. Mater.,* vol. 29, no. 44, Nov 2019, doi: ARTN 1905266

10.1002/adfm.201905266.

[139] M. Zabihipour *et al.*, "High yield manufacturing of fully screen-printed organic electrochemical transistors," *npj Flex. Electron.,* vol. 4, no. 1, 2020, doi: 10.1038/s41528-020-0078-9.

[140] P. Andersson Ersman *et al.*, "Screen printed digital circuits based on vertical organic electrochemical transistors," *Flex. Print. Electron.,* vol. 2, no. 4, 2017, doi: 10.1088/2058-8585/aa903a.

[141] M. Zabihipour, D. Y. Tu, J. Strandberg, M. Berggren, I. Engquist, and P. A. Ersman, "Designing Inverters Based on Screen Printed Organic Electrochemical Transistors Targeting Low-Voltage and High-Frequency Operation," (in English), *Adv. Mater. Technol.,* vol. 6, no. 12, Dec 2021, doi: ARTN 2100555

10.1002/admt.202100555.

[142] P. Andersson Ersman *et al.*, "Monolithic integration of display driver circuits and displays manufactured by screen printing," *Flex. Print. Electron.,* vol. 5, no. 2, 2020, doi: 10.1088/2058-8585/ab7ab4.

[143] J. H. Cho *et al.*, "Printable ion-gel gate dielectrics for low-voltage polymer thin-film transistors on plastic," *Nat. Mater.,* vol. 7, no. 11, pp. 900-6, Nov 2008, doi: 10.1038/nmat2291.

[144] Y. Xia, J. Cho, B. Paulsen, C. D. Frisbie, and M. J. Renn, "Correlation of on-state conductance with referenced electrochemical potential in ion gel gated polymer transistors," *Appl. Phys. Lett.,* vol. 94, no. 1, 2009, doi: 10.1063/1.3058694.

[145] D. Song, F. Zare Bidoky, E. B. Secor, M. C. Hersam, and C. D. Frisbie, "Freestanding Ion Gels for Flexible, Printed, Multifunctional Microsupercapacitors," *ACS Appl. Mater. Interfaces,* vol. 11, no. 10, pp. 9947-9954, Mar 13 2019, doi: 10.1021/acsami.8b20766.

[146] E. M. Jung, S. W. Lee, and S. H. Kim, "Printed ion-gel transistor using electrohydrodynamic (EHD) jet printing process," *Org. Electron.,* vol. 52, pp. 123-129, 2018, doi: 10.1016/j.orgel.2017.10.013.

[147] H. Lee, S. Lee, W. Lee, T. Yokota, K. Fukuda, and T. Someya, "Ultrathin Organic Electrochemical Transistor with Nonvolatile and Thin Gel Electrolyte for Long-Term Electrophysiological Monitoring," (in English), *Adv. Funct. Mater.,* vol. 29, no. 48, Nov 2019, doi: ARTN 1906982

10.1002/adfm.201906982.

[148] P. C. Hutter, T. Rothlander, G. Scheipl, and B. Stadlober, "All Screen-Printed Logic Gates Based on Organic Electrochemical Transistors," *IEEE Trans. Electron Devices,* vol. 62, no. 12, pp. 4231-4236, 2015, doi: 10.1109/ted.2015.2491342.

[149] Y. Y. A *et al.*, "Biodegradable Polycarbonate Iongels for Electrophysiology Measurements," *Polymers,* vol. 10, no. 9, Sep 5 2018, doi: 10.3390/polym10090989.

[150] S. Han, S. Yu, S. Hu, H.-j. Chen, J. Wu, and C. Liu, "A high endurance, temperature-resilient, and robust organic electrochemical transistor for neuromorphic circuits," *J. Mater. Chem. C,* vol. 9, no. 35, pp. 11801-11808, 2021, doi: 10.1039/d1tc02215f.

[151] S. J. Han, S. L. Yu, S. J. Hu, X. C. Liang, Y. Y. Luo, and C. Liu, "Ion transport to temperature and gate in organic electrochemical transistors with anti-freezing hydrogel," (in English), *Org. Electron.,* vol. 108, Sep 2022, doi: ARTN 106605

10.1016/j.orgel.2022.106605.

[152] Z. Wu, X. Yang, and J. Wu, "Conductive Hydrogel- and Organohydrogel-Based Stretchable Sensors," *ACS Appl. Mater. Interfaces,* vol. 13, no. 2, pp. 2128-2144, Jan 20 2021, doi: 10.1021/acsami.0c21841.

[153] S. Peng, S. Liu, Y. Sun, N. Xiang, X. Jiang, and L. Hou, "Facile preparation and characterization of poly(vinyl alcohol)-NaCl-glycerol supramolecular hydrogel electrolyte," *Eur. Polym. J.,* vol. 106, pp. 206-213, 2018, doi: 10.1016/j.eurpolymj.2018.07.024.

[154] F. Yokoyama, I. Masada, K. Shimamura, T. Ikawa, and K. Monobe, "Morphology and structure of highly elastic poly(vinyl alcohol) hydrogel prepared by repeated freezing-and-melting," *Colloid Polym. Sci.,* vol. 264, no. 7, pp. 595-601, 1986, doi: 10.1007/bf01412597.

[155] J. Hagler *et al.*, "Flexible and stretchable printed conducting polymer devices for electrodermal activity measurements," (in English), *Flex. Print. Electron.,* vol. 7, no. 1, Mar 1 2022, doi: ARTN 014008

10.1088/2058-8585/ac4d0f.

[156] S. Zhang, E. Hubis, G. Tomasello, G. Soliveri, P. Kumar, and F. Cicoira, "Patterning of Stretchable Organic Electrochemical Transistors," *Chem. Mater.,* vol. 29, no. 7, pp. 3126-3132, 2017, doi: 10.1021/acs.chemmater.7b00181.

[157] J. Chen *et al.*, "Highly stretchable organic electrochemical transistors with strain-resistant performance," *Nat. Mater.,* vol. 21, no. 5, pp. 564-571, May 2022, doi: 10.1038/s41563-022-01239-9.

[158] T. D. Nguyen, T. Q. Trung, Y. Lee, and N. E. Lee, "Stretchable and Stable Electrolyte-Gated Organic Electrochemical Transistor Synapse with a Nafion Membrane for Enhanced Synaptic Properties," (in English), *Adv. Eng. Mater.,* vol. 24, no. 4, Apr 2022, doi: ARTN 2100918

10.1002/adem.202100918.

[159] M. Kohler, P. Lunkenheimer, and A. Loidl, "Dielectric and conductivity relaxation in mixtures of glycerol with LiCl," *Eur. Phys. J. E Soft Matter,* vol. 27, no. 2, pp. 115-22, Oct 2008, doi: 10.1140/epje/i2008-10357-8.

[160] L. Zhao, L. Pan, Z. Cao, and Q. Wang, "Mutual Effects of Glycerol and Inorganic Salts on Their Hydration Abilities," *J. Phys. Chem. B,* vol. 120, no. 51, pp. 13112-13117, Dec 29 2016, doi: 10.1021/acs.jpcb.6b08778.

[161] C. Lu *et al.*, "In Situ Characterization of Dehydration during Ion Transport in Polymeric Nanochannels," *J. Am. Chem. Soc.,* vol. 143, no. 35, pp. 14242-14252, Sep 8 2021, doi: 10.1021/jacs.1c05765.

[162] R. Morais, D. H. Vieira, C. Gaspar, L. Pereira, R. Martins, and E. N. Alves, "Influence of paper surface characteristics on fully inkjet printed PEDOT:PSS-based electrochemical transistors," (in English), *Semicond. Sci. Technol.,* vol. 36, no. 12, Dec 2021, doi: ARTN 125005

10.1088/1361-6641/ac2de0.

[163] D. Majak, J. Fan, and M. Gupta, "Fully 3D printed OECT based logic gate for detection of cation type and concentration," *Sens. Actuators B Chem.,* vol. 286, pp. 111-118, 2019, doi: 10.1016/j.snb.2019.01.120.

[164] J. Fan, C. Montemagno, and M. Gupta, "3D printed high transconductance organic electrochemical transistors on flexible substrates," *Org. Electron.,* vol. 73, pp. 122-129, 2019, doi: 10.1016/j.orgel.2019.06.012.

[165] G. T. Go *et al.*, "Achieving Microstructure-Controlled Synaptic Plasticity and Long-Term Retention in Ion-Gel-Gated Organic Synaptic Transistors," (in English), *Adv. Intell. Syst.,* vol. 2, no. 11, Nov 2020, doi: ARTN 2000012

10.1002/aisy.202000012.

[166] S. Yamamoto, A. G. Polyravas, S. Han, and G. G. Malliaras, "Correlation between Transient Response and Neuromorphic Behavior in Organic Electrochemical Transistors," (in English), *Adv. Electron. Mater.,* vol. 8, no. 4, Apr 2022, doi: ARTN 2101186

10.1002/aelm.202101186.

[167] F. Decataldo *et al.*, "Oxygen Gas Sensing Using a Hydrogel-Based Organic Electrochemical Transistor for Work Safety Applications," *Polymers,* vol. 14, no. 5, Mar 3 2022, doi: 10.3390/polym14051022.

[168] H. Zhang, Z. Guo, C. Ma, W. Xie, and W. Liu, "Study on meso-macroscopic ionic conductivity of hydrogels and construction of prediction model," *Polymer,* vol. 302, 2024, doi: 10.1016/j.polymer.2024.127048.

[169] K. H. Seol, S. J. Lee, K. G. Cho, K. Hong, and K. H. Lee, "Highly conductive, binary ionic liquid–solvent mixture ion gels for effective switching of electrolyte-gated transistors," *J. Mater. Chem. C,* vol. 6, no. 41, pp. 10987-10993, 2018, doi: 10.1039/c8tc03076f.

[170] S. M. Zhang *et al.*, "Tuning the Electromechanical Properties of PEDOT:PSS Films for Stretchable Transistors And Pressure Sensors," (in English), *Adv. Electron. Mater.,* vol. 5, no. 6, Jun 2019, doi: ARTN 1900191

10.1002/aelm.201900191.

[171] Y. Li, S. Zhang, X. Li, V. R. N. Unnava, and F. Cicoira, "Highly stretchable PEDOT:PSS organic electrochemical transistors achieved via polyethylene glycol addition," *Flex. Print. Electron.,* vol. 4, no. 4, 2019, doi: 10.1088/2058-8585/ab5202.

[172] M. Lerond, A. Subramanian, W. G. Skene, and F. Cicoira, "Combining Electrospinning and Electrode Printing for the Fabrication of Stretchable Organic Electrochemical Transistors," (in English), *FrPhy,* vol. 9, Aug 24 2021, doi: ARTN 708914

10.3389/fphy.2021.708914.

[173] S. Chang *et al.*, "Flexible and Stretchable Light-Emitting Diodes and Photodetectors for Human-Centric Optoelectronics," *Chem. Rev.,* vol. 124, no. 3, pp. 768-859, Feb 14 2024, doi: 10.1021/acs.chemrev.3c00548.

[174] D. C. Kim *et al.*, "Intrinsically stretchable quantum dot light-emitting diodes," *Nat. Electron.,* vol. 7, no. 5, pp. 365-374, 2024, doi: 10.1038/s41928-024-01152-w.

[175] D. Zhong *et al.*, "High-speed and large-scale intrinsically stretchable integrated circuits," *Nature,* vol. 627, no. 8003, pp. 313-320, Mar 2024, doi: 10.1038/s41586-024-07096-7.

[176] H. U. Chung *et al.*, "Binodal, wireless epidermal electronic systems with in-sensor analytics for neonatal intensive care," *Science,* vol. 363, no. 6430, p. eaau0780, Mar 1 2019, doi: 10.1126/science.aau0780.

[177] X. P. Hao *et al.*, "Healable, Recyclable, and Multifunctional Soft Electronics Based on Biopolymer Hydrogel and Patterned Liquid Metal," *Small,* vol. 18, no. 23, p. 2201643, Jun 2022, doi: 10.1002/smll.202201643.

[178] H. Su, H. Moeinnia, and W. S. Kim, "3D Printed Electromyography Sensing Systems," *Adv. Sensor Res.,* vol. 2, no. 9, 2023, doi: 10.1002/adsr.202300003.

[179] N. Matsuhisa, X. Chen, Z. Bao, and T. Someya, "Materials and structural designs of stretchable conductors," *Chem. Soc. Rev.,* vol. 48, no. 11, pp. 2946-2966, Jun 4 2019, doi: 10.1039/c8cs00814k.

[180] X. Su *et al.*, "A Highly Conducting Polymer for Self-Healable, Printable, and Stretchable Organic Electrochemical Transistor Arrays and Near Hysteresis-Free Soft Tactile Sensors," *Adv. Mater.,* vol. 34, no. 19, p. 2200682, May 2022, doi: 10.1002/adma.202200682.

[181] X. Zhou *et al.*, "Conducting polymer films and bioelectrodes combining high adhesion and electro-mechanical self-healing," *J. Mater. Chem. C,* vol. 12, no. 16, pp. 5708-5717, 2024, doi: 10.1039/d3tc04230h.

[182] D. Won *et al.*, "Digital selective transformation and patterning of highly conductive hydrogel bioelectronics by laser-induced phase separation," *Sci. Adv.,* vol. 8, no. 23, p. eabo3209, Jun 10 2022, doi: 10.1126/sciadv.abo3209.

[183] S. H. Sunwoo *et al.*, "Stretchable Low-Impedance Conductor with Ag-Au-Pt Core-Shell-Shell Nanowires and in Situ Formed Pt Nanoparticles for Wearable and Implantable Device," *ACS Nano,* vol. 17, no. 8, pp. 7550-7561, Apr 25 2023, doi: 10.1021/acsnano.2c12659.

[184] Z. Zhao, S. Soni, T. Lee, C. A. Nijhuis, and D. Xiang, "Smart Eutectic Gallium-Indium: From Properties to Applications," *Adv. Mater.,* vol. 35, no. 1, p. 2203391, Jan 2023, doi: 10.1002/adma.202203391.

[185] L. Teng, S. Ye, S. Handschuh-Wang, X. Zhou, T. Gan, and X. Zhou, "Liquid Metal-Based Transient Circuits for Flexible and Recyclable Electronics," *Adv. Funct. Mater.,* vol. 29, no. 11, p. 1808739, 2019, doi: 10.1002/adfm.201808739.

[186] X. Wu, Z. Qi, W. Zhang, H. Cai, X. Han, and K. Yang, "Lignin-Stabilized Tough, Sticky, and Recyclable Liquid Metal/Protein Organogels for Multifunctional Epidermal Smart Materials," *Small,* p. 2405126, Aug 6 2024, doi: 10.1002/smll.202405126.

[187] V. Vallem, V. Aggarwal, and M. D. Dickey, "Stretchable Liquid Metal Films with High Surface Area and Strain Invariant Resistance," *Adv. Mater. Technol.,* vol. 8, no. 5, 2022, doi: 10.1002/admt.202201233.

[188] J. Chen, X. Chen, Y. Su, B. Shen, and W. Zheng, "Multifunctional strain-activated liquid-metal composite films with electromechanical decoupling for stretchable electromagnetic shielding," *Mater Horiz,* vol. 11, no. 24, pp. 6381-6390, Dec 9 2024, doi: 10.1039/d4mh00774c.

[189] K. Y. Kwon *et al.*, "Surface Modification of Gallium-Based Liquid Metals: Mechanisms and Applications in Biomedical Sensors and Soft Actuators," *Adv. Intell. Syst.,* vol. 3, no. 3, p. 2000159, 2020, doi: 10.1002/aisy.202000159.

[190] K. Schlingman, G. M. D'Amaral, R. S. Carmichael, and T. B. Carmichael, "Intrinsically Conductive Liquid Metal-Elastomer Composites for Stretchable and Flexible Electronics," *Adv. Mater. Technol.,* vol. 8, no. 1, p. 2200374, 2022, doi: 10.1002/admt.202200374.

[191] S. P. Pujari, L. Scheres, A. T. Marcelis, and H. Zuilhof, "Covalent surface modification of oxide surfaces," *Angew Chem Int Ed Engl,* vol. 53, no. 25, pp. 6322-56, Jun 16 2014, doi: 10.1002/anie.201306709.

[192] H. Bark and P. S. Lee, "Surface modification of liquid metal as an effective approach for deformable electronics and energy devices," *Chem. Sci.,* vol. 12, no. 8, pp. 2760-2777, Feb 2 2021, doi: 10.1039/d0sc05310d.

[193] H.-F. Wen *et al.*, "Soft Poly(butyl acrylate) Side Chains toward Intrinsically Stretchable Polymeric Semiconductors for Field-Effect Transistor Applications," *Macromolecules,* vol. 50, no. 13, pp. 4982-4992, 2017, doi: 10.1021/acs.macromol.7b00860.

[194] R. Wang, P.-M. Wang, and X.-G. Li, "Physical and mechanical properties of styrene–butadiene rubber emulsion modified cement mortars," *Cem. Concr. Res.,* vol. 35, no. 5, pp. 900-906, 2005, doi: 10.1016/j.cemconres.2004.07.012.

[195] Q. Wei *et al.*, "Surface Engineering of Liquid Metal Nanodroplets by Attachable Diblock Copolymers," *ACS Nano,* vol. 14, no. 8, pp. 9884-9893, Aug 25 2020, doi: 10.1021/acsnano.0c02720.

[196] B. Fan, J. Wan, Y. Liu, W. W. Tian, and S. H. Thang, "Functionalization of liquid metal nanoparticles via the RAFT process," *Polym. Chem.,* vol. 12, no. 20, pp. 3015-3025, 2021, doi: 10.1039/d1py00257k.

[197] J. Ma, F. Krisnadi, M. H. Vong, M. Kong, O. M. Awartani, and M. D. Dickey, "Shaping a Soft Future: Patterning Liquid Metals," *Adv. Mater.,* vol. 35, no. 19, p. 2205196, May 2023, doi: 10.1002/adma.202205196.

[198] G.-H. Lee *et al.*, "Large-area photo-patterning of initially conductive EGaIn particle-assembled film for soft electronics," *Mater. Today,* vol. 67, pp. 84-94, 2023, doi: 10.1016/j.mattod.2023.05.025.

[199] G. Yun *et al.*, "Liquid metal-filled magnetorheological elastomer with positive piezoconductivity," *Nat. Commun.,* vol. 10, no. 1, p. 1300, Mar 21 2019, doi: 10.1038/s41467-019-09325-4.

[200] Z. Luo and X. Zhou, "Ternary Liquid Metal Polymer Composite for Stretchable Electronics," *Adv. Mater. Technol.,* vol. 9, no. 7, 2023, doi: 10.1002/admt.202301638.

[201] M. Tobiszewski, J. Namieśnik, and F. Pena-Pereira, "Environmental risk-based ranking of solvents using the combination of a multimedia model and multi-criteria decision analysis," *Green Chem.,* vol. 19, no. 4, pp. 1034-1042, 2017, doi: 10.1039/c6gc03424a.

[202] M. Clausén, L.-O. Öhman, J. D. Kubicki, and P. Persson, "Characterisation of gallium(iii)-acetate complexes in aqueous solution: A potentiometric, EXAFS, IR and molecular orbital modelling study," *J. Chem. Soc., Dalton Trans.,* no. 12, pp. 2559-2564, 2002, doi: 10.1039/b111408e.

[203] Z. J. Farrell and C. Tabor, "Control of Gallium Oxide Growth on Liquid Metal Eutectic Gallium/Indium Nanoparticles via Thiolation," *Langmuir,* vol. 34, no. 1, pp. 234-240, Jan 9 2018, doi: 10.1021/acs.langmuir.7b03384.

[204] Z. Qu, F. Hu, K. Chen, Z. Duan, H. Gu, and H. Xu, "A facile route to the synthesis of spherical poly(acrylic acid) brushes via RAFT polymerization for high-capacity protein immobilization," *J Colloid Interface Sci,* vol. 398, pp. 82-87, May 15 2013, doi: 10.1016/j.jcis.2013.02.001.

[205] T. Pirman, M. Ocepek, and B. Likozar, "Radical Polymerization of Acrylates, Methacrylates, and Styrene: Biobased Approaches, Mechanism, Kinetics, Secondary Reactions, and Modeling," *Ind. Eng. Chem. Res.,* vol. 60, no. 26, pp. 9347-9367, 2021, doi: 10.1021/acs.iecr.1c01649.

[206] S. Zhu, Y. Huang, and B. Fang, "Progress and Prospect for Conducting Polymer Fibers," *Adv. Mater.,* vol. 37, no. 48, p. e04071, Dec 2025, doi: 10.1002/adma.202504071.

[207] J. Y. Gerasimov, M. J. Donahue, D. Gao, D. Tu, and S. Fabiano, "Electropolymerization of Organic Mixed Ionic-Electronic Conductors: Fundamentals and Applications in Bioelectronics," *Chem Rev,* vol. 126, no. 1, pp. 28-79, Jan 14 2026, doi: 10.1021/acs.chemrev.5c00183.

[208] A. E. Avila Ramirez, D. P. van der Laan, M. B. Shah, L. Wang, E. Zeglio, and A. Savva, "PEDOT:PSS-A Key Material for Bioelectronics," *Adv. Sci.,* p. e13480, Dec 23 2025, doi: 10.1002/advs.202513480.

[209] M. Wang *et al.*, "Robust and flexible organic electrochemical transistors enabled by electropolymerized PEDOT," *Npj Flex Electron,* vol. 9, no. 1, p. 74, 2025, doi: 10.1038/s41528-025-00457-w.

[210] S. Han *et al.*, "Implantable Ion-Selective Organic Electrochemical Transistors Enable Continuous, Long-Term, and In Vivo Plant Monitoring," *Adv. Sci.,* vol. 12, no. 41, p. e04283, Nov 2025, doi: 10.1002/advs.202504283.

[211] B. Seufert, S. Thomas, and A. Takshi, "Colloidal SnO2 nanoparticles for the enhancement of PEDOT:PSS-coated string electrodes for potential use for glucose sensing," *MRS Advances,* vol. 9, no. 9, pp. 678-683, 2024, doi: 10.1557/s43580-024-00821-4.

[212] V. A. Zarubin *et al.*, "Improved Anisotropic Thermoelectric Behavior of Poly(3,4-ethylenedioxythiophene):Poly(styrenesulfonate) via Magnetophoresis," *ACS Omega,* vol. 3, no. 10, pp. 12554-12561, Oct 31 2018, doi: 10.1021/acsomega.8b00999.

[213] M. S. Mahajan, D. M. Marathe, S. S. Ghosh, V. Ganesan, and J. V. Sali, "Changes in in-plane electrical conductivity of PEDOT:PSS thin films due to electric field induced dipolar reorientation," *RSC Advances,* vol. 5, no. 105, pp. 86393-86401, 2015, doi: 10.1039/c5ra13610e.

[214] G. Dijk, H. J. Ruigrok, and R. P. O'Connor, "Influence of PEDOT:PSS Coating Thickness on the Performance of Stimulation Electrodes," *Advanced Materials Interfaces,* vol. 7, no. 16, 2020, doi: 10.1002/admi.202000675.

[215] S. Zhang *et al.*, "Tuning the Electromechanical Properties of PEDOT:PSS Films for Stretchable Transistors And Pressure Sensors," *Adv. Electron. Mater.,* vol. 5, no. 6, 2019, doi: 10.1002/aelm.201900191.

[216] Y. Y. Lee *et al.*, "Stretching-Induced Growth of PEDOT-Rich Cores: A New Mechanism for Strain-Dependent Resistivity Change in PEDOT:PSS Films," *Adv. Funct. Mater.,* vol. 23, no. 32, pp. 4020-4027, 2013, doi: 10.1002/adfm.201203670.

[217] Y. Y. Lee *et al.*, "Growth Mechanism of Strain-Dependent Morphological Change in PEDOT:PSS Films," *Sci. Rep.,* vol. 6, p. 25332, Apr 29 2016, doi: 10.1038/srep25332.

[218] J. Rivnay *et al.*, "Structural control of mixed ionic and electronic transport in conducting polymers," *Nat. Commun.,* vol. 7, p. 11287, Apr 19 2016, doi: 10.1038/ncomms11287.

[219] S. M. Jorge *et al.*, "Free-Standing, Water-Resistant, and Conductivity-Enhanced PEDOT:PSS Films from In Situ Polymerization of 3-Hydroxymethyl-3-Methyl-Oxetane," *Polymers,* vol. 16, no. 16, Aug 14 2024, doi: 10.3390/polym16162292.

[220] M. N. Gueye, A. Carella, J. Faure-Vincent, R. Demadrille, and J.-P. Simonato, "Progress in understanding structure and transport properties of PEDOT-based materials: A critical review," *Progress in Materials Science,* vol. 108, 2020, doi: 10.1016/j.pmatsci.2019.100616.

[221] R. Noriega *et al.*, "A general relationship between disorder, aggregation and charge transport in conjugated polymers," *Nat. Mater.,* vol. 12, no. 11, pp. 1038-44, Nov 2013, doi: 10.1038/nmat3722.

APPENDIX A SUPPORTING INFORMATION OF ARTICLE 1: ALL-PRINTED AND STRETCHABLE ORGANIC ELECTROCHEMICAL TRANSISTORS USING A HYDROGEL ELECTROLYTE

Chi-hyeong Kim, Mona Azimi, Jiaxin Fan, Harini Nagarajan, Meijing Wang, and Fabio Cicoira*

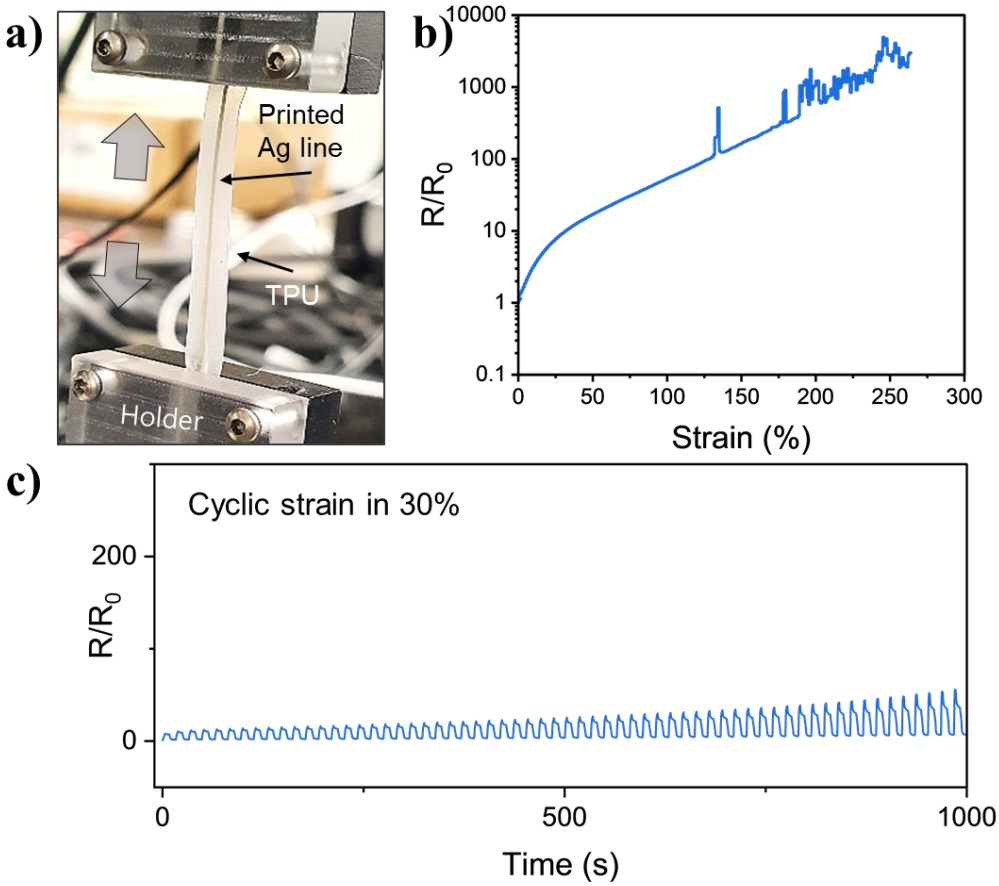

Figure A.1 Electromechanical test of a printed stretchable Ag electrode. a) Digital photo of the sample. b) Normalized resistance (R) with respect to the initial resistance (R0) at 0% while stretching until break. c) 30% cyclic tensile strain test. 10 mA was applied in b) and c)

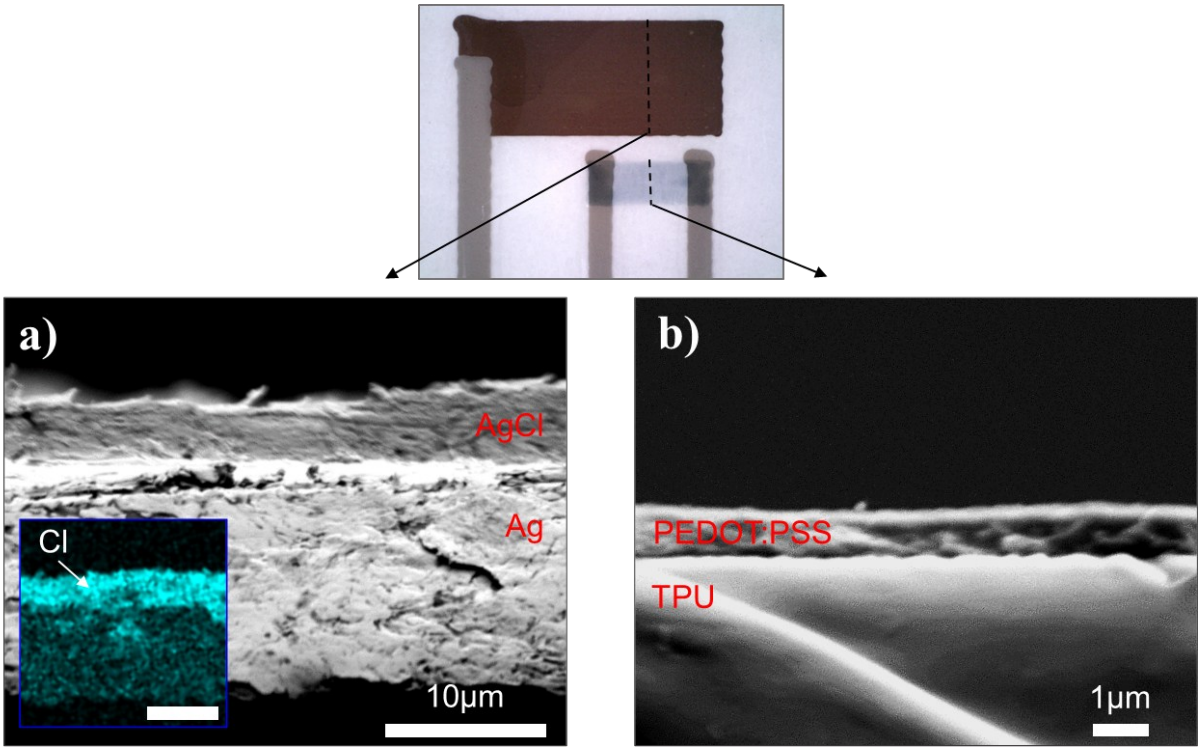

Figure A.2 FE-SEM cross-sectional images a) printed Ag/AgCl gate. The inset shows Cl element in AgCl layer by Energy-dispersive X-ray spectroscopy (scale bar: 10μm). b) printed PEDOT:PSS channel on TPU substrate.

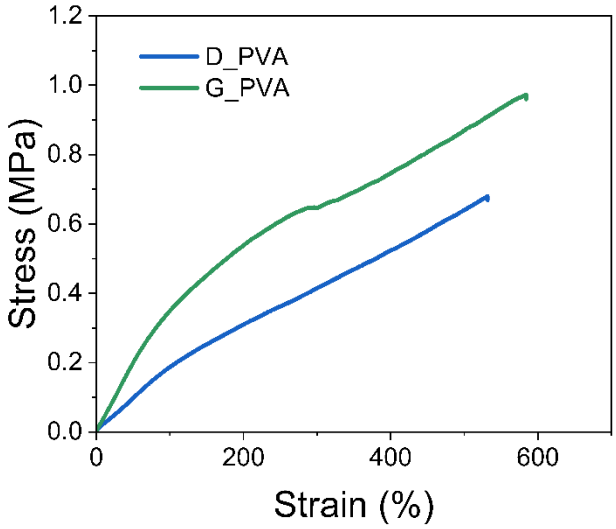

Figure A.3 Stress-strain curve of hydrogel tensile test.

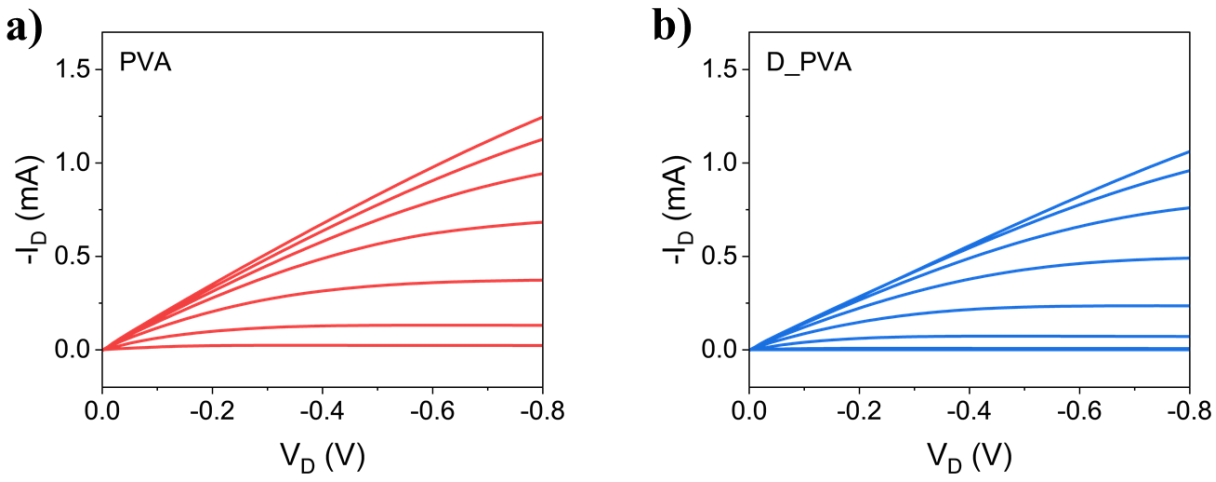

Figure A.4 Output curves of a) PVA and b) D_PVA OECT. (V_G from -0.6 to 0.8 V in 0.2 V steps)

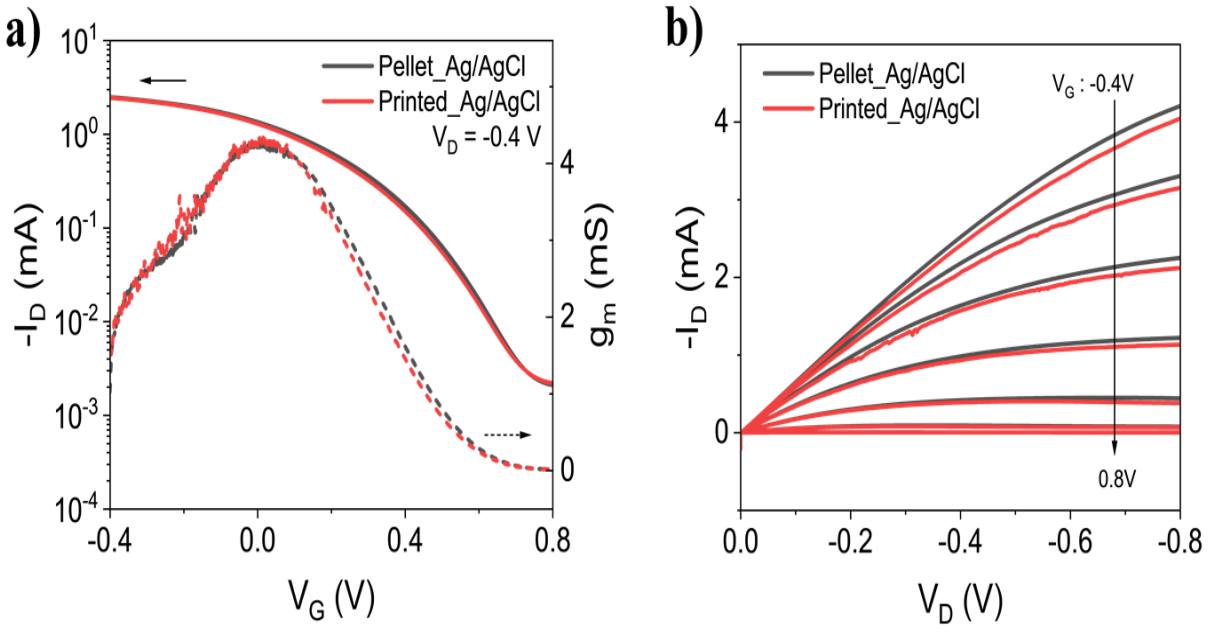

Figure A.5 Comparison of I-V characteristics measured with a pellet and a printed Ag/AgCl gate a) transfer curves and b) output curves. The dimension of Ag/AgCl pellet (Warner Instruments) is 4 mm diameter and 1 mm thickness. The electrolyte is a 0.1 M NaCl solution.

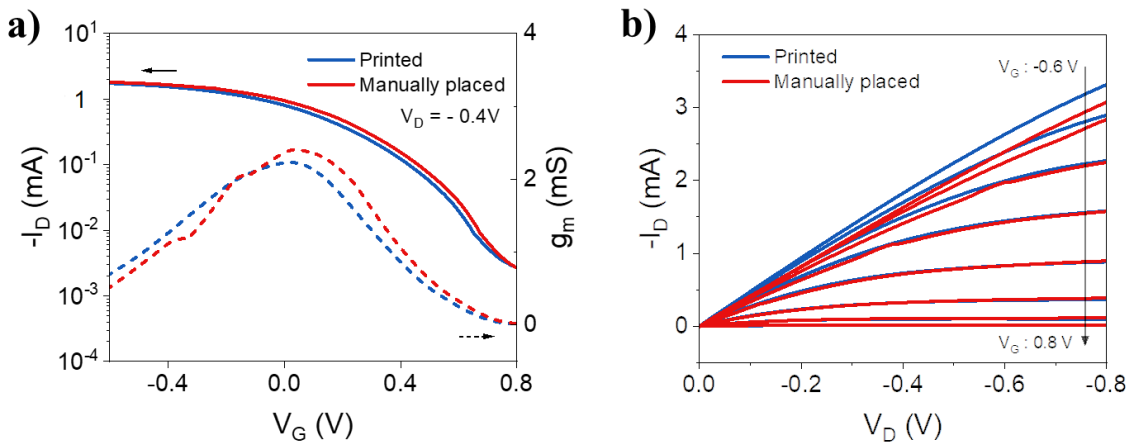

Figure A.6 Comparison of I-V characteristics measured with printed and manually attached PVA hydrogel electrolytes on the OECTs a) transfer curves and b) output curves.

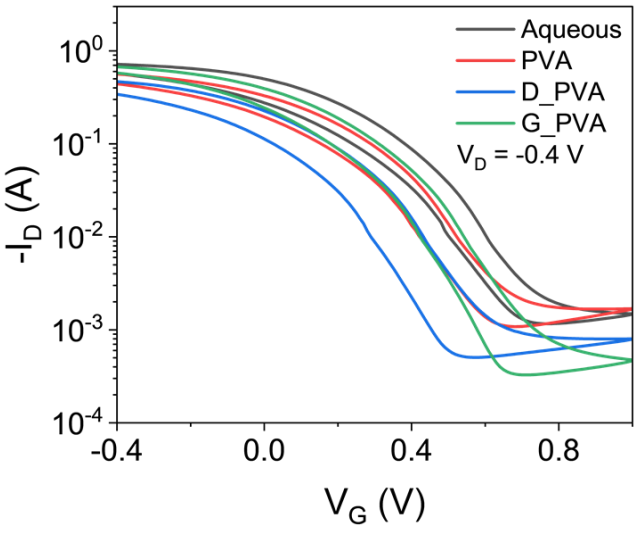

Figure A.7 Transfer curves with 4 types of electrolytes, including backward sweep of gate voltage

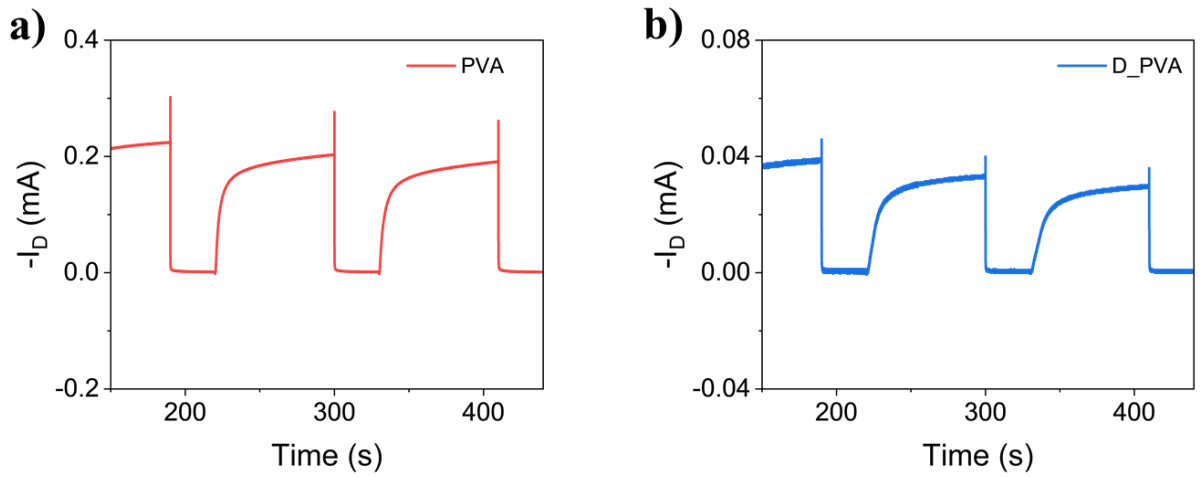

Figure A.8 Transient responses of a) PVA a) and b) D_PVA OECTs. (V_D = -0.4 V and ΔV_G = 0.7 V)

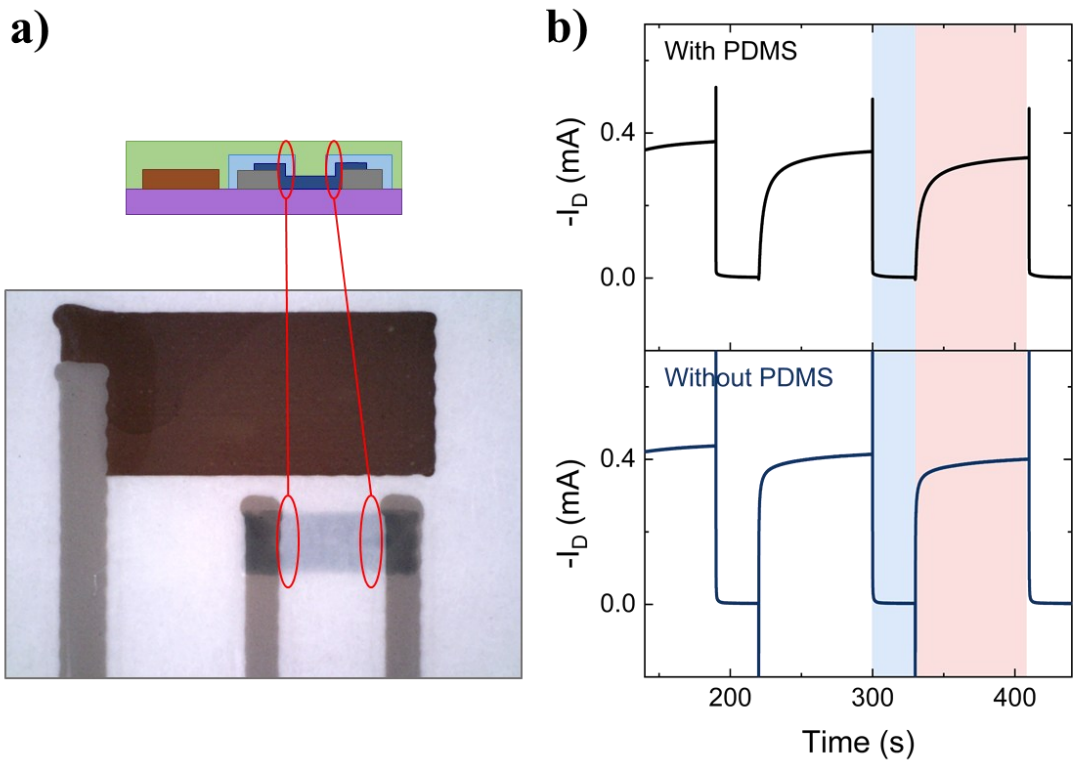

Figure A.9 a) A scheme and a microscopic image of the OECT, indicating PDMS covering the PEDOT:PSS layer. b) Comparison of transient responses between the aqueous electrolyte-gated OECT with and without PDMS cover. The blue and red area indicate on-to-off and off-to-on responses, respectively. V_D = -0.4 V and 0.7 V gate pulses were applied.

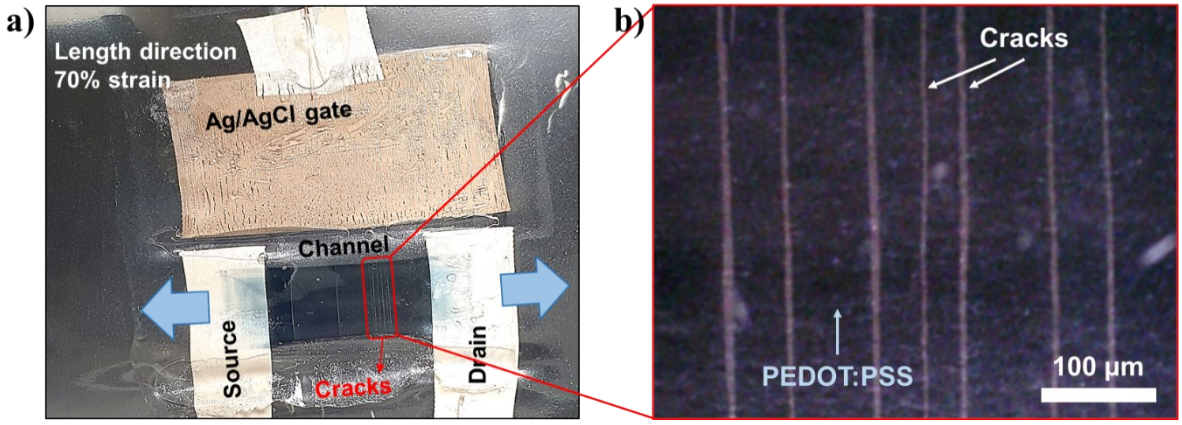

Figure A.10 a) A digital photo of a stretched OECT in length direction at 70%. b) A microscopic image of micro-cracks on PEDOT:PSS channel.

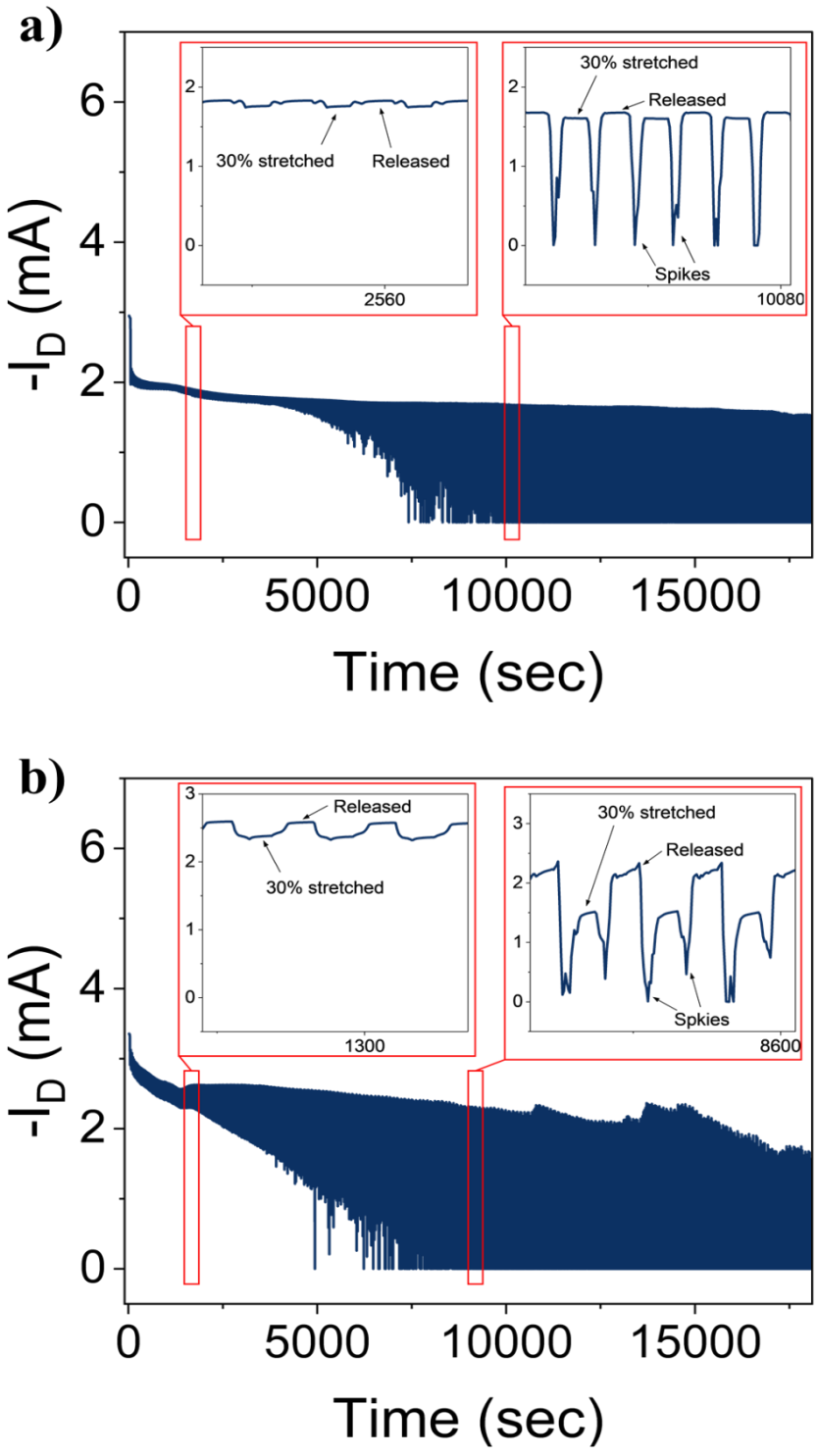

Figure A.11 The drain current measured under 30% cyclic strains in a) the length direction and b) the width direction. The device was biased at V_D = -0.4 V and V_G = 0 V. The insets are magnified plots.

APPENDIX B SUPPORTING INFORMATION OF ARTICLE 2: RECYCLABLE PRINTED LIQUID METAL COMPOSITE FOR UNDERWATER STRETCHABLE ELECTRONICS

Chi-hyeong Kim, Jinsil Kim, Jiaxin Fan, Meijing Wang, Fabio Cicoira

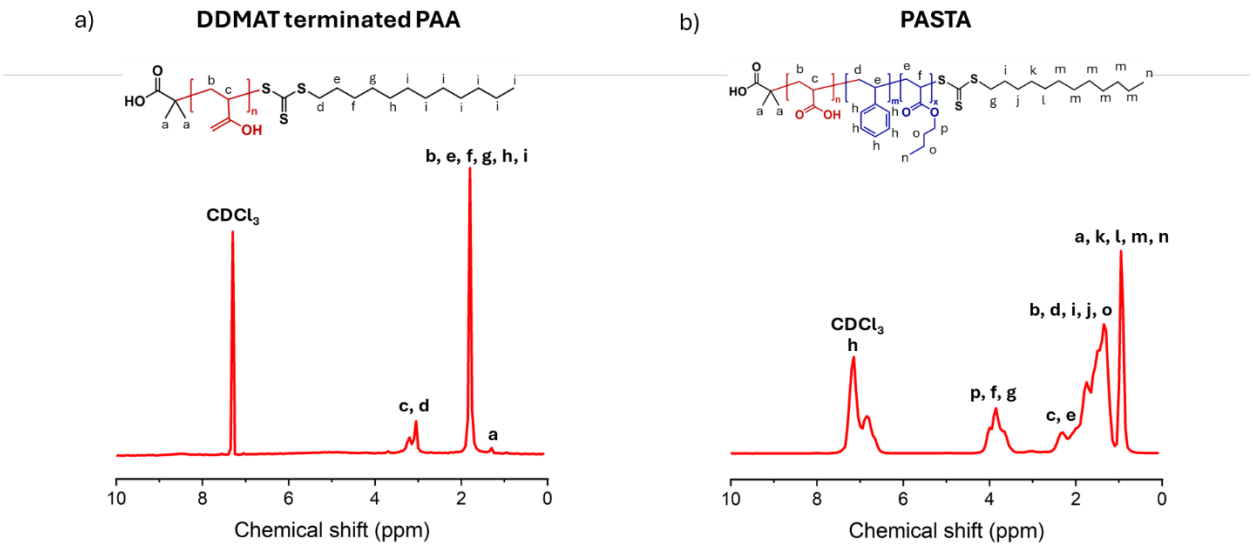

Figure B.1 ^{1}H-NMR of a) DDMAT-terminated PAA and b) PASTA. The chemical structures of the synthesized polymers were verified with ^{1}H-NMR.

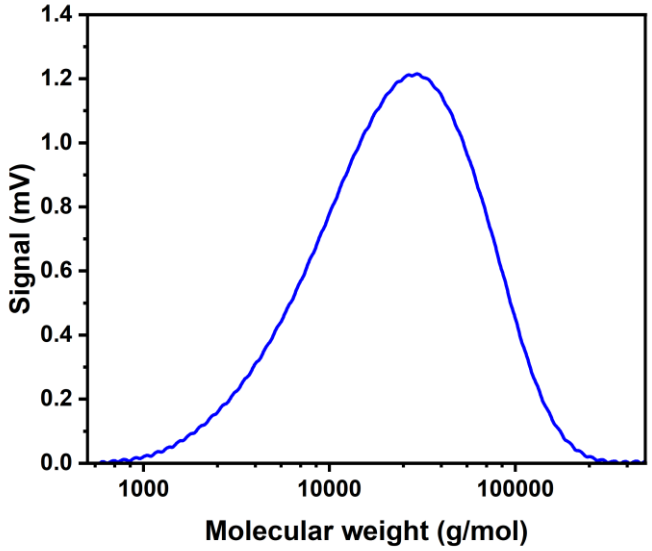

Figure B.2 GPC of PASTA. The molecular weight averages and PDI of PASTA were extracted from the GPC data. Mw = 68 ± 1 kg/mol, M_n = 34 ± 1 kg/mol, PDI = 2 ± 0.1

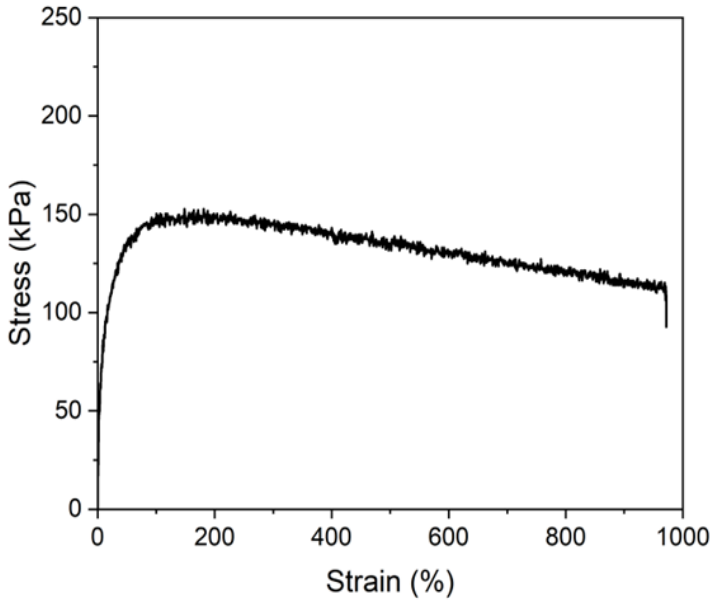

Figure B.3 Tensile stress-strain curve of PASTA.

Mechanical characterization achieved via tensile stress-strain curves indicates that free-standing polymer films exhibit an elastic deformation range up to 40% strain and are stretchable up to at least 900%. Additionally, for applied strains higher than 100%, we observed a decrease in the stress as the strain increased. The behavior can be correlated with the low glass transition (*T*g) of the material since the linear chains of PASTA may have high mobility at temperatures higher than *T*g and can show a stress decrease in the mechanical ductile region.

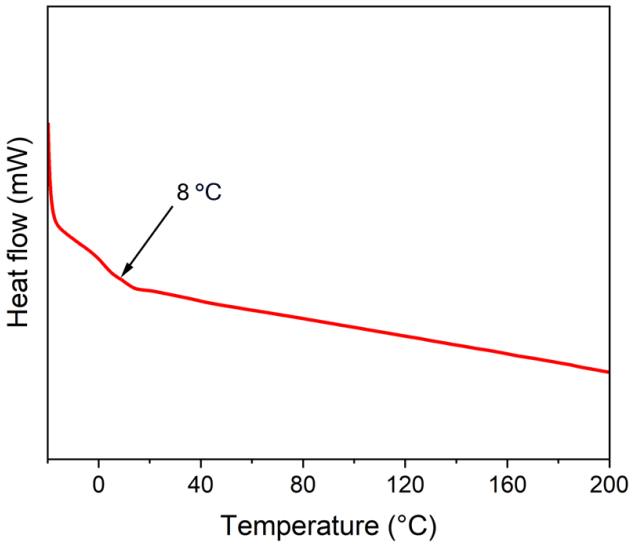

Figure B.4 Differential scanning calorimetry of PASTA.

From DSC, *T*g of PASTA is around 8°C. Hence, PASTA demonstrated high stretchability and low *T*g, which are suitable properties for LM composite development.

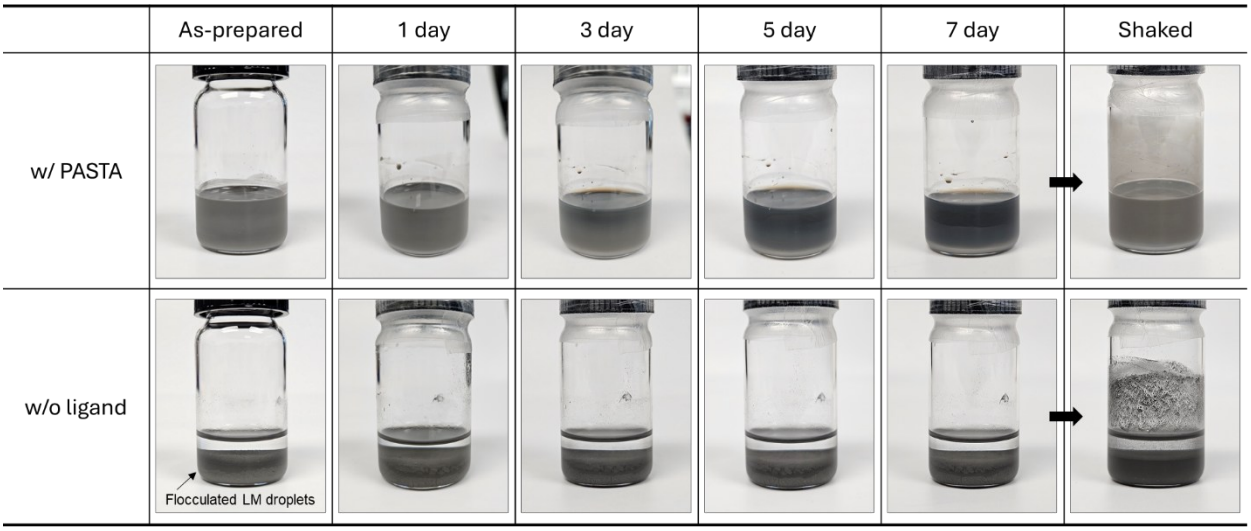

Figure B.5 Digital Photos of LM suspension stability test over time.

The LM/PASTA suspension was gradually less homogeneous from 3 days, indicating the LM droplets slowly flocculated due to the gravity effect. The separated layer in the LM suspension was observed at 7 days. However, the polymer-grafted LM suspension could be recovered to its homogeneity with shaking by hand, compared to the sedimented bare LM droplets after shaking.

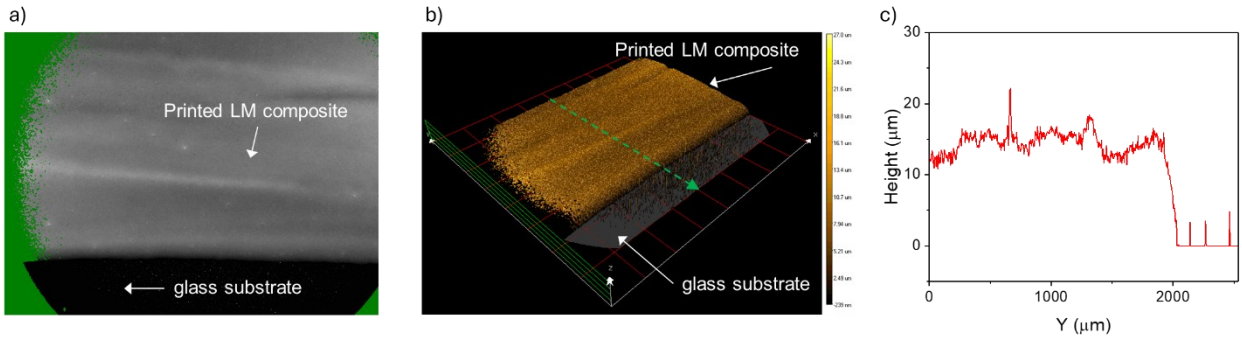

Figure B.6 Surface profile of a printed LM composite measured by the white light interferometer. a) Optical and b) 3D images of the composite. c) Cross-sectional profile of the composite, which was cut at the green dash line in the 3D image. The average thickness is 14.44 ± 3.01 μm (n=5).

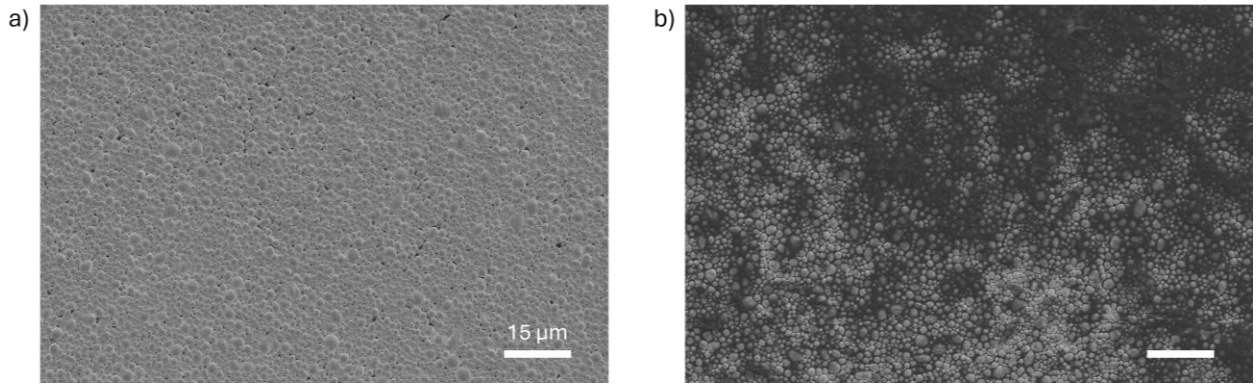

Figure B.7 SEM images of a) as-printed P35 composite and b) acid-treated P35 composite.

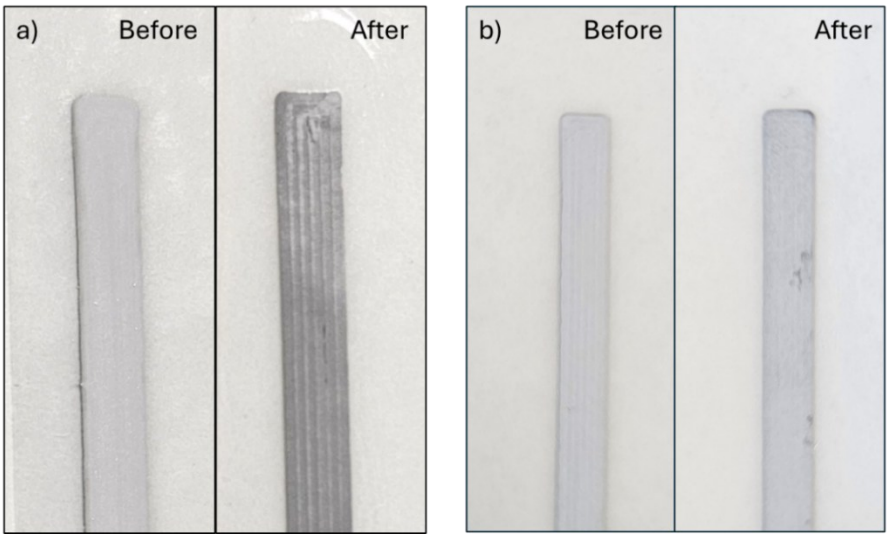

Figure B.8 Optical images of as-printed P35 before & after a) acid solution and b) acetone treatment. All the printed LM composites have a 2 mm width.

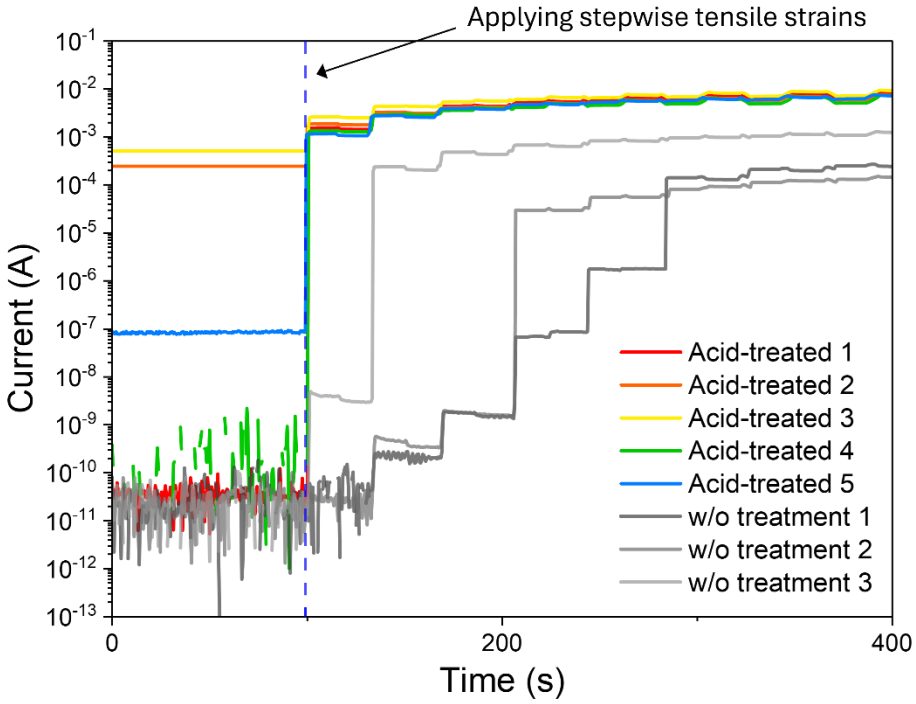

Figure B.9 Currents vs time plot in log scale, comparing the acid-treated composites (n=5) to non-treated composites (n=3) from 0 to 400 seconds in Figure 3c. The composites have currents as low as noise level (10^{-10}-10^{-11} A) before mechanical activation. Few acid-treated composites (Acid-treated 2,3, and 5) showed higher current (10^{-3}-10^{-7} A) before activation, likely due to minor activation while handling the samples printed on a stretchable TPU substrate. However, the minor activation did not affect the electrical properties of fully activated LM composites.

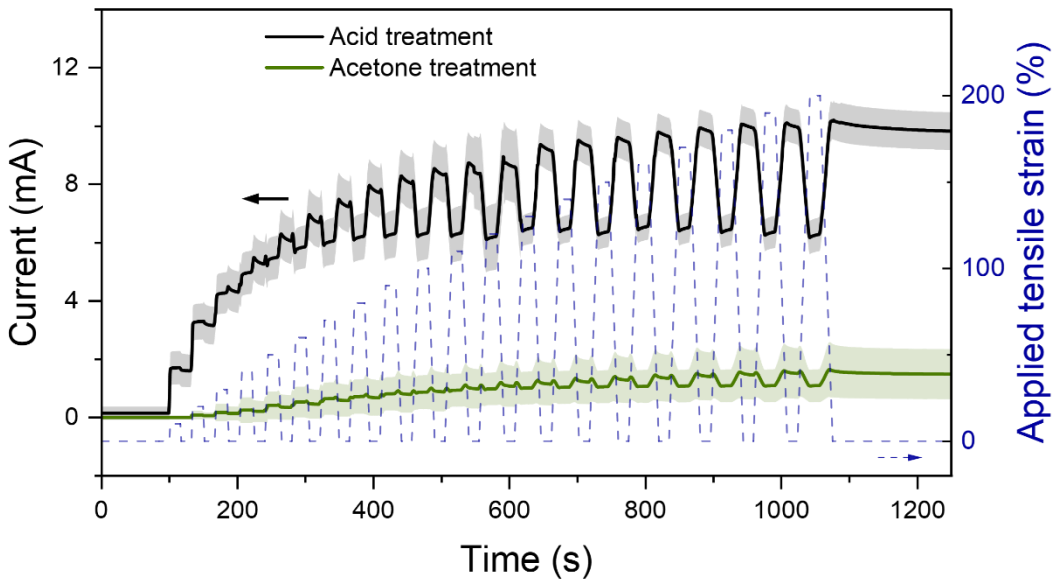

Figure B.10 Comparison of the currents of acid-treated (n=5) and acetone-treated (n=3) LM composites during mechanical activation.

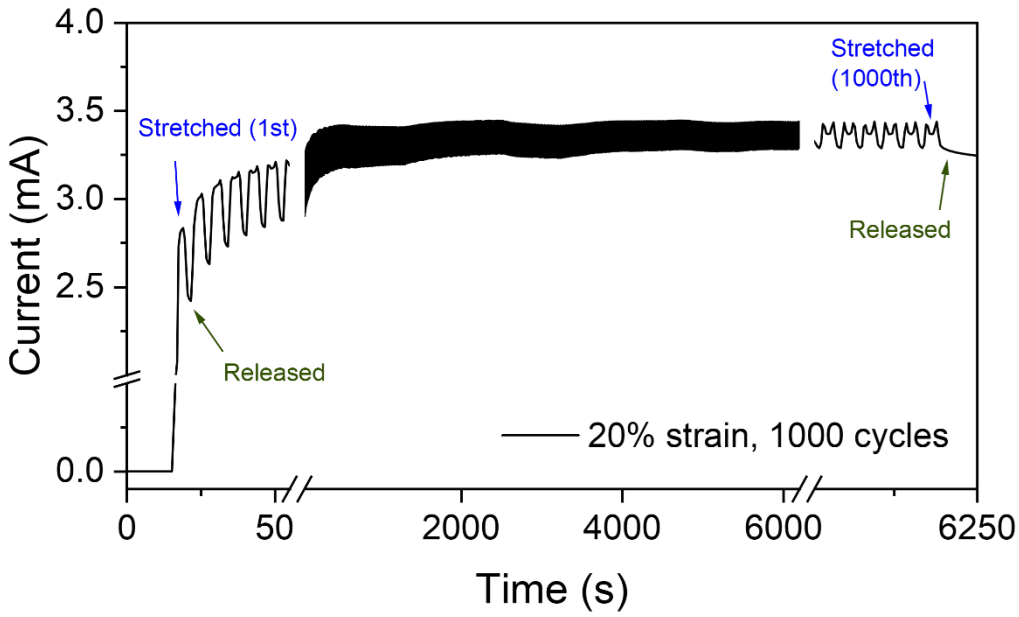

Figure B.11 The current of P35 while applying 20% strain 1000 times. The current in 0-55 and 6200-6250 second were enlarged.

Table B.1 Electrical conductivities of LM composites (*n*=5). P15, P35, and P70 were prepared with 15 mg, 35 mg, and 70 mg PASTA, respectively. The composites were mechanically activated with 50% tensile strain 20 times before the measurement.

	Chemical Treatment	Conductivity [s cm-1]
P15	Acid	3555 ± 875
P35	Acid	2770 ± 286
P35	Acetone	288 ± 136
P35	(x)	196 ± 86
P70	Acid	429 ± 108

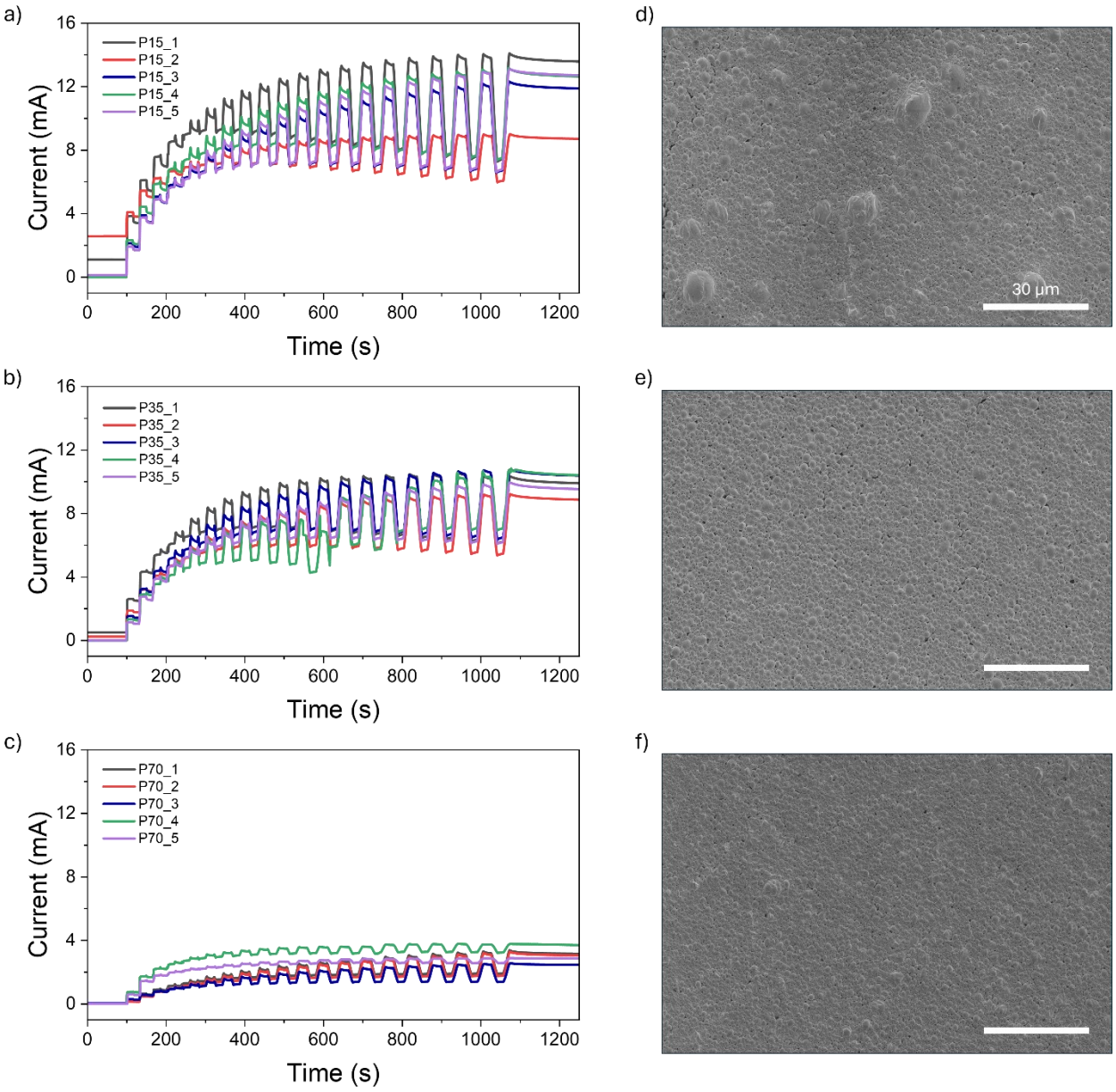

Figure B.12 The mechanical activation test of acid-treated LM/PASTA containing a) 15 mg, b) 35 mg, and c) 70 mg polymer (n = 5). The applied tensile strain is increased by 10 % step by step from 0% to 200%. SEM images of as-printed d) P15, e) P35, and f) P70.

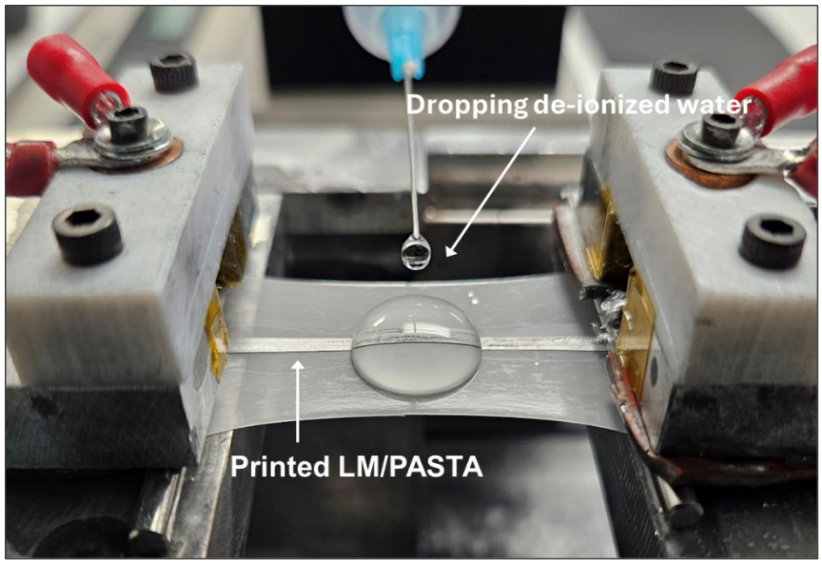

Figure B.14 Resistance vs. time of LM/PASTA (P35) over 5000 cycles of 50% strain conducted over 16 h under dry and wet conditions. The samples were prepared with exactly same conditions to the composites used in Figure 4.4e in the main text.

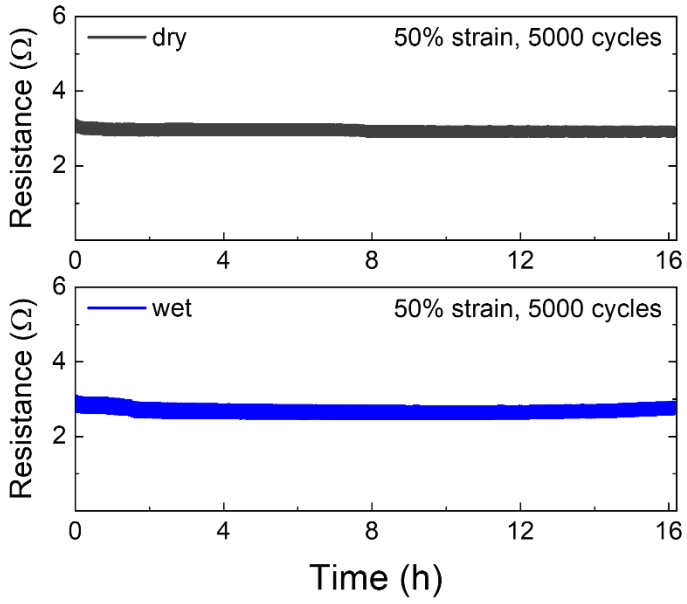

Figure B.13 Optical image of electromechanical durability test with a partially wet LM composite.

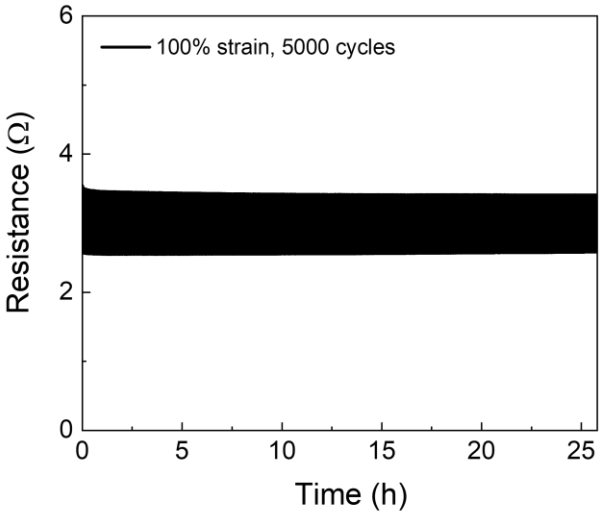

Figure B.15 . Resistance vs cycle numbers of the dry LM/PASTA (P35). The tests were conducted with 100% tensile strain for 5000 cycles at a speed of 5 mm s^{-1}.

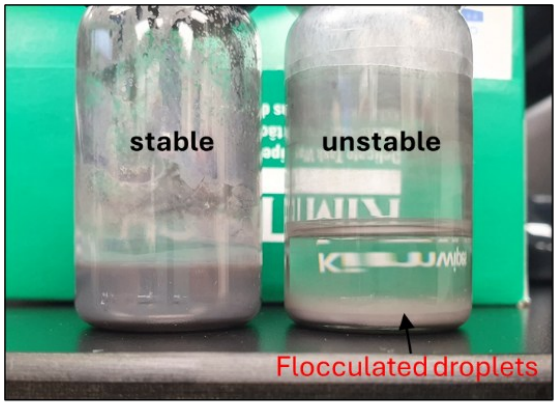

Figure B.16 Digital photograph of LM suspensions. The left suspension in toluene has well-dispersed LM droplets after a day but the right suspension containing DMF solvent has flocculated droplets on the bottom.

The effects of polar solvents on the stability of suspension were shown. PASTA-grafted LM suspension with toluene on the left side is well-dispersed a day after preparation. On the other hand, the LM droplets in the suspension prepared with PASTA dissolved in DMF solvent flocculated.

Table B.2 Comparison of LM composite-based stretchable conductors

LM	Polymer	Conductivity [105 S m^{-1}]	Stretchabilitya) [%]	Stability in water	Recyclability	Ref
EGaIn	PASTA	0.4-3.6	500	Yes	Yes	This work
EGaIn	Poly(styrene-isoprene-styrene)	N/A	500	N/A	Yes	[70]
EGaIn	Poly(styrene-isoprene-styrene) and polybutadiene	0.2	1200	N/A	Yes	[71]
EGaIn	Polyester polyol-rich TPU	22.5	2200	N/A	Yes	[84]
EGaIn	PVA	1.3	20	N/A	Yes	[89]
EGaIn	PSS	15.0	500	N/A	Yes	[83]
EGaIn	PDMS	1.4	50	N/A	N/A	[87]
Galinstan	PDMS	1.2	75	N/A	N/A	[86]
EGaIn	PDMS	N/A	128	N/A	N/A	[190]
EGaIn	PDMS and Ecoflex	N/A	40	Yesb)	N/A	[88]

a) The maximum stretchability exhibited in each work was surveyed.

b) Compared to this work, which showed that LM/PASTA as a stretchable conductor is electromechanically durable in water, they demonstrated the electrical stability of their unstrained composites in water.

Table B.3 Solubility test of polymer and LM suspension stability test in various solvents

Solvent	Solubility of the polymer	Suspension stability	Dipole moment
Toluene	O	O	0.36 D
orth-Xylene	O	O	0.45 D
Anisole	O	O	1.38 D
THF	O	O	1.75 D
DMF	O	X	3.82 D
Acetone	O	N/A	2.88 D
Cyclohexane	X	N/A	0 D
1-Octanol	X	N/A	1.68 D
DMSO	X	N/A	3.96 D
Water	X	N/A	1.85 D

Through solvent tests, we found that PASTA was soluble in DMF, toluene, anisole, xylene, THF, and acetone. Solvent polarity is correlated to the dipole moment of the polymer, indicating DMF and DMSO are polar solvents. It was reported that the polar solvent DMSO can detach the polymer grafted on LM droplets.[11] We believe that DMF may have the same effect, leading to flocculation for a short time. Toluene was selected as the solvent for LM composite ink development since it is compatible with the printer parts and relatively less toxic than the other nonpolar solvents.

Supporting Note

Calculation of the theoretical resistance for a sample with a constant conductivity

The traditional equation of resistance $R(t)$ at a given time t can be expressed as follows:

$$R(t) = \rho(t) \times \frac{L(t)}{A(t)} = \frac{1}{\sigma(t)} \times \frac{L(t)^2}{V(t)} \quad \text{(B. 1)}$$

where $\rho(t)$, $\sigma(t)$, $L(t)$, $A(t)$,and $V(t)$ are resistivity, conductivity, length, cross-sectional area, and volume of the material at a given time t. When t=0, the resistance and the conductivity of unstretched material are R_0 and σ_0, and the dimension factors are L_0, A_0, and V_0. Hence, the resistance under strain with respect to the original value can be expressed as:

$$\frac{R(t)}{R_0} = \frac{\sigma_0 \cdot V_0}{\sigma(t) \cdot V(t)} \times \frac{L(t)^2}{{L_0}^2} \quad \text{(B. 2)}$$

When assuming the conductivity and the volume remain constant while stretching the material, Equation (S2) can be simplified as:

$$\frac{R(t)}{R_0} = \big(1 + \varepsilon(t)\big)^2 \quad \text{(B. 3)}$$

where $\varepsilon(t)$ is the strain corresponding to $(L(t)/L_0)$.

APPENDIX C SUPPORTING INFORMATION OF ARTICLE 2: RECYCLABLE PRINTED LIQUID METAL COMPOSITE FOR UNDERWATER STRETCHABLE ELECTRONICS

Chi-hyeong Kim and Fabio Cicoira*

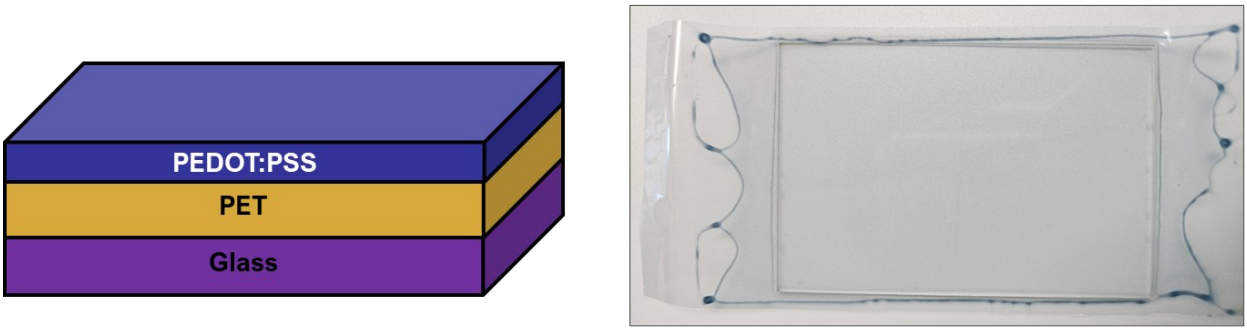

Figure C.1 Scheme (left) and optical photo (right) of the as-prepared dry PEDOT:PSS film spin-coated once. The glass plate is 5x7 cm^2.

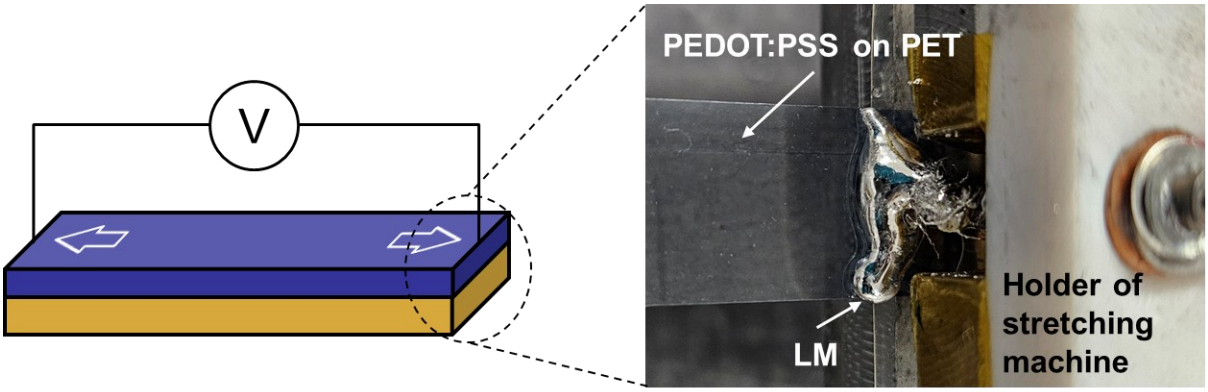

Figure C.2 Scheme (left) and optical photo (right) of the electrical connection for electromechanical characterization. The PEDOT:PSS film was connected to the equipment with liquid metal.

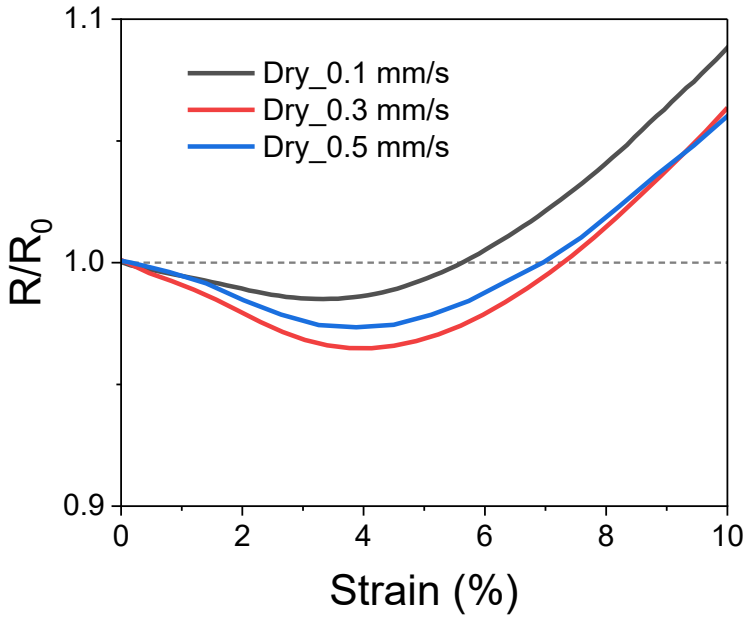

Figure C.3 Changes in normalized resistance of dry PEDOT:PSS films as a function of strain, which are magnified curves from Figure 5.3a